REMOTE SENSING OF LAKE DYNAMICS IN ALASKA

By

Prajna R. Lindgren

RECOMMENDED:

Dr. Vladimir E. Romanovsky

Dr. Franz J. Meyer

Dr. Katey M. Walter Anthony
Advisory Committee Co-Chair

Dr. Guido Grosse
Advisory Committee Co-Chair

Dr. Paul J. McCarthy
Chair, Department of Geosciences

APPROVED:

Dr. Paul W. Layer
Dean, College of Natural Science and Mathematics

Dr. John C. Eichelberger
Dean of the Graduate School

12 April 2016
Date

REMOTE SENSING OF LAKE DYNAMICS IN ALASKA

A

DISSERTATION

Presented to the Faculty

of the University of Alaska Fairbanks

in Partial Fulfillment of the Requirements

for the Degree of

DOCTOR OF PHILOSOPHY

By

Prajna R. Lindgren, B.S., M.A.

Fairbanks, Alaska

May 2016

Abstract

Lakes are abundant in high northern latitude permafrost regions. They are important ecosystem components forming a complex and dynamic landscape with repeated cycles of lake formation and drainage affecting regional hydrological and terrestrial characteristics, biogeochemical processes and carbon cycling, wildlife habitats, and human communities living in the permafrost region. Remote sensing is a useful tool to map the spatial distribution of lakes and assess its change, understand lake dynamics, and to extract useful information to study their associated feedbacks in a changing climate. In this dissertation, I focused on remote sensing studies associated with (1) methane ebullition from a thermokarst lake, (2) post-drainage succession patterns in drained thermokarst lake basins, and (3) lake change dynamics.

I developed a semi-automatic classification method based on an Object-based Image Analysis (OBIA) framework to detect methane ebullition bubbles trapped in a snow-free ice-covered lake using high-resolution airborne images of Goldstream lake, Fairbanks, Alaska acquired following freeze up in October of 2011 and 2012. This study showed that remote sensing is a valuable tool to map ebullition bubbles (bubble patches) on the entire lake surface with an accuracy of > 95%, a task that is difficult to achieve through field-based survey alone. The image analysis performed by combining the mapping results from the OBIA and field-based observations showed a relationship between bubble patch brightness and ground-measured methane flux, which was then used to estimate the whole-lake methane flux. A strong inverse exponential relationship (R^2 >= 0.79) was found between the percent of the surface area of lake ice covered with bubble patches and distance from the active thermokarst lake margin, indicating high methane production as a response to thermokarst activity that released labile organic-rich carbon along the eroding lake margin. Despite the influence of atmospheric pressure conditions on distribution of ebullition bubble patches following the lake freeze-up events, the spatiotemporal regularity of bubble patches revealed that a larger number of seeps are stable over at least annual timescales. This remote sensing technique is applicable to other regions for mapping ebullition bubbles trapped in snow-free ice-covered lakes, identifying their relative flux, and assessing their spatiotemporal dynamics.

By using TerraSAR-X (TSX) Synthetic Aperture Radar (SAR) backscatter data and the Normalized Difference Vegetation Index (NDVI) derived from a Landsat-5 image from the year

2009, I characterized drained thermokarst lake basins (DTLBs) of various age ranging between 0 to 10,000 years since drainage in the northern Seward Peninsula, Alaska. In the study I found logarithmic relationships of basin age from 0 to 10,000 years with mean basin TSX backscatter ($R^2 = 0.36$) and with mean basin NDVI ($R^2 = 0.53$). However, TSX data performed much better to discriminate older basins in the age class 50–10,000 years with $R^2 = 0.58$, while no significant relationship was found between NDVI and basin age. Results of this study demonstrated the potential application of X-band SAR data in combination with NDVI data to enhance differentiation of soil moisture and vegetation status on drained basins for mapping long-term succession dynamics of DTLBs.

Finally, I demonstrated the utility of Landsat imagery to identify lake distribution patterns and changes between 1972 and 2014 in six major lake-rich study regions across various permafrost zones covering an area of 68,830 km^2 in western Alaska. Even though lake area change was found to be positive (increase by less than 4%) in some study areas while negative (decrease by 4-15%) in others, there was a widespread drainage of mainly large lakes in all regions creating remnant ponds that increased the abundance of lakes <10 ha in all study regions by 2-27%. The average lake area decline observed in various permafrost zones did not represent the trend of individual sites due to spatial heterogeneity in lake characteristics. While lake drainage dominated the non-continuous permafrost zones, areas of continuous permafrost showed both trends of negative and positive lake area change accompanied by major lake drainage events that led to a regional lake area loss in the continuous permafrost zone. This remote sensing technique proved to be useful in identifying ongoing lake drainage and expansion events within study regions and a regional shift in lake distribution (i.e. lake area loss) that is happening in western Alaska.

Based upon my research, there is an immense opportunity to use and combine various remote sensing tools to study lake dynamics and to evaluate associated environmental changes. Future work should be directed towards collaborative research for combining field-based observations and remote sensing tools to improve the understanding of how lakes and drained lake basins change in a changing climate as well as extend the scale of observations of methane ebullition features by covering many lakes in an environmentally diverse set of regions. This will guide us to understanding the feedback of lake dynamics to the surrounding ecosystem, global

carbon budget, and to upscale the response of lakes to changing climate and permafrost environments to larger regions.

Table of Contents

List of Figures

List of Tables

List of Supplementary Materials

Chapter 3

Supplementary online material: Detection and spatiotemporal analysis of methane ebullition on thermokarst lake ice using high-resolution optical aeiral imagery (Available for download at http://www.biogeosciences.net/13/27/2016/)

Chapter 5

Dedication Page

With great love and affection, I dedicate this dissertation to my parents who inspired me and believed in me.

Acknowledgements

First and foremost I would like to thank my committee co-chairs, Guido Grosse and Katey Walter Anthony, for giving me an opportunity to pursue a Ph.D. I am very appreciative of the continuous support they have given me these past five years. Guido provided hours of advice and assistance despite his busy schedule while I was working on each chapter. He offered opportunities to expand my knowledge on the periglacial environment and processes, encouraging me to think about the big picture. This tremendously complemented my remote sensing research. He was patient with me when I was overwhelmed or distracted, and always allowed for exploration of new ideas and research tools. Further, I am grateful to Guido for providing the funding throughout this Ph.D. Katey offered numerous opportunities to work in the field and graciously spent hours with me teaching and assisting. This allowed me to appreciate the importance of field observations, to understand the physical processes, and think about overarching research questions. I was able to apply this knowledge in remote sensing research that utilized field methods and results to guide analyses in the lab. I am very thankful to my other committee members, Franz Meyer and Vladimir Romanovsky, for their assistance and suggestions throughout my research. They generously spent their time with me when I needed their guidance. The wisdom and knowledge they provided helped me in every step of my research and will be extremely beneficial to my future career.

I thankfully acknowledge the following funding sources that made my Ph.D. work possible: NASA (grant NNX08AJ37G and NNX11AH20G), National Science Foundation (grant OPP-0732735 and 1107892), and the Western Alaska Landscape Conservation Cooperative (WA2011-02). I thank the German Space Agency DLR for providing TerraSAR-X images through IPY grant LAN0351 and the US National Park Service for research permits in Bering Land Bridge National preserve and providing Ikonos imagery.

I am the primary contributor for all the chapters in this dissertation. I developed the methods, performed data analysis, and took the lead role in writing each of the manuscript. I am very grateful to all the coauthors for their significant contributions. I am indebted to Guido Grosse for his assistance with data analysis, interpretation of results and manuscript writing on Chapter 2, Chapter 3, Chapter 4, and Chapter 5. Katey Walter Anthony assisted with data collection, interpretation of results and manuscript writing for Chapter 2, Chapter 3, and Chapter

4. Franz Meyer helped with data analysis and manuscript writing for Chapter 2 and Chapter 3. Miriam Jones and Ben Jones provided data associated with drained basin age and helped with manuscript writing for Chapter 4. Chapter 5 benefited from the contributions to interpretation of results and manuscript writing provided by Vladimir Romanovsky and Louise Farquharson.

I am grateful for the assistance provided by Peter Anthony with the statistical analysis in Chapter 3. I would also like to thank my colleagues Allen Bondurant, Melanie Engram, Amy Strohm, and Josefine Lenz for their help in the field and for all the fun adventure we had together. I am very grateful to Jessie Cherry for helping with aerial image acquisitions. I would also like to thank Bill Walker and Bruce Crevensten for UAV image acquisitions and processing. I would also like to thank my colleagues in the Permafrost Lab who provided technical support to perform my research smoothly. I would like to thank my former M.A. advisor Ronald Eastman of Clark University, Worcester, MA and former colleagues at the Clark Labs for helping me build the foundation of my remote sensing expertise.

Finally, but most importantly, I would like to thank my husband, Michael Lindgren. This dissertation would not have been possible without his love, support and encouragement. He listened to me and provided advice through all stages of this Ph.D. when I needed a friend/confidant to talk to. He also inspired me to think outside the box. He introduced me to the open-source computing world surrounding data science that allowed me to improve my research techniques by leaps and bounds. This was especially true while dealing with large volumes of data that required efficient automation. I would like to thank my parents, especially my father, and family in Nepal, who supported me in all my pursuits, for their love and inspiration. I am also thankful to my new family in the United States who has been always so loving and supportive.

Chapter 1. Introduction

1.1. Background and overview of dissertation

Permafrost, perennially frozen ground that remains at or below 0 ^{o}C for two or more years, is an important part of the cryosphere and is widely distributed in the high northern latitudes (Zhang et al., 2008). Permafrost is classified by its spatial extent into four types: (1) continuous (> 90% permafrost cover), (2) discontinuous (50-90% permafrost cover), (3) sporadic (10-50% permafrost cover), and (4) isolated (up to 10% permafrost cover). The occurrence of permafrost, which creates an impervious subsurface water barrier, has an immense influence on the distribution of lakes and allows lakes to occur in high abundance in permafrost-dominated regions. Approximately one-fourth of the lakes on Earth are estimated to occur in the high northern latitudes (Lehner and Döll, 2004) and the majority of these lakes are located in permafrost regions (Grosse et al., 2013). About 41% of all lakes > 10 ha encompassing 50% of the total lake area are present in permafrost regions with high concentrations of lakes occurring in many Arctic and Subarctic lowlands (Grosse et al., 2013).

Climate warming is amplified in the Arctic and Subarctic with near-surface air temperatures rising nearly twice as much as the world average in the past decades (ACIA, 2005; Solomon et al., 2007; Serreze and Francis, 2006; Hinzman et al., 2005; Walsh et al., 2011). This has greatly influenced the ground thermal regime of the region. Permafrost temperatures have increased throughout the Arctic and Subarctic regions particularly during the past two to three decades (Osterkamp and Romanovsky, 1999; Romanovsky et al., 2010; Smith et al., 2010). Permafrost degradation can change lake habitat characteristics drastically through initiation of new lakes by thermokarst processes as well as through growth and drainage of existing lakes. Thermokarst refers to the process by which characteristic landforms result from the thawing of ice-rich permafrost or the melting of massive ice (French, 2007). The presence of lakes, both thermokarst and non-thermokarst origin, can alter the thermal regime of surrounding permafrost and subsequent degradation of confining permafrost can further enlarge these lakes (West and Plug, 2008). Continued degradation may trigger lake drainage by processes such as stream piracy, tapping, bank overflow or ice-wedge erosion, or in discontinuous permafrost zones lakes may drain internally through open taliks (Hopkins, 1949; Mackay, 1988; Yoshikawa and Hinzman, 2003; Hinkel et al., 2007). Therefore, permafrost-lake interactions are a crucial component that

can alter the current Arctic and Subarctic landscape characteristics if the climate continues to warm. This will have major implications on hydrological and terrestrial dynamics of the region (Yoshikawa and Hinzman, 2003; Rowland et al., 2011; Jorgenson et al., 2010), wildlife habitat changes (Clark et al., 2010), changes in water accessibility for village communities and industries (Eisner et al., 2009; Alessa et al., 2008; Jones et al., 2009), and biogeochemical processes and carbon cycling (Walter et al., 2006; Walter et al., 2008; Schuur et al., 2008; Tranvik et al., 2009; van Huissteden et al., 2011; Schuur et al., 2015).

A large number of lakes are located in the remote regions of the Arctic and Subarctic. Therefore, remote sensing is a useful tool to map the spatial distribution of lakes, assess its changes, understand the dynamics at all stages from lake formation to post-drainage and to extract useful information to study their associated feedbacks (Frohn et al., 2005; Hinkel et al., 2005; Smith et al., 2005; Riordan et al., 2006; Hinkel et al., 2007; Grosse et al., 2008; Plug et al., 2008; Sannel and Brown, 2010; Jones et al., 2011; Morgenstern et al., 2011; Jones et al., 2012; Jones and Arp, 2015; Chen et al., 2014; Roach et al., 2011; Karlsson et al., 2014). Even though remote sensing techniques are now widely used for advancing research related to lakes in permafrost regions, there are many potential applications of remote sensing for studying lake dynamics that are yet to be explored.

My dissertation focuses on the application of a variety of remote sensing approaches and offers some new techniques to study different aspects of permafrost region lake dynamics at local and regional scales. In Chapter 2, I present an object-based classification method to detect methane ebullition bubbles trapped in a snow-free ice-covered lake located in Fairbanks, Alaska using high-resolution airborne imagery. Chapter 3 examines the spatiotemporal dynamics of methane ebullition bubbles trapped in lake ice and provides an estimate of whole-lake methane ebullition using field-measured observations and the results from the Object-based Image Analysis (OBIA) bubble mapping presented in Chapter 2. Chapter 4 focuses on the application of TerraSAR-X backscatter in conjunction with Normalized Difference Vegetation Index (NDVI) to characterize post-drainage succession patterns in drained thermokarst lake basins on the Seward Peninsula, Alaska. Chapter 5 evaluates the lake distribution and changes based on Landsat imagery between 1972 and 2014 in six major lake-rich areas across various permafrost zones (continuous, discontinuous, sporadic, and isolated extent) located in western Alaska.

1.2. Methane emission from thermokarst lakes

Permafrost stores about 1330-1580 Pg of soil organic carbon, an estimate that only accounts for surface carbon (0-3 m depth) and deep carbon in the yedoma region and Arctic river deltas (> 3 m depth) (Schuur et al., 2015). Additional carbon (potential for 400 Pg carbon) stored in other deep terrestrial permafrost deposits including subsea permafrost is still poorly quantified. This has important implications on the high latitude northern carbon cycle and the global climate system (Zimov et al., 2006; Walter et al., 2006; Schuur et al., 2008; Koven et al., 2011; Grosse et al., 2011; Schuur et al., 2015). Permafrost degradation can facilitate the transfer of this permafrost-stored carbon to the atmosphere in the form of the greenhouse gases carbon dioxide (CO_2) and methane (CH_4), resulting in a positive feedback to global climate change (Zimov et al., 2006; Walter et al., 2006; Schuur et al., 2008; Koven et al., 2011). In particular, thermokarst lakes are one of the common forms of permafrost degradation (Grosse et al., 2013) and an effective mechanism for the release of permafrost-stored terrestrial carbon to the atmosphere in the form of CH_4 ebullition (bubbling) (Zimov et al., 1997; Walter et al., 2006). Accounting for methane emissions from thermokarst lakes can significantly improve estimation of lake contributions to regional and global atmospheric carbon budgets (Walter et al., 2007; Bastviken et al., 2011).

Methane can be transported from lake sediment to the atmosphere by three major pathways: molecular diffusion, ebullition or transport via gas-conducting tissues of emergent plants (Bastviken et al., 2011). Among these, ebullition is known to be the dominant pathway of methane release from many lakes to the atmosphere (Keller and Stallard, 1994; Bastviken, 2004). Bubbles impeded by the wintertime lake ice sheet in cold regions form distinct white patches as a function of bubbling rate when lake ice grows downward and around them, trapping the gas in and under the ice. This provides a unique opportunity to identify ebullition point sources and estimate the associated flux based on bubble size and morphology (Walter Anthony et al., 2010). Yet, methane fluxes from thermokarst lakes have been difficult to estimate due to logistical difficulties of field surveys in remote locations and spatiotemporal patchiness of methane ebullition within individual lakes. Remote sensing tools can overcome the logistical challenges that exist in field-based surveys by offering an opportunity to detect methane ebullition bubbles trapped in lake ice across the whole lake. This can immensely complement field-based surveys to

enhance the ability for quantifying lake methane emission at regional scales and to understand spatiotemporal dynamics of methane ebullition. Until now, only synthetic aperture radar (SAR) remote sensing data has been utilized to quantify methane emission from lakes (Walter et al., 2008; Engram et al., 2012). SAR is capable of penetrating into snow-covered lake ice and detecting trapped methane bubbles. However, the moderate spatial resolution of current long-wave band SAR systems such as L-band SAR can be a limiting factor to estimate methane emission from small lakes and along lake margins, and to capture delicate spatial patterns of ebullition seeps on lakes. SAR backscatter signals of the lake ice near the shore tend to be affected by strong backscatter gradients at the lake shoreline (Walter et al., 2008; Engram et al., 2012). This limits its usability in proximity to shores (about 1 pixel around lake shores is therefore excluded in SAR analyses) where an important portion of ebullition may take place on eroding thermokarst margins.

In Chapter 2, I developed a classification technique built on using an OBIA framework to successfully map individual ebullition bubbles trapped in early winter snow-free lake ice of Goldstream Lake located in Fairbanks, Alaska. I used high-resolution (9-11 cm) optical aerial images acquired two and four days following freeze up in the years 2011 and 2012, respectively. The design of the multiresolution segmentation and region-specific rulesets allowed the identification of bubble features and separation from other confounding factors such as snow, submerged vegetation, shadows, and open water.

In Chapter 3, I characterized methane ebullition seeps mapped in 2011 and 2012 aerial images of Goldstream Lake to estimate whole-lake methane flux. I also performed a spatiotemporal analysis with the goals of discerning: (1) whether we could use high-resolution optical imagery to identify field-mapped ebullition seeps for estimating whole-lake methane ebullition and (2) the variety of information that could be extracted for further research to enhance the understanding of ebullition dynamics and the variables that control such dynamics. I classified the mapped bubbles into four distinct types of seeps (point sources and hotspot) as identified by Walter Anthony et al. (2010): (1) A-type seep (ebullition rate: 22 ± 4 mLgas d^{-1}), (2) B-type seep (ebullition rate: 211 ± 39 mLgas d^{-1}), (3) C-type seep (ebullition rate: 1726 ± 685 mLgas d^{-1}), and (4) Hotspots (ebullition rate: 7801 ± 764 mLgas d^{-1}). I applied the ebullition rates determined from bubble-trap field measurements (Walter Anthony et al., 2010) to

the distribution of seeps identified in my images to derive an estimate of the whole-lake ebullition flux. I further assessed the spatial distribution of ebullition bubble patches on the lake as a function of distance from the eroding thermokarst shore and studied the temporal dynamics of bubble patterns on the lake. In this chapter, I also highlight the complexities associated with ebullition and the benefits as well as challenges of aerial image analysis for ebullition seep mapping.

1.3. Drained thermokarst lake basins

Thermokarst lakes form in closed depressions following surface settlement due to melting of excess ground ice or when underlying ice-rich permafrost thaws. However, they are in many cases not persistent on the landscape but last for centuries to millennia until they drain. The formation of thermokarst lakes on permafrost influences the ground thermal regime with a positive feedback to permafrost degradation (West and Plug, 2008). As a result of this continued thawing of permafrost under and around a lake, lake growth increases the chances of lateral or internal drainage via bank overflow, headward erosion, lake tapping, development of drainage pathways, or formation of open taliks (Hopkins, 1949; Mackay, 1988; Yoshikawa and Hinzman, 2003; Hinkel et al., 2007; Marsh et al., 2009; Jones et al., 2011; Grosse et al., 2013; Jones and Arp, 2015). Following drainage, re-vegetation and peat accumulation begins in drained basins, which starts in the first 20-100 years (Eisner and Peterson, 1998; Bliss and Peterson, 1992; Jones et al., 2012; Hinkel et al., 2005). In addition, cold winter frost can penetrate into the exposed lake bottom, and new permafrost aggradation may begin to form in the drained lake basin (Ling and Zhang, 2004). Eventually, the basin surface gets drier and basin productivity decreases as nutrients from the fresh lake sediments are consumed and permafrost aggradation causes limitations in rooting depth and nutrient availability. Over time, low-centered ice wedge polygons may start to develop in drained basins if climatic conditions are favorable, which eventually creates preconditions for new ponding and the beginning of a new thermokarst lake cycle (Mackay and Burn, 2002). The hypothesis of 'thaw lake cycle' that thermokarst lakes form, drain, and reform on millennial time scales has been reported by previous studies based on observations from several regions of Alaska (Hopkins, 1949; Billings and Peterson, 1980; Hinkel et al., 2003; Plug et al., 2008). The repeated lake formation and drainage forms complex and characteristic landscapes evident in many thermokarst-affected lowlands occupied with a mosaic

of lakes and drained basins at various stages of post-drainage succession affecting hydrology, permafrost, carbon cycling, vegetation, and wildlife habitats as well as human communities living in the permafrost region (Hinkel et al., 2003; Yoshikawa and Hinzman, 2003; Walter et al., 2006; Alessa et al., 2008; Eisner et al., 2009; Clark et al., 2010; Rowland et al., 2011; van Huissteden et al., 2011).

Post-drainage changes in vegetation, surface hydrology, soil characteristics and often permafrost aggradation follow a relatively predictable pattern reflecting successional stage or the relative age of the drained basin (Hinkel et al., 2003; Jones et al., 2012). A number of studies have exploited moderate and low resolution satellite images derived from optical sensors to map drained thermokarst lake basins, evaluate their spatial and temporal dynamics, and classify their relative age relying on relationships of land surface properties to post-drainage succession in vegetation, soils and permafrost aggradation (Hinkel et al., 2003; Frohn et al., 2005; Zona et al., 2010; Jones et al., 2012). Hinkel et al. (2003) and Jones et al. (2012) were able to establish a correlation between basin age and peat thickness to estimate carbon accumulation rates in DTLBs and to scale this information across a larger study. This is an important finding that suggests a potential application of remote sensing to determine the amount of carbon stored in DTLBs that could partially offsets methane emission from lakes and wetlands in thermokarst-affected landscapes or could be released to the atmosphere as methane gas through thermokarst processes.

In Chapter 4, I demonstrate the application of high resolution X-band SAR data of the German TerraSAR-X (TSX) satellite for determining the time since lake drainage (or drained basin age) based on basin surface properties as characterized by the SAR backscatter signal in order to understand the post-drainage succession dynamics for a set of drained thermokarst lake basins. This study was conducted for an area of approximately 3,800 km^2 on the northern Seward Peninsula, Alaska. The main goal of this study was to take the advantage of SAR for its capacity to penetrate into the near-surface soil and detect soil moisture, which enhances the ability to characterize basin successional stages more accurately within a few centuries after drainage, the period during which basin vegetation succession slows down. Remote sensing data derived from optical sensors has a disadvantage in this regard since it is more limited to detecting surface conditions. I compared the known age since drainage of a set of 74 basins located across the

study region with the basin-wide TerraSAR-X backscatter mean values to investigate their relationship. One of the goals was to examine how this would compare to the relationship estimated by previous studies using Normalized Difference Vegetation Index (NDVI) derived from optical remote sensing data. The age of 74 basins were determined from multi-sensor optical time series imagery covering the 1950-2010 period (Grosse et al., personal communication) and accelerated mass spectrometry radiocarbon-dating of the basal portion of terrestrial peat covering lake sediments (Jones et al., 2012).

1.4. Lake distribution and changes

Lakes are abundant in extensive lowland landscapes of Northeast Siberia, northern West Siberia (Smith et al., 2005; Grosse et al., 2006; Karlsson et al., 2014); in Alaska on the North Slope, Seward Peninsula, North Western Alaska, Yukon-Kuskokwim Delta region (Sellmann et al., 1975; Hinkel et al., 2005; Jones et al., 2011; Arp and Jones, 2009); and in Canada on the Mackenzie Delta, Tuktoyaktuk Peninsula, and Yukon Coastal plain (Mackay, 1988; Plug et al. 2008; West and Plug, 2008; Plug and West, 2009). They are important ecosystem components forming a complex and dynamic landscape sometimes with repeated cycles of lake formation and drainage (Frohn et al., 2005; Jorgenson and Shur, 2007; Arp and Jones, 2009; Jones et al., 2012). Their dynamics and evolution at the landscape level have important implications for carbon budgets in permafrost regions (Walter et al. 2006), terrestrial and hydrologic change that accompanies permafrost degradation (Jorgenson et al. 2010, Rowland et al., 2011), and habitat character and distribution (Clark et al., 2010). They are important resources for industrial water needs and for indigenous communities as these lakes provide fresh drinking water as well as support subsistence hunting and fishing (Eisner et al. 2009; Jones et al., 2009).

A suite of studies has utilized remotely sensed imagery to assess the spatial distribution of lakes and changes in lake area extent across the Arctic and Subarctic regions (Frohn et al., 2005; Yoshikawa and Hinzman, 2003; Hinkel et al., 2005; Smith et al., 2005; Riordan et al., 2006; Grosse et al., 2008; Plug et al., 2008; Labrecque et al., 2009; Marsh et al., 2009; Roach et al., 2011; Jones et al. 2011; Chen et al., 2014; Karlsson et al., 2014). Many of these studies have reported changes in lake area extent at various rates in several locations particularly since the 1970s, when satellite images became available. However, the drivers for such changes in lake area extent are still discussed. Some studies have found regional patterns that were linked with

regional permafrost extent and the rate of permafrost degradation (Smith et al., 2005; Yoshikawa and Hinzman, 2003; Jones et al., 2011; Karlsson et al., 2014). In general, it is thought that lakes are expanding in the continuous permafrost zone and they are draining in the non-continuous permafrost zone (discontinuous, sporadic and isolated) (Smith et al., 2005). Other studies have indicated that intra- and inter-annual patterns of precipitation, evaporation, and ice jam flooding events are also influencing the areal extent of lakes (Bosikov, 1998; Riordan et al., 2006; Plug et al. 2008; Jones et al., 2009; Labrecque et al., 2009; Roach et al., 2011; Chen et al., 2013; Chen et al., 2014). Temporal and spatial heterogeneity in lake area change indicates regional and temporal variation likely related to climate and environment. Lake types vary across the Arctic and Subarctic regions and may therefore respond differently to changing climate and environment.

In Chapter 5, I conducted a Landsat-based (MSS and OLI) study to assess lake distribution and changes in areal extent of lakes larger than 1 ha between 1970s and 2014 in six major lake-rich regions across various permafrost zones (continuous, discontinuous, sporadic, and isolated extent) in western Alaska. The study regions were (1) Beringia, (2) Baldwin Peninsula, (3) Kobuk Delta, (4) Selawik, (5) Central Seward Peninsula, and (6) Yukon-Kuskokwim Delta, covering a total area of 68,830 km^2. Additionally, I investigated the patterns of lake area change (1) among different study regions and (2) among different permafrost zones in the study regions to understand how the patterns of lake change express at different scales: How do local lake change patterns influence the regional lake change patterns? Eventually, I investigated the relationship between trends of lake change and permafrost extent to see if the hypothesis (lakes are expanding in the continuous permafrost zone and shrinking in the non-continuous permafrost zone) was valid for western Alaska.

1.5. References

ACIA, 2005. Impacts of a warming arctic: arctic climate impact assessment, Cambridge University Press, Cambridge, UK, 139 p.

Alessa, L., Kliskey, A., Lammers, R., Arp, C., White, D., Hinzman, L., Busey, R., 2008. The Arctic Water Resource Vulnerability Index: An Integrated Assessment Tool for Community Resilience and Vulnerability with Respect to Freshwater. Environ. Manage. 42, 523–541. doi:10.1007/s00267-008-9152-0

Arp C. D., Jones, B. M., 2009. Geography of Alaska Lake Districts : Identification, description, and analysis of lake-rich regions of a diverse and dynamic State. : U.S. Geological Survey Scientific Investigations Report, 2008–5215, 40 p.

Bastviken, D., 2004. Methane emissions from lakes: Dependence of lake characteristics, two regional assessments, and a global estimate. Global Biogeochem. Cycles 18, 1–12. doi:10.1029/2004GB002238

Bastviken, D., Tranvik, L. J., Downing, J. A., Crill, P. M., Enrich-Prast, A., 2011. Freshwater methane emissions offset the continental carbon sink. Science. 331, 50.

Billings, W.D., Peterson, K.M., 1980. Vegetational change and ice wedge polygons through the thaw-lake cycle in Arctic Alaska. Arctic Alpine Res. 1, 413–432.

Bliss, L.C., Peterson, K.M., 1992. Arctic Ecosystems in a Changing Climate. In Plant Succession, Competition, and the Physiological Constraints of Species in the Arctic: An Ecophysiological Perspective; Chapin, F.S., III, Jefferies, R.L., Reynolds, J.F., Shaver, G.R., Svoboda, J., Chu, E.W., Eds.; Academic Press: San Diego, CA, USA, pp. 111–136.

Bosikov, N.P., 1998. Wetness variability and dynamics of thermokarst processes in central Yakutia. Proceedings of the 7th International Conference on Permafrost, Yellowknife, Canada, pp. 71–74.

Clark, R., Ott, A., Rabe, M., Vincent-Lang, D., Woodby, D., 2010. The effects of a changing climate on key habitats in Alaska. Special Publication No. 10-14, Alaska Department of Fish and Game, 102 p.

Chen, M., Rowland, J.C., Wilson, C.J., Altmann, G.L., Brumby, S.P., 2013. The Importance of Natural Variability in Lake Areas on the Detection of Permafrost Degradation: A Case Study in the Yukon Flats, Alaska. Permafr. Periglac. Process. 24, 224–240. doi:10.1002/ppp.1783

Chen, M., Rowland, J.C., Wilson, C.J., Altmann, G.L., Brumby, S.P., 2014. Temporal and spatial pattern of thermokarst lake area changes at Yukon Flats, Alaska. Hydrol. Process. 28, 837–852. doi:10.1002/hyp.9642

Eisner, W.R., Peterson, K.M., 1998. Pollen, Fungi and Algae as Age Indicators of Drained Lake Basins near Barrow, Alaska. In Proceedings of the 7th International Permafrost Conference, Yellowknife, NWT, Canada, 23–27 June 1998; Lewkowicz, A.G., Allard, M., Eds.; Centre d'études nordiques de l'Université Laval: Quebec, QC, Canada, pp. 790–795.

Eisner W. R., Cuomo C. J., Hinkel K. M., Jones B. J., Brower R. H. Sr., 2009. Advancing landscape change research through the incorporation of Iñupiaq knowledge. Arctic, 62 (4), 429–442. doi: http://dx.doi.org/10.14430/arctic174

Engram, M., Anthony, K.W., Meyer, F.J., Grosse, G., 2012. Synthetic aperture radar (SAR) backscatter response from methane ebullition bubbles trapped by thermokarst lake ice. Can. J. Remote Sens. 38, 667–682.

French, H.M., 2007. The Periglacial Environment, Third ed., John Wiley & Sons Ltd, Chichester, West Sussex, England, 458 p. doi: 10.1002/9781118684931

Frohn, R. C., Hinkel, K. M., Eisner, W. R., 2005. Satellite remote sensing classification of thaw lakes and drained thaw lake basins on the North Slope of Alaska. Remote Sensing of Environment. 97, 116–126. doi: 10.1016/j.rse.2005.04.022

Grosse, G., Schirrmeister, L., Malthus, T.J., 2006. Application of Landsat-7 satellite data and a DEM for the quantification of thermokarst-affected terrain types in the periglacial Lena – Anabar coastal lowland. Polar Res. 51–67.

Grosse, G., Romanovsky, V., Walter, K., Morgenstern, A., Lantuit, H., Zimov, S. 2008. Distribution of thermokarst lakes and ponds at three yedoma sites in Siberia. In Ninth International Conference on Permafrost (eds. D. L. Kane and K. M. Hinkel), Institute of Northern Engineering, University of Alaska Fairbanks, 551-556.

Grosse, G., Harden, J., Turetsky, M., McGuire, A. D., Camill, P., Tarnocai, C., Frolking, S., Schuur, E. A. G., Jorgen- son, T., Marchenko, S., Romanovsky, V., Wickland, K. P., French, N., Waldrop, M., Bourgeau-Chavez, L., Striegl, R. G., 2011 Vulnerability of high-latitude soil organic carbon in North America to disturbance, J. Geophys. Res., 116, 1–23. doi:10.1029/2010JG001507

Grosse G., Jones B., Arp C., 2013. Thermokarst Lakes, Drainage, and Drained Basins. In: Shroder JF (ed.): Treatise on Geomorphology. Vol. 8, pp. 325-353. San Diego: Academic Press. doi:10.1016/B978-0-12-374739-6.00216-5

Hinkel, K.M., Eisner, W.R., Bockheim, J.G., Nelson, F.E., Peterson, K.M., Dai, X., 2003. Spatial extent, age and carbon stocks in drained thaw lake basins on the Barrow Alaska Peninsula, Alaska. Arctic, Antart. Alp. Res. 35, 291–330.

Hinkel, K.M., Frohn, R.C., Nelson, F.E., Eisner, W.R., Beck, R. a., 2005. Morphometric and spatial analysis of thaw lakes and drained thaw lake basins in the western Arctic Coastal Plain, Alaska. Permafr. Periglac. Process. 16, 327–341. doi:10.1002/ppp.532

Hinkel, K.M., Jones, B.M., Eisner, W.R., Cuomo, C.J., Beck, R. a., Frohn, R., 2007. Methods to assess natural and anthropogenic thaw lake drainage on the western Arctic coastal plain of northern Alaska. J. Geophys. Res. 112, 1–9. doi:10.1029/2006JF000584

Hinzman, L.D., Bettez, N.D., Bolton, W.R., Chapin, F.S., Dyurgerov, M.B., Fastie, C.L., Griffith, B., Hollister, R.D., Hope, A., Huntington, H.P., Jensen, A.M., Jia, G.J., Jorgenson, T., Kane, D.L., Klein, D.R., Kofinas, G., Lynch, A.H., Lloyd, A.H., McGuire, A. D.,

Nelson, F.E., Oechel, W.C., Osterkamp, T.E., Racine, C.H., Romanovsky, V.E., Stone, R.S., Stow, D. a., Sturm, M., Tweedie, C.E., Vourlitis, G.L., Walker, M.D., Walker, D. A., Webber, P.J., Welker, J.M., Winker, K.S., Yoshikawa, K., 2005. Evidence and Implications of Recent Climate Change in Northern Alaska and Other Arctic Regions. Clim. Change 72, 251–298. doi:10.1007/s10584-005-5352-2.

Hopkins, D.M., 1949. Thaw lakes and thaw sinks in the Imuruk Lake area, Seward Peninsula, Alaska. J. Geol., 57, 119–131.

van Huissteden, J., Berrittella, C., Parmentier, F.J.W., Mi, Y., Maximov, T.C., Dolman, a. J., 2011. Methane emissions from permafrost thaw lakes limited by lake drainage. Nat. Clim. Chang. 1, 119–123. doi:10.1038/nclimate1101

Jones, B.M., Arp, C.D., Jorgenson, M.T., Hinkel, K.M., Schmutz, J. a., Flint, P.L., 2009. Increase in the rate and uniformity of coastline erosion in Arctic Alaska. Geophys. Res. Lett. 36, L03503. doi:10.1029/2008GL036205

Jones, B.M., Grosse, G., Arp, C.D., Jones, M.C., Walter Anthony, K.M., Romanovsky, V.E., 2011. Modern thermokarst lake dynamics in the continuous permafrost zone, northern Seward Peninsula, Alaska. J. Geophys. Res. 116, 1–13. doi:10.1029/2011JG001666

Jones, M.C., Grosse, G., Jones, B.M., Walter Anthony, K., 2012. Peat accumulation in drained thermokarst lake basins in continuous, ice-rich permafrost, northern Seward Peninsula, Alaska. J. Geophys. Res. 117, 1–16. doi:10.1029/2011JG001766

Jones, B.M., Arp, C.D., 2015. Observing a Catastrophic Thermokarst Lake Drainage in Northern Alaska. Permafr. Periglac. Process. 119–128. doi:10.1002/ppp.1842

Jorgenson, M.T., Shur, Y., 2007. Evolution of lakes and basins in northern Alaska and discussion of the thaw lake cycle. J. Geophys. Res. 112, 1–12. doi:10.1029/2006JF000531

Jorgenson, M.T., Romanovsky, V., Harden, J., Shur, Y., O'Donnell, J., Schuur, E. a. G., Kanevskiy, M., Marchenko, S., 2010. Resilience and vulnerability of permafrost to climate changeThis article is one of a selection of papers from The Dynamics of Change in Alaska's Boreal Forests: Resilience and Vulnerability in Response to Climate Warming. Can. J. For. Res. 40, 1219–1236. doi:10.1139/X10-060

Karlsson, J., Lyon, S., Destouni, G., 2014. Temporal Behavior of Lake Size-Distribution in a Thawing Permafrost Landscape in Northwestern Siberia. Remote Sens. 6, 621–636. doi:10.3390/rs6010621.

Keller, M., Stallard, R. F., 1994. Methane emission by bubbling from Gatun Lake, Panama, J. Geophys. Res., 99, 8307–8319. doi:10.1029/92JD02170.

Koven, C. D., Ringeval, B., Friedlingstein, P., Ciais, P., Cadule, P., Khvorostyanov, D., Krinner, G., Tarnocai, C., 2011. Permafrost carbon-climate feedbacks accelerate global warming, P. Natl. Acad. Sci. USA, 108, 14769–14774. doi:10.1073/pnas.1103910108

Labrecque, S., Lacelle, D., Duguay, C.C.R., Lauriol, B., Hawkings, J., 2009. Contemporary (1951-2001) evolution of lakes in the Old Crow Basin, Northern Yukon, Canada: remote sensing, numerical modeling, and stable isotope analysis. Arctic 62, 225–238.

Lehner, B., Döll, P., 2004. Development and validation of a global database of lakes, reservoirs and wetlands. J. Hydrol. 296, 1–22. doi:10.1016/j.jhydrol.2004.03.028

Ling, F., Zhang, T.J., 2004. Modeling study of talik freeze-up and permafrost response under drained thaw lakes on the Alaskan Arctic Coastal Plain. J. Geophys. Res. 109, D01111.32.

Mackay, J.R., 1988. Catastrophic lake drainage, Tuktoyaktuk Peninsula area, District of Mackenzie. Curr. Res.-Bull. Geol. Surv. Can. 88–1D, 83–90.

Mackay, J.R.; Burn, C.R., 2002. The first 20 years (1978–1979 to 1998–1999) of ice-wedge growth at the Illisarvik experimental drained lake site, western Arctic coast, Canada. Can. J. Earth Sci. 39, 95–111.

Marsh, P., Russell, M., Pohl, S., Haywood, H., Onclin, C., 2009. Changes in thaw lake drainage in the Western Canadian Arctic from 1950 to 2000 158, 145–158. doi:10.1002/hyp

Morgenstern, A.; Grosse, G.; Günther, F.; Fedorova, I.; Schirrmeister, L., 2011. Spatial analyses of thermokarst lakes and basins in Yedoma landscapes of the Lena Delta. Cryosphere, 5, 849–867.

Osterkamp, T. E. and Romanovsky,V. E.: 1999. Evidence for warming and thawing of discontinuous permafrost in Alaska. Permafrost Periglacial Process. 10, 17–37.

Plug, L.J., Walls, C., Scott, B.M., 2008. Tundra lake changes from 1978 to 2001 on the Tuktoyaktuk Peninsula, western Canadian Arctic. Geophys. Res. Lett. 35, L03502. doi:10.1029/2007GL032303

Plug, L.J., West, J.J., 2009. Thaw lake expansion in a two-dimensional coupled model of heat transfer, thaw subsidence, and mass movement. J. Geophys. Res. 114, F01002. doi:10.1029/2006JF000740

Riordan, B., Verbyla, D., McGuire, A. D., 2006. Shrinking ponds in subarctic Alaska based on 1950–2002 remotely sensed images. J. Geophys. Res. 111, G04002. doi:10.1029/2005JG000150

Roach, J., Griffith, B., Verbyla, D., Jones, J., 2011. Mechanisms influencing changes in lake area in Alaskan boreal forest. Global Change Biology 17, 2567-2583.

Romanovsky, V.E., Smith, S.L., Christiansen, H.H., 2010. Permafrost thermal state in the polar Northern Hemisphere during the international polar year 2007-2009: A synthesis. Permafr. Periglac. Process. 21, 106–116. doi:10.1002/ppp.689

Rowland, J.C., Travis, B.J., Wilson, C.J., 2011. The role of advective heat transport in talik development beneath lakes and ponds in discontinuous permafrost. Geophys. Res. Lett. 38, 1–5. doi:10.1029/2011GL048497

Sannel, A.B.K., Brown, I.A., 2010. High-resolution remote sensing identification of thermokarst lake dynamics in a subarctic peat plateau complex. Canadian Journal of Remote Sensing 36(1), S26–S40. doi:10.5589/m10-010

Schuur, E. a. G., Bockheim, J., Canadell, J.G., Euskirchen, E., Field, C.B., Goryachkin, S. V., Hagemann, S., Kuhry, P., Lafleur, P.M., Lee, H., Mazhitova, G., Nelson, F.E., Rinke, A., Romanovsky, V.E., Shiklomanov, N., Tarnocai, C., Venevsky, S., Vogel, J.G., Zimov, S. A., 2008. Vulnerability of Permafrost Carbon to Climate Change: Implications for the Global Carbon Cycle. Bioscience 58, 701. doi:10.1641/B580807

Schuur, E.A.G., McGuire, A.D., Grosse, G., Harden, J.W., Hayes, D.J., Hugelius, G., Koven, C.D., Kuhry, P., 2015. Climate change and the permafrost carbon feedback. Nature 520, 171–179. doi:10.1038/nature14338

Sellmann, P.V., Brown, J., Lewellen, R.I., McKim, H.L., Merry, C.J., 1975. The classification and geomorphic implications of thaw lakes on the Arctic Coastal Plain, Alaska. U.S. Army Cold Regions Research and Engineering Laboratory, Hanover, New Hampshire, p. 21.

Serreze, M.C., Francis, J.A.. 2006, The Arctic amplification debate. Climatic Change, 76, 241-264.

Smith, L.C., Sheng, Y., MacDonald, G.M., Hinzman, L.D., 2005. Disappearing Arctic lakes. Science 308, 1429. doi:10.1126/science.1108142

Smith, S.L., Romanovsky, V.E., Lewkowicz, A.G., Burn, C.R., Allard, M., Clow, G.D., Yoshikawa, K., Throop, J., 2010. Thermal state of permafrost in North America: a contribution to the international polar year. Permafr. Periglac. Process. 21, 117–135. doi:10.1002/ppp.690

Solomon, S., Qin, D., Manning, M., Alley, R.B., Berntsen, T., Bindoff, N.L., Chen, Z., Chidthaisong, A., Gregory, J.M., Hegerl, G.C., Heimann, M., Hewitson, B., Hoskins, B.J., Joos, F., Jouzel, J., Kattsov, V., Lohmann, U., Matsuno, T., Molina, M., Nicholls, N., Overpeck, J., Raga, G., Ramaswamy, V., Ren, J., Rusticucci, M., Somerville, R., Stocker, T.F., Whetton, P., Wood, R.A., Wratt, D., 2007. Technical summary. In: ***Climate change 2007: The physical science basis***. Contribution of Working Group I to the Fourth Assessment Report of the Intergovernmental Panel on Climate Change, edited by Solomon,

S., Qin, D., Manning, M., Chen, Z., Marquis, M., Averyt, K.B., Tignor, M., Miller, H.L., Cambridge, UK, and New York: Cambridge University Press.

Walsh, J.E., Overland, J.E., Groisman, P.Y., Rudolf, B., 2011. Ongoing climate change in the arctic. Ambio 40, 6–16. doi:10.1007/s13280-011-0211-z

Walter, K.M., Zimov, S. a, Chanton, J.P., Verbyla, D., Chapin, F.S., 2006. Methane bubbling from Siberian thaw lakes as a positive feedback to climate warming. Nature 443, 71–5. doi:10.1038/nature05040

Walter, K.M., Smith, L.C., Chapin, F.S., 2007. Methane bubbling from northern lakes: present and future contributions to the global methane budget. Philos. Trans. A. Math. Phys. Eng. Sci. 365, 1657–76. doi:10.1098/rsta.2007.2036

Walter, K.M., Engram, M., Duguay, C.R., Jeffries, M.O., Chapin, F.S., 2008. The potential use of Synthetic Aperture Radar for estimating methane ebullition from Arctic lakes. J. Am. Water Resour. Assoc. 44, 305–315.

Walter Anthony, K., Vas, D.A., Brosius, Laura, F.S.C.I., Zimov, S.A., 2010. Estimating methane emissions from northern lakes using ice- bubble surveys. Limnol. Ocean. Methods 8, 592–609.

West, J.J., Plug, L.J., 2008. Time-dependent morphology of thaw lakes and taliks in deep and shallow ground ice. J. Geophys. Res. 113, 1–14. doi:10.1029/2006JF000696

Yoshikawa, K., Hinzman, L.D., 2003. Shrinking thermokarst ponds and groundwater dynamics in discontinuous permafrost near council, Alaska. Permafr. Periglac. Process. 14, 151–160. doi:10.1002/ppp.451

Zimov, S.A., Voropaev, Y.V., Semiletov, I.P., Davidov, S.P., Prosiannikov, S.F., Chapin III, F.S., Chapin, M.C., Trumbore, S., Tyler, S., 1997. North Siberian Lakes: A Methane Source Fueled by Pleistocene Carbon. Science, 277, 800–802. doi:10.1126/science.277.5327.800

Zimov, S. A, Schuur, E. A. G., Chapin, F.S., 2006. Permafrost and the global carbon budget. Science, 312, 1612–16133. doi:10.1126/science.1128908

Zona, D., Oechel, W.C., Peterson, K.M., Clements, R.J., Paw U, K.T., Ustin, S.L., 2010. Characterization of the carbon fluxes of a vegetated drained lake basin chronosequence on the Alaskan Arctic Coastal Plain. Glob. Chang. Biol. 16, 1870–1882. doi:10.1111/j.1365-2486.2009.02107.x

Zhang, T., Barry, R.G., Knowles, K., Heginbottom, J.A., Brown, J., 2008. Statistics and characteristics of permafrost and ground-ice distribution in the Northern Hemisphere. Polar Geogr. 31, 47–68. doi:10.1080/10889370802175895

Chapter 2. An object-based classification method to detect methane ebullition bubbles in early winter lake ice[1]

2.1. Abstract

Thermokarst lakes in the Arctic and Subarctic release carbon from thawing permafrost in the form of methane and carbon dioxide with important implications for regional and global carbon cycles. It is difficult to accurately measure methane flux from these lakes due to challenges associated with logistics of fieldwork and the heterogeneous nature of gas ebullition, a dominant pathway of methane release from lake bottoms to the atmosphere. Lake ice impedes the release of methane gas during the winter resulting in vertically oriented bubble columns in the ice that are visible on the lake surface. Ebullition bubbles appear as white patches on high-resolution optical remote sensing images of snow-free lake ice acquired in early winter and thus can be mapped over the whole lake area. The information derived from high-resolution optical images of early winter lake ice can supplement often spatially limited field sampling methods to better estimate methane flux from individual lakes but also from numerous lakes within larger regions. But reaching this goal requires an appropriate image classification method that can extract methane ebullition bubble patches from an image for further analysis. In this paper we describe a classification technique using an Object-Based Image Analysis (OBIA) framework to successfully map ebullition bubbles trapped in early winter lake ice of an of an interior Alaska thermokarst lake. We used high-resolution (9-11 cm) aerial images acquired two and four days following freeze up in the years 2011 and 2012, respectively. The design of multiresolution segmentation and region-specific rulesets allowed the identification of bubble features and separation from other confounding factors such as snow, submerged vegetation, shadows, and open water. The OBIA technique revealed an accuracy of >95% for mapping ebullition bubble patches in early winter lake ice.

[1]Lindgren, P. R., Grosse, G., Meyer, F. J., Walter Anthony, K. M., Detection and spatiotemporal analysis of methane ebullition on thermokarst lake ice using high-resolution optical aerial imagery, *In preparation for ISPRS Journal of Photogrammetry and Remote Sensing*.

2.2. Introduction

Ebullition or bubbling is the dominant pathway of methane release from many lakes to the atmosphere, however, the spatiotemporal heterogeneity of bubbling makes it challenging to quantify ebullition emissions (Keller and Stallard, 1994; Bastviken et al., 2011). Vertically oriented bubbles are visible on the lake ice surface in high latitudes when seasonal lake ice cover prevents the release of methane to the atmosphere. Bubbles emerging from the lake bed ascend through the water column and get trapped under the ice cover as bubble-shaped gas pockets (Walter et al., 2008). Lake ice growth results in enclosure of the bubbles in the ice, preserving a seasonal record of ebullition events in the ice column over a specific location. This temporary preservation provides an opportunity to quantify spatial distribution and characteristics of methane bubbles and to correlate seep fluxes with trapped bubble size (Walter et al., 2006; Walter Anthony et al., 2010). Due to logistical challenges of fieldwork and due to the remote locations of the lakes, an accurate estimation of methane flux is still difficult. However, remote sensing methods combined with field observations can overcome some of the limitations that come with a detailed but spatially restricted field-survey approach. Previous studies have shown the ability of space-borne Synthetic Aperture Radar (SAR) images to detect vertically-oriented tubular gas bubbles trapped in ice (Jeffries et al., 1994; Jeffries et al., 2005; Duguay and Lafleur, 2003) and demonstrated its potential application to quantify methane emissions from thermokarst lakes at the lake scale (Walter et al., 2008; Engram et al., 2012). Ebullition bubbles are potentially visible on high-resolution optical images of lake ice in early winter if snow-free ice cover conditions exist during the image acquisition time (Lindgren et al., 2016) (Figure 2.1). These bubbles are seen as white patches against contrasting dark bubble-free black lake ice. We refer to the bubble features seen in our images as 'bubble patches' henceforth.

The availability of regular or on-demand high resolution optical images and recent developments in image analysis techniques have opened promising avenues for exploring their potential applications to understanding methane ebullition variability and improving estimates of methane emission from thermokarst lakes. It is thus important to have an appropriate image classification method that allows mapping methane ebullition bubbles from an image for further analysis. Depending on the image quality and lake ice conditions, bubble extraction generally can be a challenging task.

Many advanced classification approaches for high resolution images are available based on either per-pixel, sub-pixel, or image objects (Lu and Weng, 2007); however, Object-Based Image Analysis (OBIA) has proved to be the most suitable approach for classification of such imagery (Baatz et al., 2008; Blaschke, 2010; Blaschke et al., 2014). In contrast to traditional pixel-based image analysis methods that classify individual pixels directly based on spectral characteristics and can group pixels based on their spectral features similarity into classes, OBIA involves additional steps. First it aggregates pixels based on their spatial and spectral homogeneity into meaningful clusters known as image objects and then classifies individual objects in the second step using the objects' spatial, spectral, textural, and contextual information (Liu and Xia, 2010). Furthermore, statistical summaries pertaining to objects can be integrated from useful auxiliary and thematic data for classification. Additionally, OBIA allows segmentation of image objects with different scale, shape, and spectral parameters while preserving the objects' properties and relationships to each other via an object-hierarchy. This approach helps to decompose a complex scene into understandable objects of desired scales, provides an opportunity to develop a conceptual framework to organize image objects in a semantic network, and thus allows us to integrate knowledge-based classification procedures or rulesets specific to objects of interest that cannot be achieved through pixel-based image analysis (Baatz and Schäpe, 1999; Lang, 2008) (Figure 2.2). For example, a high-resolution image can be first decomposed at coarser scales to delineate large image features, e.g. such as types of forest. In the following steps each forest type can be further segmented at finer scales and localized classification rulesets can be designed for each forest type to characterize the tree canopies that make up the respective forest types. The process can go on further depending on the type of scenes until the final target objects are well captured. Through such repeated segmentation and localized classification built following a structured semantic framework of image objects, a higher accuracy of classification compared to traditional pixel-based classification techniques can be achieved with OBIA (Baatz et al., 2008; Lang, 2008).

OBIA techniques have been extensively used to map urban features (Herold et al., 2002; Mathieu et al., 2007; Lackner and Conway, 2008; Moskal et al., 2011; de Pinho et al., 2012; Novack et al., 2014), to derive forest stand-level inventory information (Hay et al., 2005; Bunting and Lucas, 2006; Chubey et al., 2006), to monitor biodiversity and wildlife habitat

(Bock et al., 2005; Förster et al., 2008; Kamal and Phinn, 2011), and also to estimate relative abundance of wildlife (Groom et al., 2011). Similar object-based approaches can be appropriate to map individual ebullition bubble patches that are visible on early winter lake ice.

We recently highlighted the application of high-resolution aerial images to study methane ebullition dynamics on a thermokarst lake located in interior Alaska with a focus on intra-lake distribution patterns of ebullition and inter-annual ebullition dynamics (Lindgren et al., 2016). In this paper, we lay out in detail the OBIA technique used to identify methane ebullition bubble patches on early winter lake ice in very high-resolution optical remote sensing images. We especially focus on the multiresolution segmentation approach and the region-specific rulesets designed for extracting methane ebullition bubbles, which have the potential to be applied to other lakes with similar ice cover characteristics.

2.3. Study area

Goldstream Lake (informal name) is a thermokarst (thaw) lake located near Fairbanks, Alaska (Figure 2.1). The lake covers an area of approximately 10,300 m^2. The maximum and average depths of the lake are 2.9 and 1.6 m, respectively. Historical aerial and recent satellite images show that the lake drained partially after the year 1949 but has been expanding mainly along the eastern shore since then (Walter Anthony and Anthony, 2013; Lindgren et al., 2016). This active thermokarst expansion is also clearly indicated by a steep shore with spruce trees leaning inwards along the eastern lake perimeter.

The lake usually freezes between the end of September to mid-October and break up occurs around the end of April or early May. In winter when the lake is frozen, vertically oriented layers of methane ebullition bubbles are seen in the lake ice (Walter Anthony and Anthony, 2013; Lindgren et al., 2016). High concentrations of methane bubbles and numerous methane bubbling open-hole hotspots, which remain mostly ice-free throughout the winter, are found along the eroding part of the lake shore where permafrost is thawing and released soil organic carbon fuels microbial activity on the lake bottom (Brosius et al., 2012; Walter Anthony and Anthony, 2013; Lindgren et al., 2016). Cattails (*Typha spp.*) and water lilies (*Nuphar spp.*) grow in shallow parts of the lake. Some dead but still standing spruce tree trunks are found in the eastern margin of the lake also indicating lake expansion.

2.4. Data

2.4.1. Remotely sensed high-resolution images

For this study low altitude, sub-meter spatial resolution aerial images to map methane ebullition bubbles in the early winter lake ice were utilized (Table 2.1). Image acquisitions were scheduled on 14 October 2011 and 13 October 2012 in nadir-looking imaging geometry, two and four days following freeze-up, respectively, when the ice was still snow-free and methane ebullition seeps were still visible. Images (5 in year 2011, 8 in year 2012) were acquired with a Nikon D300 camera system mounted in the bellyport of a Navion L17a plane that was aligned with a Global Positioning System (GPS). Flight altitudes for the acquisitions were ~750 m asl in 2011 and ~587 m asl in 2012. Image scales were 1:20,000 and 1:17,000, respectively for 2011 and 2012, which in turn corresponds to ground sampling distances (GSD) of 11 cm and 9 cm. All the images consisted of the three visible bands red, green, and blue (RGB).

2.4.2. Ground control points

We collected the complete lake perimeter data and locations of stationary objects such as markers installed on and around the lake shore, and a LiCor methane analyzer installed on a wooden platform in the lake using a survey-grade LEICA VIVA™ real time kinematic Differential Global Positioning System (DGPS) sensors with centimeter-accuracy in 2011 and 2012 when the lake was frozen and was safe to walk on. We also surveyed other identifiable reference points such as cattail vegetation on the lake.

2.5. Methods

2.5.1. Image processing: Image rectification and transformation

In an initial step, 5 and 8 images for 2011 and 2012, respectively, of Goldstream Lake were mosaicked using Agisoft PhotoScan Professional Software™ Version 0.9.0 to create a single image product that covered the entire lake. We then performed a geometric correction of the aerial image mosaic acquired in October 2012. The 2012 DGPS data of the corners of small peninsulas, lake edge and identifiable vegetation on the lake served as ground control points (GCPs) for image rectification. A total of 22 GCPs were used to determine the parameters of a second order polynomial function for geometric correction of the image using the ENVI™

(version 4.8) image processing software. The total Root Mean Square Error (RMSE) of the polynomial fit was 0.07 m. The image was projected to NAD 83 UTM Zone 6. The corrected 2012 image was then used as the base image to rectify the October 2011 image since there was no significant change in lake margin position between these years. We utilized a high-resolution (1 m), orthorectified Digital Orthophoto Quarter Quadrangle (DOQQ) aerial image of the lake region from 2007 as well as the DGPS points of stationary objects collected in 2011 to confirm the accuracy of image rectification

After the image was transformed and rectified into the UTM Zone 6 coordinate system, a spectral transformation using the Unstandardized Principal Component Analysis (PCA) in the ENVI™ image processing software was used on all three visible bands of the final lake image mosaic. PCA is a feature-space linear transformation that has been widely used in remote sensing for image processing (Schowengerdt, 2007; Mather and Koch, 2011). PCA transforms a set of correlated variables within a dataset into a set of values or components of linearly uncorrelated variables that are orthogonal to each other. The transformation outputs principal component (PC) bands in such a way that the first principal component has the variables that account for the most variance in the dataset, and each succeeding independent component in turn contains less information than the preceding one. The information decreases with increasing PC bands and the most information is available in the first few bands. In this case, PCA is used for the decomposition of spectral information distributed in the three optical RGB bands into a set of three uncorrelated PC bands that can represent some specific physical processes governing the image data. PCA thus removes any redundant information and since it outputs bands in terms of variance explained, it can help enhance the image information by separating dominant spatial patterns in the first PC component with high contrast such as methane bubble patches in the image (Zhang, 2002; Rodarmel and Shan, 2002; Lu et al., 2011).

2.5.2. Image object structure and classification model

We decomposed the scenes into eight meaningful regions associated with respective image object classes such as lake, lake shore, vegetation in lake ice, dark ice, white ice, bubbles etc. (Figure 2.3). We then organized them in a conceptual image object hierarchy creating a semantic network between different sized objects (Figure 2.2) such that the final target features, ebullition bubble patches, were at the bottom of the hierarchy (Figure 2.3). We created a four-level image

object hierarchy. In terms of spatial scale, the regions associated with super-objects on the upper level of the hierarchy were coarser than the regions associated with sub-objects on the lower level of the hierarchy. For example, a lake is a super-object composed of sub-objects associated with different lake ice characteristics such as lake ice with vegetation, whereas sub regions of specific lake ice characteristics such as white and dark ice are super-objects of the final target feature (ebullition bubble patches).

2.5.2.1. Multiresolution segmentation

At each level, we performed multiresolution segmentation on RGB, PC 1 and PC 2 bands to create image objects. PC band 3 was discarded due to its low information content and high noise level. Multiresolution segmentation is based on a bottom-up region merging segmentation approach starting with single seed pixels or one-pixel objects. It then starts merging pixels or merging smaller objects to larger objects at each step until the 'degree of fitting' assigned to homogeneity criteria is fulfilled (Baatz and Schäpe, 2000; Benz et al., 2004). There are four criteria for estimating heterogeneity between objects: (1) color, (2) shape, (3) smoothness, and (4) compactness (Benz et al., 2004; Definiens, 2007a; Frohn et al., 2011). In eCognition for multiresolution segmentation, heterogeneity is defined by:

$$f = w_{color} \cdot h_{color} + w_{shape} \cdot h_{shape} \quad \text{(Equation 2.1)}$$

$$w_{color} \in [0,1] \; and \; w_{shape} \in [0,1] \; w_{color} + w_{shape} = 1 \quad \text{(Equation 2.2)}$$

w_{shape}: User-defined parameter to modify shape and color criteria. w_{color} is calculated from w_{shape}. It allows users to define to which percentage spectral values of image layers will contribute to the entire homogeneity criterion. w_{shape} was set to 0.5.

h_{color} is spectral heterogeneity that allows multi-variant segmentation by assigning a weight w_c to the image bands, c, and is defined by

$$h_{color} = \sum_c w_c \left(n_{merge}\sigma_c^{merge} - \left(n_{obj\_1}\sigma_c^{obj\_2} + n_{obj\_2}\sigma_c^{obj\_2} \right) \right) \quad \text{(Equation 2.3)}$$

Subscript 'merge' refers to the merged objects

Subscripts 'obj_1' and 'obj_2' refer to neighboring object pairs prior to merge.

n: Number of pixels within image object.

σ_c: Standard deviation within image object band c.

w_c: User-defined parameter that allows image layers to be weighted depending on their

suitability for the segmentation result. The highest weight was given to PC bands 1 and 2 since they carried more useful non-redundant information. The RGB band weights were set to 1 and PC band weights were set to 2 (i.e. double the weight of RGB bands).

h_{shape} is shape heterogeneity estimated based on smoothness and compactness.

$$h_{shape} = w_{cmpct} \cdot h_{cmpct} + (1 - w_{cmpct})\, h_{smooth} \qquad \text{(Equation 2.4)}$$

w_{cmpct}: User-defined parameter to optimize image objects with regard to compactness. It was set to 0.5.

$$h_{smooth} = n_{merge} \frac{l_{merge}}{b_{merge}} - \left(n_{obj\_1} \frac{l_{obj\_1}}{b_{obj\_1}} + n_{obj\_2} \frac{l_{obj\_2}}{b_{obj\_2}} \right) \qquad \text{(Equation 2.5)}$$

$$h_{cmpct} = n_{merge} \frac{l_{merge}}{\sqrt{n_{merge}}} - \left(n_{obj\_1} \frac{l_{obj\_1}}{\sqrt{n_{obj\_1}}} + n_{obj\_2} \frac{l_{obj\_2}}{\sqrt{n_{obj\_2}}} \right) \qquad \text{(Equation 2.6)}$$

l : Image object perimeter

b : Perimeter of an image object's bounding box

The merging process stops when the maximum heterogeneity of two merging objects exceeds the one determined by the user-defined scale parameter (Baatz and Schäpe, 2000; Benz et al., 2004). The scale parameter is an abstract term defined to set a threshold to control the growth of image objects. The parameter value can range between 1 and 100. This procedure allows all image objects to grow in a simultaneous way such that output image objects are of comparable size and scale. A larger scale parameter allows more objects to fuse and thus results in larger image objects. In this study, different scale parameters (10, 15, 50, 100) were chosen depending on the size of the smallest objects of interest for a particular level (Figure 2.4), which we have explained in the next section 2.5.2.2.

2.5.2.2. Object-based classification

We developed rule-based classifiers at each decomposition level to tag segmented image objects with their associated class for which we integrated spectral, shape, and spatial information pertaining to objects for classification. The following explains the processes and region-specific rulesets designed at each level in detail (Table 2.2).

In Level I, we performed multiresolution segmentation on the whole image using a scale factor of 100 to identify two major regions in the image: (1) Lake and (2) Lake shore. The classification was based on grey values of PC 2 band, as well as size and spatial information

pertaining to image objects. We first used a threshold value on PC 2 to separate Lake from Lake Shore. However, some small segments in Lake Shore were still misclassified as Lake and vice-versa. Therefore, we re-classified misclassified objects based on their size and their spatial location. For example, we reclassified small misclassified objects (misclassified as Lake) enclosed by the Lake Shore as Lake Shore. Similarly, small segments of Lake Shore enclosed by Lake were reclassified as Lake.

In the second level, Level II, we further classified sub-regions within Lake: (1) Lake Ice with Vegetation, (2) Lake Ice without Shadow, and (3) Lake Ice with Shadow. In the first step, we applied a chessboard segmentation (Definiens, 2007a) on Lake resulting in pixel size segments (Figure 2.4) and ran a multiresolution segmentation using a scale factor of 15. This is an important step since multiresolution segmentation starts with single pixel object. We chose a small-scale parameter for segmentation to capture small water lily pads trapped in ice. PC 2 band was used to separate Lake Ice with Shadow, Lake Ice without Shadow and Vegetation. The size of image objects and spatial information pertaining to neighboring objects were used to refine the classification between lake ice with and without shadow. For example, following the examination of the shadow characteristics on the lake, any remaining small patches of Lake Ice without Shadow enclosed by Lake Ice with Shadow were re-classified as Lake Ice with Shadow since tall spruce trees on the southern margin of the lake had overcast a contiguous shadow along the southern part of the lake.

At the third level, Level III, we further classified lake ice based on ice characteristics into two classes (1) Dark Ice, and (2) White Ice. For this, we developed classifiers specific for lake ice type (with shadow and without shadow). Both classifiers involved multiresolution segmentation on both shadowed and not shadowed regions with a scale factor of 50. PC 1 band was then used to classify Dark Ice and White Ice, respectively.

In the fourth level, Level IV, we created rulesets to identify ebullition bubble patches trapped in specific lake ice zones identified in Level III; (1) Dark Ice – Lake Ice with Shadow (2) White Ice - Lake Ice with Shadow (3) Dark Ice - Lake Ice without Shadow (4) White Ice - Lake Ice without Shadow. The first two classes are sub-objects of Lake Ice with Shadow and the last two are of Lake Ice without Shadow. We classified bubble patches in three main stages: (1)

identification of Bubble Patch edge, (2) identification of Bubble Patch center and (3) Bubble Patch edge and center were merged into one class 'Bubble Patch'.

The first step involved multiresolution segmentation on Level III objects using a scale factor of 10. We then applied Canny Edge Detection algorithm to detect Bubble Patch edge on PC 1 band. The area enclosed by Bubble Patch edges was classified as Bubble Patch center.

The Canny edge detector performs localized edge detection to identify a single strong edge with low error rates (Canny, 1986; Definiens, 2007b). To achieve this, the algorithm uses the following steps: (1) it smooths the image to eliminate any noise using Gaussian filters; (2) it calculates intensity gradients on the filtered image and outlines the area with high spatial derivatives; (3) it uses an edge thinning technique called non-maximum suppression, which suppresses any pixels at non-maxima to place an edge at local maxima; (4) finally, it applies a thresholding method called 'hysteresis' to refine the edge. This technique uses two thresholds to reduce streaking and tracks along the remaining pixels to check if the magnitude falls below the first threshold or above the second threshold to either suppress them or to make edge respectively. Pixels that lie between two thresholds are accepted if they are connected to pixels with strong response, i.e. the gradient between these neighboring pixels are above the second threshold.

We then chose a threshold value on the output layer generated by the Canny edge detector to delineate the Bubble Patch edge. We set a non-conservative threshold value that allowed detection of weak edges. On the downside, this led to unrealistic shapes of objects due to overestimation of edge pixels. Therefore, we used spectral and spatial information in the rulesets for shaping the Bubble Patch edges. For this, we segmented Bubble Patch edges into pixel-sized objects using chessboard segmentation. We checked the spatial relationship between individual pixel-size Bubble Patch edge objects and their respective Bubble Patch center. If the Bubble Patch edge image object did not share a border with Bubble Patch center (i.e. parameter 'Border To' = 0 in eCognition) then we disassociated such misclassified object from the Bubble Patch edge. We re-evaluated the spectral characteristics of image objects neighboring the Bubble Patch center in the next iteration to avoid reducing the Bubble Patch area in this process. If the image objects met the spectral threshold criteria on PC 1 band, then we reclassified them as Bubble

Patch edge again. Finally, Bubble Patch edge and Bubble patch center were merged into one Bubble Patch object class.

In the final stage, we checked the neighboring pixels around a Bubble Patch to find any missing Bubble Patch areas followed by a simple Contrast and Split segmentation that separated clusters of Bubble Patches that were mapped in one single Bubble Patch. First, we segmented the neighboring lake ice around the Bubble Patches into single pixel-size objects using chessboard segmentation. Then we re-classified segmented lake ice pixels as Bubble Patches and merged them if they met a certain threshold criteria based on PC 1 band values. We applied the Contrast Split algorithm to break clusters of fused Bubble Patches into individual Bubble Patches. We set a threshold on the PC 1 band for the algorithm to keep 'dark objects' (values below PC 1 threshold) as Bubble Patches whereas to disassociate 'bright objects' (values above PC 1 threshold) from the Bubble Patch class. Contrast and split segmentation is a simple segmentation technique that involves choosing a threshold value for the algorithm to maximize the contrast between bubble patches and dark lake ice with the goal of separating them into dark (consisting of pixels below the threshold) and bright objects (consisting of pixels above the threshold) (Definiens, 2007b). Occasionally, this process can degrade the shape of bubble patches. Therefore, following another chessboard segmentation, we iteratively re-assigned the unclassified pixel size objects neighboring Bubble Patches with 'Border To' > 0 as Bubble Patches until all of the missing bright bubble pixels are reclassified and merged. In the final step, we applied the opening morphological filter for the final demarcation of the Bubble Patches.

2.6. Accuracy assessment

Ebullition is both spatially and temporally heterogeneous. This behavior can lead to discrepancies in number of seeps and seep morphology between bubble observations from an early stage of lake ice formation with that from a few weeks later when ice is thicker and again in early spring when ice starts to melt (Wik et al., 2011; Lindgren et al., 2015). Due to thin lake ice conditions during the image acquisition days, it was not feasible to collect ground truth data of ebullition bubble patches for the purpose of accuracy assessment. Therefore, we compared the ebullition bubble mapping results with manually identified bubble features in image segments that served as ground truth sample data for classification accuracy assessment. Multiresolution segmentation with a scale factor 10 was applied on the image to create image objects that we

randomly selected to manually classify them as Bubble and No Bubble for ground truth samples. It is important to note that despite the use of a set of image objects as reference information, we did not check the classification accuracy in terms of an object's geometry or boundary delineation. We performed a quantitative site-specific accuracy assessment using an error metric (Congalton and Green, 1999; Lang, 2008) that only checks the agreement of object classes between manually classified reference samples and object-based classification results.

2.7. Results and discussion

2.7.1. Principal Component Analysis

PCA performed very well in de-correlating redundant information distributed in visible bands into different band components that consisted of independent dominating patterns of interest on the lake ice. The first two PC bands carried greater than 98% of the total variance. It is clearly visible that methane bubble patches that appear as bright white spots in the natural color composite have very low grey values and are easily separable from the surrounding lake ice in PC 1 band (Figure 2.5), i.e. true brightness of bubble patches in natural color composite corresponded to low PC 1 grey values. Non-bubble objects such as cattails growing in lake water and along the lake perimeter, floating lily pads had low PC 1 grey values similar to bubble patches as well. However, in PC 2 band vegetation carried the lowest grey values allowing us to separate them from bubble patches in the consecutive classification steps (Figure 2.5).

2.7.2. Segmentation and classification

The OBIA approach reduced the complexity of imagery and allowed establishment of relationships between features through decomposition of the images into meaningful image objects. It helped to establish a structured semantic network between image objects to integrate a knowledge-based classification. Thus, we were able to develop region-specific rulesets by integrating local context information. A non-linear repeated image segmentation and classification helped to refine image objects until the target objects were identified more accurately. The multi-level segmentation and classification rulesets that we adopted performed very well to identify the final target objects, ebullition bubble patches. Bubble patches were mapped with an accuracy of 95.1 % and 98 % for the year 2011 and 2012 respectively (Figure

2.6). The errors were associated with misclassification of bubble patches with small patches of white ice and vegetation that spectrally appeared bright like bubbles on aerial images.

We mapped 1195 (0.119 seeps m^{-2}) and 1860 (0.185 seeps m^{-2}) ebullition bubble patches on 2011 and 2012 images, respectively. The percent surface area of lake ice covered with ebullition bubble patches for 2011 was 2.14% and for 2012 was 2.67%. We found that PC 1 grey values for bubble patches were in the ranges between 0-235 for the year 2011 and 0-90 for the year 2012. In both years ebullition bubble patches were more concentrated towards the eastern thermokarst lake shore indicating permafrost degradation as a driver of methane production in Goldstream Lake (Brosius et al., 2012; Walter Anthony and Anthony, 2013; Lindgren et al., 2016). Ebullition seepage, and thus methane production, was lower towards the center of the lake. This likely is due to depletion of ancient labile carbon and lack of significant sediment accumulation and organic matter input at the lake center due to the larger distance from eroding shores (Brosius et al., 2012; Kessler et al., 2012).

The presence of a large number of ebullition bubble patches as well as their increased brightness in 2012 can be explained by differences in atmospheric pressure conditions around the image acquisition time compared to 2011. Additionally, there was a longer interval between the time of freeze-up and aerial image acquisition date in 2012 compared to 2011 (4 days in 2012 vs. 2 days in 2011) that allowed more time for seep expression. Lindgren et al., 2016 noticed a significant air pressure during the week preceding image acquisition in October 2012 that allowed methane that previously accumulated in the sediment during high-pressure days to overcome the hydrostatic load and rise up into the water column, manifesting themselves as larger numbers of bubbles and larger bubble sizes in the lake ice compared to the October 2011 situation. In contrast, air pressure change in October 2011 was not large enough to enhance ebullition before the image was acquired. Previous studies have shown that atmospheric pressure dynamics can strongly impact bubbling rate over short time periods, resulting in different ice-bubble patterns between years (Mattson and Likens, 1990; Varadharajan, 2009; Casper et al., 2000; Glaser et al., 2004; Tokida et al., 2005; Scandella et al., 2011). Ebullition is enhanced following the fall of hydrostatic pressure triggered by changes in air pressure or after a sufficient volume of gas is produced in the sediment that allows bubble tubes or gas conduits in the lake-

sediments to open or dilate (Scandella et al., 2011). A detailed geophysical analysis of the extracted bubble patch information can be found in Lindgren et al. (2016).

2.7.3. Implications and future directions

We were able to map ebullition bubble patches on the entire lake surface with high accuracy using aerial imagery. The mapping results from this study are a valuable resource to study the spatiotemporal dynamics of ebullition bubbles (Lindgren et al., 2016). This has an advantage over traditional field survey methods that have challenges associated with logistics of fieldwork in remote locations and spatiotemporal heterogeneity of ebullition (Casper et al., 2000; Bastviken, 2004; Wik et al., 2011; Walter Anthony and Anthony, 2013). This approach can supplement often spatially limited field sampling methods to better understand ebullition dynamics and to better estimate methane flux from lakes. The OBIA bubble mapping method we described here can be applied to other snow-free ice-covered thermokarst and non-thermokarst lakes within larger regions. Therefore, future study should be directed towards advancing the use of optical remote sensing to detect methane bubbles trapped in lake ice that would enhance the ability for quantifying methane flux at the regional scale more accurately. Furthermore, this offers a huge potential for utilizing information derived from remotely sensed imagery in conjunction with field-based observations to assess biogeochemical processes in lakes, the regional carbon cycle and the associated feedbacks.

2.8. Conclusion

Recent research has shown that permafrost thaw releases organic carbon to thermokarst lakes. Microbial decomposition of permafrost carbon under anaerobic conditions in lake sediments results in the formation of methane, a potent greenhouse gas that escapes lakes primarily by ebullition. Due to the heterogeneous nature of ebullition and the logistical difficulties of field surveys in remote locations, where most of these lakes are located, accurately estimating methane emission from thermokarst lakes is still a challenging task. We developed a method using very high-resolution optical remote sensing imagery to map methane ebullition in winter lake ice. Object-based image analysis proved to be efficient in identifying 1195 and 1860 bubble clusters on lake ice with a high accuracy of > 95% for the years 2011 and 2012 for a thermokarst lake in interior Alaska. This classification framework can be applied on other ice-covered lakes

to derive useful information that can complement field-based surveys to understand spatiotemporal dynamics of methane ebullition and identify variables that control the methane ebullition dynamics. Optical remote sensing-based lake ice classifications will be helpful to better estimate methane emission from cold-climate lakes at regional scales.

2.9. Acknowledgement

We thank Jessie Cherry for aerial image acquisitions. This study was supported by NASA Carbon Cycle Science grant #NNX11AH20G. Additional support came from ERC #338335.

2.10. Figures

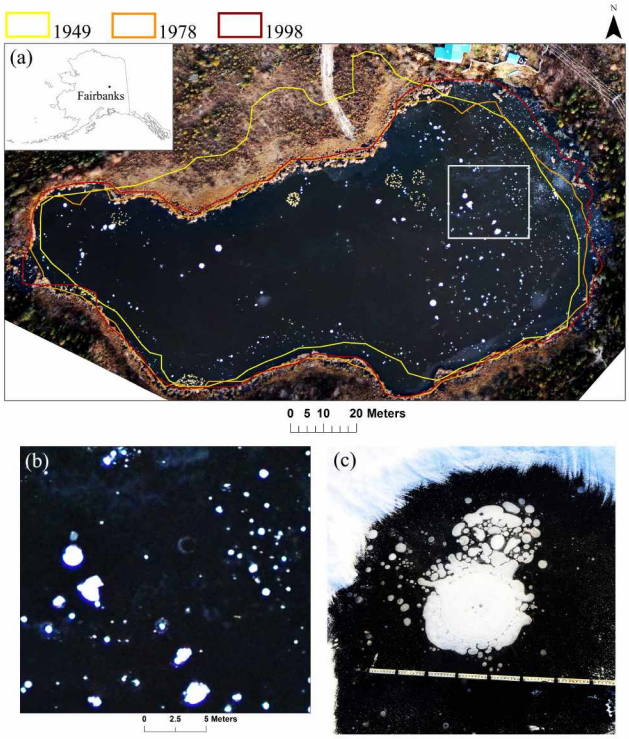

Figure 2.1. **(a)** Natural color composite of an aerial image of Goldstream Lake, Fairbanks, Alaska acquired on 13 October 2012. **(b)** A closer view of lake ice (outlined in black box in the lake image **a**) shows the appearance of ebullition bubble patches as bright white spots on the aerial image. **(c)** is an example of methane ebullitions bubbles trapped in lake ice as seen on ground.

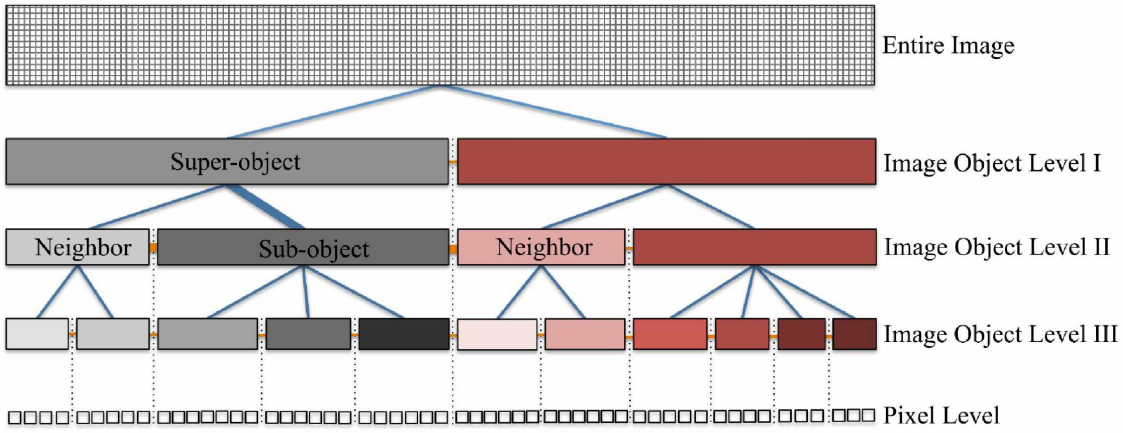

Figure 2.2. Schematic diagram showing links between image objects in OBIA (Benz et al., 2004; Definiens, 2007c). Objects on the same level are neighbors, at the upper level they are 'super-objects', and at the lower level they are 'sub-objects'. Thick orange lines show links between example image objects at the same level (neighbors) and thick blue lines show links at different levels (super-or sub-object). An image is segmented into appropriate image objects at different levels and classified by assigning each object to a class based on features and criteria set by the user.

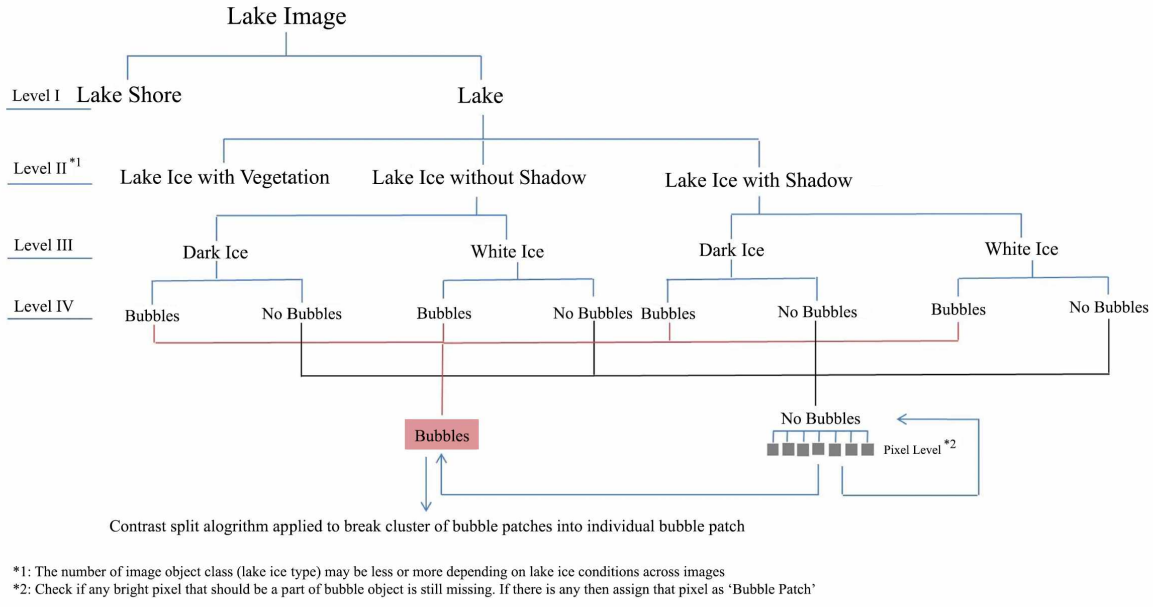

Figure 2.3. Image object hierachry to identify ebullition bubble patches on early winter lake ice.

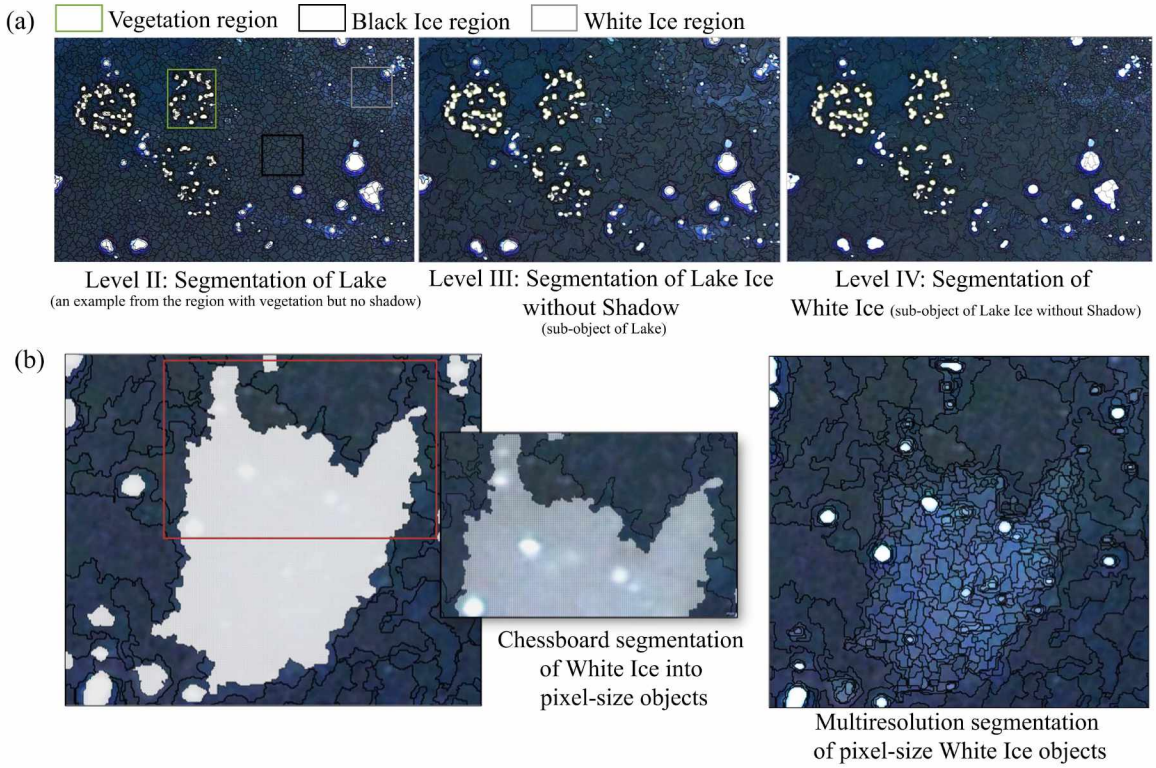

Figure 2.4. (a) Multiresolution segmentation results showing transition of target image objects in terms of shape and size from one level to another. Notice how segmentation is performed at different levels. The entire lake area comprised of vegetation, dark and white ice is segmented (scale factor = 15) in Level II to separate these sub regions. In Level III, only the region with Lake Ice without Shadow comprised of dark and white ice is segmented (scale factor = 50) and only White Ice is segmented (scale factor = 10) in Level IV. **(b)** An example of chessboard segmentation to create pixel-size objects followed by multiresolution segmentation on White Ice image objects to identify bubble patches within the white ice region.

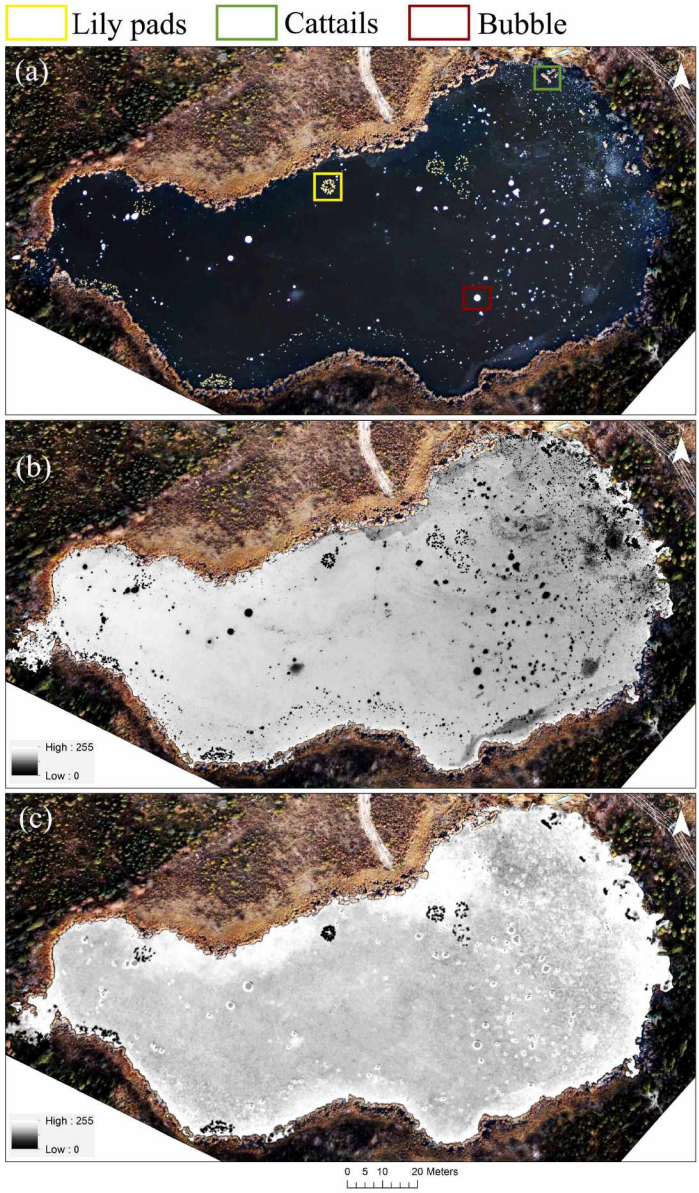

Figure 2.5. Natural color composite aerial image of Goldstream Lake, Fairbanks, Alaska acquired on 13 October 2012. **(b)** PC 1 band of image show in **a**. Bubble patches that appear bright in natural color composite in **a** have very low grey values in PC 1 band. Area highlighted in red box is an example. Vegetation such as a cluster of lily pads (yellow box) or cattails (green box) also appears dark in PC 1 band. **(c)** PC 2 band of image shown in **a**. Vegetation is separable from bubble patches. Bubble patches have higher grey values compared to vegetation and appear grey. *Note: The land area around the lake in* ***b*** *and* ***c*** *is shown in natural color composite.*

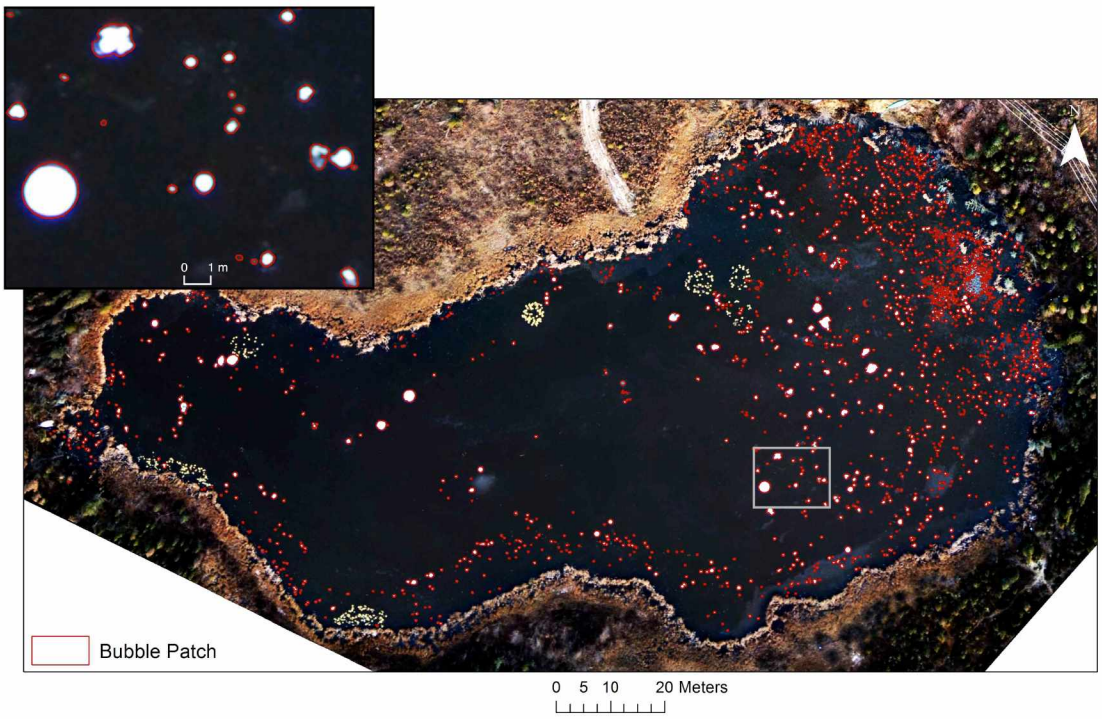

Figure 2.6. Bubble Patch map of Goldstream Lake, Fairbanks overlaid on natural color composite of aerial image acquired on 13 October 2012.

2.11. Tables

Table 2.1. List of aerial images of Goldstream Lake, Fairbanks, used in this study

Imagery	Scale	Ground Sampling Distance	Date/Year
Aerial imagery [Nikon D300 photo camera]	1:20,000	11 cm	14 October, 2011
Aerial imagery [Nikon D300 photo camera]	1:17,000	9 cm	13 October, 2012
Aerial imagery [Digital Orthophoto Quarter Quadrangle (DOQQ), orthorectified, USGS]	NA	1 m	2007

Table 2.2. Description of image objects levels, segmentation and classification methods

Level	Purpose	Segmentation	Classification	
			Criteria	eCognition Functions
II	Separate Lake from Lake Shore	- Multiresolution segmentation on Red, Green, Blue, PC 1, and PC 2 on the whole image	- Threshold on PC 2 to label image objects - Size of image objects to remove misclassified small lake image objects in the shore area. - Spatial relationship to Lake and Lake shore objects - Merge image objects of same class	- Assign - Merge - Enclosed by
III	Identify sub-regions of lake: Lake Ice with Shadow, Lake Ice without Shadow, and Vegetation in Lake	- Chessboard segmentation of lake object class - Multiresolution segmentation on Red, Green, Blue, PC 1, and PC 2 to segment lake object class	- Threshold on PC 2 to label image objects - Size of image objects to remove misclassified lake ice types: Lake Ice with Shadow and without Shadow - Spatial relationship of Lake Ice with Shadow and Lake Ice without Shadow - Merge image objects of same class	- Assign - Merge - Enclosed by
IIII	Identify dark and white ice within Lake Ice with Shadow and without Shadow	- Chessboard segmentation of sub-regions of lake ice - Multioresolution segmentation on Red, Green, Blue, PC 1, and PC 2 to segment sub-regions of lake ice	- Threshold on PC 1 to label image objects - Merge image objects of same class	- Assign - Merge
IIV	Identify Bubble Patches in different regions of lake ice classified in Level III.	- Chessboard segmentation of dark and white lake ice image objects - Multioresolution segmentation on Red, Green, Blue, PC 1, and PC 2 to segment dark and bright lake ice objects - Contrast Split segmentation Algorithm on PC 1 to split cluster of fused bubble patches into individual bubble patch	- Canny Edge Detection Algorithm on PC 1 band to label Bubble Patch edge area - Spatial relationship of image objects with Bubble Patch to remove misclassified Bubble Patch objects or re-classify any missing Bubble Patch objects. - Opening morphological filter to shape Bubble Patch - Merge image objects of same class	- Canny Edge Algorithm - Assign - Merge - Enclosed by Relationship to Neighbors: 'Border to' - Morphological Filter: Opening

2.12. References

Baatz, M. and Schäpe, A., 1999. Object-oriented and multi-scale image analysis in semantic networks. 2nd International Symposium: Operationalization of Remote Sensing, 16-20 August, ITC, NL.

Baatz, M. and Schäpe, A., 2000. Multiresolution segmentation: an optimization approach for high quality multi-scale image segmentation. *Angewandte Geographische Informationsverarbeitung XII*, 12-23.

Baatz, M., Hoffmann, C., Willhauck, G., 2008. Progressing from object-based to object-oriented image analysis. In *Blaschke, T., Lang, S., Hay, G.J., (Eds), Object-Based Image Analysis*, Springer, Berlin, pp. 29-42.

Bastviken, D., 2004. Methane emissions from lakes: Dependence of lake characteristics, two regional assessments, and a global estimate, *Global Biogeochem. Cycles*, 18(4), 1–12, doi:10.1029/2004GB002238.

Bastviken, D., Tranvik, L. J., Downing, J. A., Crill, P. M., and Enrich-Prast, A., 2011. Freshwater methane emissions offset the continental carbon sink, *Science*, 331, 50.

Bastviken, D., 2004. Methane emissions from lakes: Dependence of lake characteristics, two regional assessments, and a global estimate, *Global Biogeochem. Cy.*, 18, 1–12. doi:10.1029/2004GB002238

Benz, U.C., Hofmann, P., Willhauck, G., Lingenfelder, I., Heynen, M., 2004. Multi-resolution, object-oriented fuzzy analysis of remote sensing data for GIS-ready information. *ISPRS J. Photogramm. Remote Sens.*, 58, 239–258. doi:10.1016/j.isprsjprs.2003.10.002

Blaschke, T., 2010. Object based image analysis for remote sensing. *ISPRS J. Photogramm. Remote Sens.*, 65(1), 2-16.

Blaschke, T., Hay, G.J., Kelly, M., Lang, S., Hofmann, P., Addink, E., Queiroz Feitosa, R., van der Meer, F., van der Werff, H., van Coillie, F., Tiede, D., 2014. Geographic Object-Based Image Analysis – Towards a new paradigm. *ISPRS J. Photogramm. Remote Sens.*, 87, 180-191.

Bock, M., Xofis, P., Mitchley, J., Rossner, G., and Wissen, M., 2005. Object-oriented methods for habitat mapping at multiple scales–Case studies from Northern Germany and Wye Downs, UK. *Journal for Nature Conservation*, 13(2), 75-89.

Brosius, L. S., Walter Anthony, K. M., Grosse, G., Chanton, J. P., Farquharson, L. M., Overduin, P. P., and Meyer, H., 2012. Using the deuterium isotope composition of permafrost

meltwater to constrain thermokarst lake contributions to atmospheric CH_4 during the last deglaciation, *J. Geophys. Res.*, 117(G1), G01022. doi:10.1029/2011JG001810

Bunting, P.J., Lucas, R.M., 2006. The delineation of tree crowns in Australian mixed species forests using hyperspectral Compact Airborne Spectrographic Imager (CASI) data. *Remote Sensing of Environment*, 101, 230–248.

Canny, J., 1986. A computational approach to edge detection. IEEE Trans. Pattern Anal. Mach. Intell. 8, 679–98.

Casper, P., Maberly, S. C., Hall, G. H., and Finlay, B. J., 2000. Fluxes of methane and carbon dioxide from a small productive lake to the atmosphere, *Biogeochemistry*, 49(1), 1–19.

Chubey, M.S., Franklin, S.E., Wulder, M.A., 2006. Object-based analysis of IKONOS- 2 imagery for extraction of forest inventory parameters. *Photogrammetric Engineering & Remote Sensing*, 72 (4), 383–394.

Definiens, 2007a. Segmentation Algorithms, In *Definiens Developer 7 Reference Book*, Document Version 7.0.0.843, 15-27, Definiens AG, München, Germany.

Definiens, 2007b. Edge Extraction Canny, In *Definiens Developer 7 Reference Book*, Document Version 7.0.0.843, 62–63, Definiens AG, München, Germany.

Definiens, 2007c. Basic Concepts, In *Definiens Developer 7 User Guide*, Document Version 7.0.2.936, 27, Definiens AG, München, Germany.

Duguay, C. R. and Lafleur, P. M., 2003. Determining depth and ice thickness of shallow sub-Arctic lakes using space-borne optical and SAR data, *Int. J. Remote Sens.*, 24(3), 475–489. doi:10.1080/01431160304992

Engram, M., Walter Anthony, K. M., Meyer, F. J., and Grosse, G., 2012. Synthetic aperture radar (SAR) backscatter response from methane ebullition bubbles trapped by thermokarst lake ice, *Canadian Journal of Remote Sensing*, 38(6), 667–682.

Förster, M., Frick, A., Walentowski, H., and Kleinschmit, B., 2008. Approaches to utilising QuickBird data for the monitoring of NATURA 2000 habitats, *Community Ecology*, 9(2), 155-168.

Frohn, R.C., Autrey, B.C., Lane, C.R., Reif, M., 2011. Segmentation and object-oriented classification of wetlands in a karst Florida landscape using multi-season Landsat-7 ETM+ imagery. *Int. J. Remote Sens.*, 32, 1471–1489. doi:10.1080/01431160903559762

Glaser, P. H., Chanton, J. P., Morin, P., Rosenberry, D. O., Siegel, D. I., Ruud, O., Chasar, L. I., and Reeve, A. S., 2004. Surface deformations as indicators of deep ebullition fluxes in a large northern peatland, *Global Biogeochem. Cy.*, 18, GB1003. doi:10.1029/2003GB002069

Groom, G., Krag Petersen, I., Anderson, M. D., and Fox, A. D., 2011. Using object-based analysis of image data to count birds: mapping of Lesser Flamingos at Kamfers Dam, Northern Cape, South Africa. *International journal of remote sensing*, *32*(16), 4611-4639.

Hay, G.J., Castilla, G., Wulder, M.A., Ruiz, J.R., 2005. An automated object-based approach for the multiscale image segmentation of forest scenes. *International Journal of Applied Earth Observation and Geoinformation,* 7 (4), 339–359.

Herold, M., Scepan, J., Müller, A., and Günther, S., 2002. Object-oriented mapping and analysis of urban land use/cover using IKONOS data. In *22nd Earsel Symposium Geoinformation for European-Wide Integration*, pp. 4-6.

Jeffries, M. O., Morris, K., Weeks, W. F., and Wakabayashi, H., 1994. Structural and stratigraphic features and ERS 1 synthetic aperture radar backscatter characteristics of ice growing on shallow lakes in NW Alaska, winter 1991-1992, *J. Geophys. Res.*, 99(C11), 22459–22471.

Jeffries, M. O., Morris, K., and Kozlenko, N., 2005. Ice characteristics and remote sensing of frozen rivers and lakes, *Remote Sensing in Northern Hydrology: Geophysical Monograph Series*¸163, 63-90.

Kamal, M., and Phinn, S., 2011. Hyperspectral data for mangrove species mapping: A comparison of pixel-based and object-based approach. *Remote Sensing*, *3*(10), 2222-2242.

Keller, M. and Stallard, R. F., 1994. Methane emission by bubbling from Gatun Lake, Panama, *J. Geophys. Res.*, 99, 8307–8319. doi:10.1029/92JD02170

Kessler, M. A., Plug, L. J., and Walter Anthony, K. M., 2012. Simulating the decadal to millennial scale dynamics of morphology and sequestered carbon mobilization of two thermokarst lakes in N.W. Alaska, *J. Geophys. Res.*, 117. doi:10.1029/2011JG001796

Lackner, M. and Conway, T.M., 2008. Determining land-use information from land cover through an object-oriented classification of IKONOS imagery, *Canadian Journal of Remote Sensing*, 34 (2), 77–92. doi:10.5589/m08-016

Lang, S., 2008. Object-based image analysis for remote sensing applications: modeling reality – dealing with complexity. In: *Blaschke, T., Lang, S., Hay, G.J., (Eds), Object-Based Image Analysis*. Springer, Berlin, pp. 3-27.

Lindgren, P. R., Grosse, G., Walter Anthony, K. M., and Meyer, F. J., 2016. Detecting methane ebullition on thermokarst lake ice using high resolution optical aerial imagery. *Biogeosciences Discuss.*, 12, 7449–7490. doi: 10.5194/bg-13-27-2016

Liu, D. and Xia, F., 2010. Assessing object-based classification: Advantages and limitations, R*emote Sensing Letters*, 1(4), 187 – 194. doi: 10.1080/01431161003743173

Lu, D. and Weng, Q., 2007. A survey of image classification methods and techniques for improving classification performance, *International Journal of Remote Sensing*, 28:5, 823-870. doi: 10.1080/01431160600746456

Lu, S. L., Zou, L. J., Shen, X. H., Wu, W. Y., and Zhang, W., 2011. Multi-spectral remote sensing image enhancement method based on PCA and IHS transformations. *Journal of Zhejiang University SCIENCE A*, 12(6), 453-460.

Mather, P. and Koch, M., 2011. Computer processing of remotely-sensed images: An introduction, 4th edn, John Wiley & Sons.

Mathieu, R., Freeman, C., and Aryal, J., 2007. Mapping private gardens in urban areas using object-oriented techniques and very high-resolution satellite imagery. *Landscape and Urban Planning*, 81(3), 179-192.

Mattson, M. D. and Likens, G. E., 1990. Air pressure and methane fluxes, *Nature*, 347, 718–719.

Moskal, L. M., Styers, D. M., and Halabisky, M., 2011. Monitoring urban tree cover using object-based image analysis and public domain remotely sensed data, *Remote Sensing*, 3(10), 2243-2262. doi:10.3390/rs3102243

Novack, T., Kux, H., Feitosa, R. Q., and Costa, G. A., 2014. A knowledge-based, transferable approach for block-based urban land-use classification, *International Journal of Remote Sensing*, 35(13), 4739-4757.

de Pinho, C. M. D., Fonseca, L. M. G., Korting, T. S., De Almeida, C. M., and Kux, H. J. H., 2012. Land-cover classification of an intra-urban environment using high-resolution images and object-based image analysis, *International Journal of Remote Sensing*, 33(19), 5973-5995.

Rodarmel, C. and Shan, J., 2002. Principal component analysis for hyperspectral image classification. *Surveying and Land Information Science*, *62*(2), 115-122.

Scandella, B. P., Varadharajan, C., Hemond, H. F., Ruppel, C., and Juanes, R., 2011. A conduit dilation model of methane venting from lake sediments, *Geophys. Res. Lett.*, 38(6), 1-6. doi:10.1029/2011GL046768

Schowengerdt, A., 2007. Principal Components in Remote Sensing: Models and Methods for Image Processing, 3rd edn., Academic Press, San Diego, CA, 193–199, 2007.

Tokida, T., Miyazaki, T., and Mizoguchi, M., 2005. Ebullition of methane from peat with falling atmospheric pressure, *Geophys. Res. Lett.*, 32. L13823 doi:10.1029/2005GL022949

Varadharajan, C., 2009. Magnitude and spatio-temporal variability of methane emissions from a eutrophic freshwater lake, PhD thesis, Massachusetts Institute of Technology, Cambridge, MA.

Walter, K. M., Zimov, S. A., Chanton, J. P., Verbyla, D., and Chapin, F. S., 2006. Methane bubbling from Siberian thaw lakes as a positive feedback to climate warming, *Nature*, 443 (7107), 71–5. doi:10.1038/nature05040

Walter, K. M., Engram, M., Duguay, C. R., Jeffries, M. O., and Chapin, F. S., 2008. The potential use of Synthetic Aperture Radar for estimating methane ebullition from Arctic lakes, *J. Am. Water Resour. Assoc.*, 44(2), 305–315.

Walter Anthony, K., Vas, D. A., Brosius, L., Chapin III, F. S., and Zimov, S. A., 2010. Estimating methane emissions from northern lakes using ice- bubble surveys, *Limnol. Oceanogr.: Methods*, 8, 592–609.

Walter Anthony, K. M. and Anthony, P., 2013. Constraining spatial variability of methane ebullition seeps in thermokarst lakes using point process models, *J. Geophys. Res. Biogeosciences*, 118, 1-20. doi:10.1002/jgrg.20087

Wik, M., Crill, P. M., Bastviken, D., Danielsson, Å., and Norbäck, E., 2011. Bubbles trapped in arctic lake ice: Potential implications for methane emissions, *J. Geophys. Res.*, 116 (G3), 1–10. doi:10.1029/2011JG001761

Zhang, Y., 2002. Problems in the fusion of commercial high-resolution satellite as well as Landsat 7 images and initial solutions, *International Archives of Photogrammetry Remote Sensing and Spatial Information Sciences*, 34(4), 587-592.

Chapter 3. Detection and spatiotemporal analysis of methane ebullition on thermokarst lake ice using high-resolution optical aerial imagery[2]

3.1. Abstract

Thermokarst lakes are important emitters of methane, a potent greenhouse gas. However, accurate estimation of methane flux from thermokarst lakes is difficult due to their remoteness and observational challenges associated with the heterogeneous nature of ebullition. We used high-resolution (9–11 cm) snow-free aerial images of an interior Alaskan thermokarst lake acquired 2 and 4 days following freeze-up in 2011 and 2012, respectively, to detect and characterize methane ebullition seeps and to estimate whole-lake ebullition. Bubbles impeded by the lake ice sheet form distinct white patches as a function of bubbling when lake ice grows downward and around them, trapping the gas in the ice. Our aerial imagery thus captured a snapshot of bubbles trapped in lake ice during the ebullition events that occurred before the image acquisition. Image analysis showed that low-flux A- and B-type seeps are associated with low brightness patches and are statistically distinct from high- flux C-type and hotspot seeps associated with high brightness patches. Mean whole-lake ebullition based on optical image analysis in combination with bubble-trap flux measurements was estimated to be 174 ± 28 and 216 ± 33 mL gas m^{-2} d^{-1} for the years 2011 and 2012, respectively. A large number of seeps demonstrated spatiotemporal stability over our 2-year study period. A strong inverse exponential relationship (R^2 > = 0.79) was found between the percent of the surface area of lake ice covered with bubble patches and distance from the active thermokarst lake margin. Even though the narrow timing of optical image acquisition is a critical factor, with respect to both atmospheric pressure changes and snow/no-snow conditions during early lake freeze-up, our study shows that optical remote sensing is a powerful tool to map ebullition seeps on lake ice, to identify their relative strength of ebullition, and to assess their spatiotemporal variability.

---

[2]Lindgren, P. R., Grosse, G., Walter Anthony, K. M., Meyer, F. J., 2016. Detection and spatiotemporal analysis of methane ebullition on thermokarst lake ice using high-resolution optical aerial imagery, *Biogeosciences*, 13, 27–44. doi:10.5194/bg-13-27-2016

3.2. Introduction

Soils in the northern permafrost region contain 1300–1370 Pg organic carbon with an uncertainty range of 930–1690 Pg (Hugelius et al., 2014). A large amount of soil carbon in the Yedoma permafrost region (~ 450Pg) is found in thick Holocene deposits in thermokarst lakes and basins, undisturbed Pleistocene-age ice-rich silts known as yedoma, and Pleistocene deposits which have thawed underneath lakes and later refrozen (Grosse et al., 2011; Walter Anthony et al., 2014). However, permafrost degradation can facilitate the transfer of this permafrost-stored carbon to the atmosphere in the form of the greenhouse gases carbon dioxide (CO_2) and methane (CH_4), resulting in a positive feedback to global climate change (Zimov et al., 2006; Walter et al., 2006; Schuur et al., 2008; Koven et al., 2011). One common and effective form of permafrost degradation involves formation and growth of thermokarst lakes (Grosse et al., 2013; Kokelj and Jorgenson, 2013), which tap into deep (up to 60 m) permafrost carbon pools (Zimov et al., 1997; Walter et al., 2008).

Thermokarst lakes are a prominent landscape feature in the high northern latitudes (Smith et al., 2007; Grosse et al., 2013). They are formed in closed depressions following the thawing of ice-rich permafrost or melting of massive ice. Once initiated, the presence of a water body on permafrost serves as a positive feedback to permafrost degradation. Depending on the amount of excess ice content in permafrost, this positive feedback accelerates the growth of thermokarst lakes in both lateral and vertical directions (Jorgenson and Shur, 2007; Plug and West, 2009; Kokelj and Jorgenson, 2013). Over many years, taliks (thaw bulbs) of perennially thawed soil develop beneath thermokarst lakes (Hinzman et al., 2005; West and Plug, 2008; Rowland et al., 2011), creating conditions favorable for year-round methane production through anaerobic decomposition of organic matter by microbes (Zimov et al., 1997; Walter et al., 2006, 2008; Kessler et al., 2012). During lateral expansion, thermal erosion along the lake margin also releases both Holocene and Pleistocene organic matter from adjacent soils into anaerobic lake bot-toms, further enhancing methanogenesis (Zimov et al., 1997; Walter Anthony et al., 2014).

Ebullition (bubbling) is considered the dominant pathway of methane release from lakes to the atmosphere (Keller and Stallard, 1994; Bastviken et al., 2011). Methane produced in dense lake sediments and thaw bulbs emerges primarily through intrasedimentary bubble tubes as point-source seeps on the lake bed (Walter Anthony et al., 2010). In the high northern latitude

region, where lake surfaces freeze through- out the winter, most bubbles emerging from the lake bed ascend through the water column and get trapped by ice as gas pockets (Walter et al., 2008; Greene et al., 2014). Ongoing ice growth can separate ice-trapped bubbles from an individual seep by thin films of ice, resulting in vertically oriented bubble columns in the ice. Walter et al. (2006) took advantage of this phenomenon to reveal locations and relative strength of point sources of methane seep ebullition across lake ice. They identified four major types of methane ebullition seeps based on ice-bubble cluster morphology and they measured daily mean ebullition rates (mean ± standard error of mean) (Figure 3.1) (Walter Anthony and Anthony, 2013). It should be noted that the seep class-specific ebullition rates reported represent the daily average of thousands of flux measurements, measured on 24 pan-Arctic lakes in continuous and discontinuous permafrost regions for up to 700 days; however, bubbling within each class is highly episodic, and bubbling rates of individual seeps are not constant over time (Walter Anthony et al., 2010; Walter Anthony and Anthony, 2013): (1) A-type seeps are characterized by isolated bubbles stacked in multiple vertical layers with less than 50 % of all gas volume merged in bubble clusters. A-type seeps have the lowest ebullition rate (22 ± 4 mL gas d^{-1}); (2) B-type seeps are dominated by laterally merged bubbles stacked in multiple layers (more than 50 % of all gas volume merged in a bubble cluster). The ebullition rate of this bubble type is 211 ± 39 mL gas d^{-1}; (3) C-type seeps, associated with an ebullition rate of 1726 ± 685 mL gas d^{-1}, are characterized by single large gas pockets (usually > 40 cm in diameter) separated vertically by ice layers containing few or no bubbles; and (4) hotspot seeps have the highest ebullition rate, on average 7801 ± 764 mL gas d^{-1}. Due to upwelling of water associated with frequent bubble streams, hotspots generally appear as open water holes in lake ice following freeze-up. Usually a thin snow–ice film develops over hotspots in winter, visually masking them at the surface; however, ice blocks cut from the lake throughout winter and spring reveal that hotspot bubbling maintains a large ice-free cavity throughout winter (Greene et al., 2014).

Accounting for methane ebullition from northern thermokarst lakes can significantly improve estimates of lake contributions to regional and global atmospheric carbon budgets (Walter et al., 2007; Bastviken et al., 2011). However, due to challenges associated with the logistics of fieldwork in remote locations as well as spatial and temporal heterogeneity of ebullition, accurate estimation of methane flux from thermokarst lakes is difficult (Casper et al.,

2000; Bastviken, 2004; Wik et al., 2011). Most studies have been carried out using field measurements to understand the spatial and temporal variability of methane ebullition. However, the insufficiency of field data is a recurring issue since it is difficult to sample the entire lake area, particularly when lakes have remote locations. This may lead to an unrealistic characterization of variability of ebullition bubbles and a less accurate estimation of methane flux at a regional scale. Recently, Walter Anthony and Anthony (2013) combined point-process modeling with field-measured data to understand the drivers of ebullition spatial variability in thermokarst lakes and provided ways to reduce uncertainty in regional-scale lake ebullition estimates based on limited field data; nonetheless spatially limited field sampling remains a hindrance to whole-lake ebullition quantification.

Remote sensing methods combined with field observations can help overcome some of the limitations that exist in a sole field-survey method. One of the major advantages of remote sensing tools is that they may provide the possibility to map the entire population of methane ebullition bubbles on a lake. Moreover, remote sensing can overcome the logistical difficulties that exist in accessing methane-bubbling lakes in the remote regions of the Arctic and Subarctic. Walter et al. (2008) and Engram et al. (2012) demonstrated the potential application of synthetic aperture radar (SAR) satellite imagery to estimate whole-lake ebullition from spatially limited field measurements of ebullition along survey transects. These studies showed correlation of radar backscatter values with the percent of the surface area of lake ice covered with bubbles and field-measured methane ebullition rates based on bubble-trap measurements from lakes. Additionally, Walter Anthony et al. (2012) used aerial surveys to identify, photograph, and map large ($\sim$ 1 to $>$ 300 m^2) bubbling-induced open water holes in ice-covered lakes in Alaska associated with geologic methane seepage. Geologic methane seeps differ distinctly from ecological seeps in associated fluxes (i.e., fluxes of geologic seeps are several orders of magnitude higher than for ecological seeps) and their spatial distribution is often aligned with geological faults. Coupling aerial surveys with ground truth flux measurements and laboratory analyses, this study showed that geologic methane seepage is not extensive, but it is important in some regions of Alaska underlain by leaky hydrocarbon reservoirs.

Since open holes induced by bubbling in snow-covered lake ice are visually distinct, and since lower-flux ebullition bubble clusters trapped inside ice appear as bright white features that

have a strong contrast against dark, bubble-, and snow-free congelation ice (Figure 3.1), there is the potential and need to detect and quantify methane bubbles with optical remote sensing. In this study, we explored high-resolution optical remote sensing images to characterize methane ebullition seeps on Goldstream Lake, an interior Alaska thermokarst lake, and to study their spatiotemporal dynamics.

3.3. Study site

Goldstream Lake (64.91° N, 147.84° W; 195 m a.s.l.) is an interior Alaska thermokarst lake covering an area of approximately 10300 m^2 with maximum and average depths of 2.9 and 1.6 m, respectively. The lake formed in "yedoma-type" deposits of retransported late Quaternary loess at the toe slope of Goldstream Valley in Fairbanks (Péwé, 1975; Kanevskiy et al., 2011; Walter Anthony and Anthony, 2013). Based on remotely sensed aerial and satellite images, the lake partially drained between 1949 and 1978 but has been expanding mainly along the eastern shore since then (Figure 3.1f). This active thermokarst expansion is also indicated by spruce trees leaning lakeward along the eastern lake margin, and standing dead trees submerged in the lake offshore of the eastern margin. The vegetation around the lake is dominated by black spruce and willow. Cattail (*Typha* spp.) grows along some shallow margins of the lake. Water lilies (*Nuphar* spp.) are also found in several locations on the northern and south- western parts of the lake.

Ebullition accounts for a total of 83% of methane emission from Goldstream Lake (Greene et al., 2014). The concentration of methane in Goldstream Lake's bubbles is 82–89% (Greene et al., 2014). Ice formation on the lake usually occurs between the end of September and mid-October, reaches maximum thickness by mid-March, and ice break-up occurs around the end of April or early May. Vertically oriented layers of methane ebullition bubbles (Figure 3.1), representing point-source seeps, are widespread in the lake ice, particularly along the eastern margin (Walter Anthony and Anthony, 2013). Many hotspot seeps are also found near the eastern eroding shore and are seen as open holes in lake ice during early winter and spring.

3.4. Methods

We used three sets of data in our study: (1) high-resolution snow-free early winter lake ice images from fall 2011 and 2012, (2) high-resolution snow-covered early winter lake images from fall 2012, and (3) field-based surveys of ebullition bubble seep types and their fluxes.

We first processed the aerial images of snow-free early winter lake ice acquired in the fall of 2011 and 2012 and then mapped ebullition bubbles trapped in the ice. We refer to the bubble features seen in our snow-free images as "bubble patches" henceforth since the image resolution was not sufficient to fully resolve smaller individual bubbles (Figure 3.1). Then we characterized imaged bubble patches based on field- collected ebullition bubble seep data collected approximately 1–2 weeks after image acquisition when ice was safe to walk on in the fall of 2011 and 2012 and again in spring of the following year. We hypothesized that the brightness of bubble patches correlates with the strength of methane flux associated with four classes of ebullition bubble seeps (A, B, C, and hotspot) identified by Walter Anthony et al. (2010). We estimated from aerial photos the bubble-patch density for each seep class and the mean whole-lake seep ebullition. Finally, we examined the spatial patterns of seep locations in the lake with respect to eroding thermokarst shores, and analyzed interannual variability of seep occurrences by comparing imagery from different years.

Due to similar spectral characteristics of open water and dark lake ice, open-hole hotspots are difficult to map on snow-free lake ice images; but they are easily identifiable on snow-covered lake ice images. Therefore, we also collected high-resolution snow-covered aerial images in the fall of 2012 to map open-hole hotspots on the lake. We compared the locations of hotspots in aerial images with maps of hotspot locations determined by field measurements over multiple years to assess hotspot regularity.

3.5. Remotely sensed high-resolution image acquisition

We scheduled low-altitude, high-resolution aerial image acquisitions to map and characterize methane ebullition bubble patches (A, B, C, and ice-covered hotspots) during a narrow time window in the early winter, when first ice had formed but was still snow-free. Images were acquired in nadir with a Navion L17a plane using a Nikon D300 camera system mounted in a belly port on 14 October 2011 and 13 October 2012, 2 and 4 days following freeze-up, respectively. Flight altitude for the acquisitions was ~ 750 m a.s.l. in 2011 and ~ 587 m a.s.l. in 2012. Image scale was 1:20000 and 1:17000 for 2011 and 2012, respectively, which in turn corresponds to ground sampling distances (GSD) of 11 and 9 cm.

We collected images of the snow-covered lake in fall on 14 October 2012 using an unmanned aerial vehicle (UAV) mounted with an Aptina MT9P031 board camera to map open-

hole hotspot seep locations. The images were acquired from a flying height of approximately 230 m a.s.l., corresponding to an image scale 1:30000 and GSD of 6 cm. All the images consisted of three visible bands: red, green, and blue (RGB).

3.5.1. Ground truth field data

3.5.1.1. Fall 2011 and 2012 field surveys

We surveyed the lake perimeter and measured several permanently installed reference markers. We conducted detailed ebullition ice-bubble surveys in October 2011 2 weeks after image acquisition when lake ice was safe to walk on. The surveys were performed within two large polygons that are identified in Figure 3.1f: one about 7 m from the eastern thermokarst shore and a second near the center of the lake. The surveyed polygons in the east and center of the lake covered ~ 428 and ~ 236 m^2, respectively, and were reported in detail in Walter Anthony and Anthony (2013) and Greene et al. (2014).

In October 2012, we performed bubble surveys 6 days after image acquisition in three other polygons (total area ~ 200 m^2) randomly distributed across the lake (Figure 3.1f). We performed bubble surveys earlier after image acquisition than in 2011 to avoid white ice conditions. We used the seep identification method described by Walter Anthony et al. (2010).

3.5.1.2. Spring 2011 and 2012 field surveys

While field-based estimations of A-, B-, and C-type seeps were limited to survey plots covering about 13 % of the lake area, the locations of hotspot seeps were mapped across the whole lake using detailed DGPS surveys of open holes in October and April 2011 and 2012. Hotspots were detected visually at these times of the year as open water holes in lake ice.

3.5.1.3. Spring 2013 field surveys

In April 2013, we extracted several blocks of the full lake ice column at seep locations to investigate the temporal ebullition patterns that developed throughout the winter season.

3.5.2. Mapping ebullition seeps on lake ice

3.5.2.1. Pre-processing of images

We conducted the following image pre-processing. (1) We performed mosaicking of multiple images of Goldstream Lake to construct a complete image of the lake. This was achieved by using Agisoft PhotoScan Professional Software™ Version 0.9.0. (2) We then performed geometric image rectification with 22 DGPS-collected GCPs using a second-order polynomial transformation with bilinear resampling. The GCPs were distributed mostly around the lake perimeter. Some of them were identifiable reference points on the lake such as cattail vegetation and a LiCor methane analyzer installed on a platform on the lake. (3) For image enhancement we applied a feature linear transformation on all three visible spectral bands of the lake images using un- standardized principal component analysis (PCA). Both geometric and spectral image transformations were performed in ENVI™ image processing software, Version 4.8. PCA spectral transformation produced three independent principal component (PC) bands. The first band (PC 1 band) consisted of the variables that explained the most variance (> 98 %) in the data set attributing to bubble patches (Figure 3.2, Supplement Section S1).

3.5.2.2. Identification of bubble patches on snow-free lake ice

We applied a classification technique based on object-based image analysis (OBIA) to semi-automatically identify and map methane ebullition bubble patches in the PCA-transformed images using eCognition Developer™ 8 (Lindgren et al., 2015). Our object-based classification method comprised two steps: (1) image segmentation, i.e., aggregation of homogenous image pixels based on their spatial and spectral homogeneity into meaningful clusters known as image objects, and (2) classification of image objects (Navulur, 2007; Blaschke and Strobl, 2001). Varying ice conditions on the lake such as (a) clear, dark congelation ice, (b) milky white snow–ice, and (c) ice with shadows from neighboring trees added challenges to identifying ebullition bubble patches. We were able to resolve these challenges by integrating semantic information associated with image objects in classification (Lindgren et al., 2015). For this, the scene is first decomposed into meaningful regions that represent different areas of lakes such as vegetation and shadow, dark, and white ice. These regions are then organized in a conceptual image object hierarchy, creating a semantic network between different sized image objects – large-scale

objects in the up- per level called "super-objects", and small-scale objects in the lower level called "sub-objects" (Supplement Figure S1; Lindgren et al., 2015). For example, the lake area is a super-object composed of sub-objects associated with various lake ice characteristics (e.g., shadow, dark black ice), whereas areas of specific lake ice characteristics are super-objects of our final target feature, ebullition bubble patches. At each level, image segmentation and classification are performed to delineate and label target regions. For example in the first level, segmentation is performed on the whole lake image to identify lake shore and lake. In the second level, only the lake region is segmented and image objects derived from the lake are classified into different lake ice characteristics. The process continued as it proceeded towards lower and finer classification levels until bubble patches were identified in the lake ice in the final stage. This approach of detecting image objects from coarser to finer scale has been described as an effective way to classify images in OBIA (Blaschke et al., 2008).

More information on this hierarchical approach of bubble- patch identification can be found in the Supplement (Supplement Section S2) and in Lindgren et al. (2015).

3.5.2.3. Identification of open-hole hotspots on snow-covered lake ice

In images acquired after the first snow fall, hotspots appeared dark against the snow-covered lake. Hence, they were mapped using a simple contrast and split segmentation technique in eCognition Developer™ (Definiens, 2007). This approach involves choosing a threshold value on the RGB image bands for the algorithm to maximize the contrast between hotspots and snow-covered lake pixels that separates the image content into dark objects (consisting of pixels below the threshold, i.e., hotspots) and bright objects (consisting of pixels above the threshold, i.e., snow-covered lake ice).

3.5.3. Statistical analysis

3.5.3.1. Interpretation of image data results

We extracted PC 1 gray values of individual ebullition bubble patches mapped in images from the year 2011 and 2012. PC 1 values of the image ranged between 0 and 255. Bubble patches are visually bright in true-color composite (RGB composite) images but appeared darker (i.e., low PC 1 values) than the surrounding lake ice in the PC 1 band (Supplement Figure S2). Therefore, we inverted PC 1 values of bubble patches to make it visually intuitive, i.e., bubbles that

apappeared bright in natural color composite also appeared bright in the PC 1 band (Fig. 2). Henceforth, we refer to this brightness obtained in the inverted PC 1 as "PC 1 brightness".

We assessed the relationship of ebullition bubble-patch PC 1 brightness values with four distinct types of ebullition seeps that we identified during our field surveys. We performed an analysis of variance (ANOVA) to test the null hypothesis that the mean PC 1 values (and thus true bubble brightnesses via its inverse relationship with the PC 1) of four types of seeps are not significantly different. We applied a post-hoc Tukey's honest significant difference (HSD) test, in case the null hypothesis was rejected, to identify significantly distinct seeps. Results of this analysis are shown in Sect. 4.1.

3.5.3.2. Classification of bubble patches

We applied a supervised classification using a maximum-likelihood classifier (MLC) on the three original visible bands and the extracted PC 1 band to classify mapped bubble patches into four distinct seep classes. The MLC calculates a Bayesian probability function from the input training classes and then assigns each pixel in the image to the class of highest membership probability (Mather, 2009). We collected 98 random samples, 35 for training and 63 for validation, on the 2011 image and similarly 181 random samples, 50 for training and 131 for validation, on the 2012 image. The samples were located at seep locations identified using field-collected DGPS data points.

The MLC approach categorized bubble patches solely based on the pixel spectral characteristics, i.e., only using the brightness values of the training samples. Since the size of bubble patches is also an additional important indicator of seep class and methane flux (Walter Anthony et al., 2010), in a subsequent step, we further refined our classification results by integrating size as an additional feature to more accurately assign bubble patches with a seep type (Supplement Sectio S3, Table S1). Finally, we estimated the seep density and mean whole-lake ebullition rate by assigning the mean long-term flux values for seep types provided by Walter Anthony and Anthony (2013) to our classified bubble patches.

3.5.3.3. Analysis of spatial distribution of bubble patches

We studied the spatial distribution of ebullition bubble patches as a function of distance from the eroding eastern thermokarst shore. For this, we divided the lake area into multiple 5 m wide

zones starting from the eastern eroding margin as mapped in a 1949 aerial image (Figure 3.1). Lake zones were created on both sides of the 1949 lake margin to cover the present-day lake area. We calculated the percent of lake ice area covered with ebullition bubble patches for each zone and then analyzed its relationship to the distance from the eastern shore lines of the lake observed in 1949, 1978, and 2012.

3.5.3.4. Analysis of temporal pattern of bubble patches

We evaluated the multi-temporal (year 2011 and 2012) variability of ebullition bubble patches and assessed their regularities in space and time. We utilized a marked point-process model to analyze spatial seep patterns in our multi-year bubble-patch data set derived from the images. Point-process modeling was performed on a set of bubble-patch centroids with their respective location and year information, which served as a marked point data set for the model, to derive and test the spatial characteristics of bubble-patch distribution against a null hypothesis based on complete spatial randomness. The null hypothesis suggests that the bubble patches are the results of a spatially random process over the study area and thus the difference of spatial patterns between years is random, i.e., the locations of bubble patches are independent when comparing between years (Bivand et al., 2008). For this, we generated a multi-type nearest-neighbor distance function derived from the locations of the bubbles mapped in the images using Gcross from the spatstat statistical package in R (Baddeley and Turner, 2005). Gcross first determines clustering parameters for the data set in the first year. These clustering parameters are then used to model the expected number of the second-year point given a certain distance from the first-year points if the second-year point placement is random relative to the first-year point placement. Based on the deviation between observed empirical value and expected theoretical value estimated by the model, we determined the stability of seep locations between 2011 and 2012. Similarly, we performed the multi-type nearest-neighbor distance function analysis using Gcross on the field data set of hotspot locations collected in year 2011 and 2012 to check regularity of hotspots.

We also considered that the centroid of a bubble patch, representing an ebullition bubble-patch point location, could move from one year to another due to changes in the shape and size of a bubble patch or changes in bubble-tube configuration in the sediment. We compared the overlap area between ebullition patches mapped in 2011 and 2012 images. If some area of a

2011 bubble patch appeared within the area of a 2012 bubble patch or vice versa, then we considered the bubble patch to be stable in location (i.e., reappearing). We assumed that the overlapping bubble patches originated from the same point-source seep. We checked location stability among four classes of overlapping patches that were defined by setting thresholds on area overlap: "all overlap- ping bubble patches", "more than 25% area overlap", "more than 50% area overlap", and "more than 75% area overlap".

We used a map of open-hole hotspot seeps derived from UAV images to compare the frequency of hotspots with hotspot occurrences observed during multiple years of fieldwork by Greene et al. (2014).

3.6. Results and discussion

3.6.1. Relationship between bubble-patch brightness and field-measured methane flux

We found that PC 1 brightness values of bubble patches correlated with the strength of field-measured methane flux of ebullition seeps (A, B, C and hotspot seeps). The lowest mean PC 1 brightness belonged to A-type seeps followed by B-type seeps in both 2011 and 2012 (Figure 3.3). The highest mean PC 1 brightness was demonstrated by hotspots in 2011 but C-type seeps had slightly higher mean brightness in 2012 (Figure 3.3). Our ANOVA test rejected the null hypothesis that the mean PC 1 values of the different seep types are the same suggesting significant distinctions between mean PC 1 brightness values of different seep classes. Further post-hoc analysis using Tukey's HSD test demonstrated that C- and A- type, hotspot and A-type, and hotspot and B-type seeps are significantly distinct based on their mean PC 1 with p values < 0.05 (Supplement Table S2). We thus conclude that higher-flux seeps (hotspot and C-type) are associated with brighter bubble patches, and lower-flux seeps (A- and B- type) are associated with darker bubble patches.

An absolute discrimination of individual seep type based on brightness was not supported by the post-hoc tests due to overlapping brightness ranges between different seep types (Figure 3.3). This is likely because ebullition is episodic with varying bubbling rates over time and because individual low-flux methane seeps were not resolved given the spatial resolution of the image. A possible explanation for low PC 1 brightness of some hotspots is that fresh thin nighttime ice temporarily covered some hotspots on the image acquisition day, allowing the formation of few

small white gas bubbles, while much of the remaining gas escaped through cracks in the thin ice, resulting in low true brightness for these high-flux seeps. We have observed this phenomenon on several occasions during our field visits in early winter and spring, particularly on days when temperatures stayed low and hotspots were covered with a few millimeters of ice with small bubbles beneath (Figure 3.4); these hotspots usually open up when atmospheric temperature rises again during the day. Conversely, hotspots that remained open could not be identified in our snow-free lake ice imagery due to spectral similarities between open water and clear black ice (Figure 3.1). ANOVA analysis was only performed on ice-covered hotspots.

We found that a large number of A-type seeps clustered together were not mapped as individual bubble patches but rather as a single large bubble patch. A-type seeps and high-flux seeps that were close together were also mapped in a single feature associated with a brighter bubble patch. Therefore, some A-type seeps showed high PC 1 brightness values. Similar to A-type seeps, occasionally individual B-type seeps were also not distinct. In a time series analysis of bubbling frequency by A- and B-type seeps, Walter Anthony et al. (2010) showed that bubbling from these shallow-sourced seeps is highly seasonal. Bubbling rates are high in summer when surface sediments are warmer, and low in winter when sediments cool down. Bubble traps left in place over these seep types year round revealed that low-flux seeps can have periods of no bubbling for up to several months. Ice blocks harvested by us in spring over seeps marked as A-type seeps in October confirm this pattern (Supplement Figure S3). It is very likely that A- and B-type seep conduits were present in the sediments, but not actively bubbling during the 2- and 4-day periods after ice formation captured by the 2011 and 2012 imagery. Thus they did not appear under the given spatial resolution of the image and its specific acquisition time. Also, bubble traps placed over C-type seeps year round revealed that these seeps can also undergo long periods (weeks to months) of no bubbling, but when they bubble, the bub- bling rates are usually very high (Walter Anthony et al., 2010). This intermittent flux behavior probably contributed to some discrepancies in the relationship between bubble-patch brightness derived from images that captured a snapshot of ebullition activity and methane flux values of seeps estimated from long-term field observations (Table 3.1).

In other parts of Goldstream Lake, especially along the eastern shore, we found large patches of many individual ebullition bubbles (each typically 3 to 10 mm diameter) that formed

large diffuse patches rather than clustering as tightly packed bubbles the way A, B, C, and hotspot seeps do. In our optical images, these ebullition bubbles appeared as irregular patches of fuzzy, white-colored bright ice with some bright regular bubble spots (Figure 3.4). Therefore, the brightness values corresponding to the surrounding diffuse patches were assigned to other seeps, particularly to low-flux seeps that were within the patch and had not expressed completely when the images were acquired. Until recently, these millimeter-scale ebullition bubbles were only recorded in transect-survey data as "tiny-type" seeps but never assigned a mean daily flux value or included in whole-lake ebullition estimates due to a lack of associated flux field measurements. Recent flux measurements made continuously year round with submerged bubble traps on the tiny-type seep class in Goldstream Lake and other lakes suggest that fluxes from these seeps may also be important (Walter Anthony et al., unpublished). Analysis of bubbles collected with bubble traps placed over tiny-type seeps revealed that these bubbles were 60–80% methane in volume (Walter Anthony et al., unpublished). When we extracted an ice block in spring 2013, we observed that tiny-type ebullition had been frequent throughout winter, resulting in long, vertically oriented stacks of tiny ebullition bubbles trapped in ice (Figure 3.4).

3.6.2. Classification of bubble patches

The overall MLC classification accuracy for differentiating seep types was ~ 50% for both 2011 and 2012 (Supplement Table S3). The classifier performed better to identify the lowest flux seeps (A-type) and the highest flux seeps (hotspot-type). B-type and C-type seeps showed high error of commission, mostly arising from the misidentification of A-type seeps and hotspots. C-type seeps had the largest error of omission since they were mostly misclassified as B-type seeps in 2011 and hotspots in 2012.

Generally higher densities of A-type seeps (and also slightly in B- and C-type seeps) in ground surveys (Walter Anthony and Anthony, 2013; Greene et al., 2014) compared to aerial images (Table 3.1) can be explained by the time in which observations were made and image resolution. Results reported in Walter Anthony and Anthony (2013) and Greene et al. (2014) are based on ground surveys conducted over multiple years (2007–2011) at Goldstream Lake usually 1 to 2 weeks following freeze-up when ice was safe to walk on (Walter Anthony et al., 2010). Since our aerial surveys were conducted only 2–4 days after ice formation, and the frequency of bubbling events from A-type seeps is often weeks to months in winter, it is not surprising that the

field surveys several weeks after ice formation capture an order of magnitude more A-type seep bubbles. Additionally, it is very likely that some active A-type seeps that occurred in very small patches were not distinct under the given resolution of the aerial images. Relatively more frequent bubbling in B- and C-type seeps allows for similar seep density values between ground surveys and aerial images; however, as expected, the 2012 seep densities are closer to the ground-ice survey values due to (a) more time since freeze-up and (b) a much higher barometric pressure drop preceding the aerial image acquisition in October 2012 compared to October 2011. It is well established that ebullition dynamics are related to changes in barometric pressure (Mattson and Likens, 1990; Fechner-Levy and Hemond, 1996; Scandella et al., 2011).

The comparison of hotspot densities in optical images vs. ground surveys in Table 3.1 also shows the expected pattern. The ground-survey data of hotspots reflect multiple years of surveys of whole-lake hotspots when ice is thick enough to safely walk on. When ice is very thin a few days after freeze-up, more open holes are present on the lake and classified as hotspot seeps in aerial images. A week or more later, many holes freeze over and will be classified as C-type seeps in ground surveys. This could have also led to a high classification error for C-type seeps. The total density of C-type and hotspot seeps combined remains consistent (~ 0.04 seeps m^{-2}) in both aerial and ground observations (Table 3.1). This also indicates that some of the seeps identified as hotspots several days after freeze-up in aerial photos really become what we classify as C-type seeps (ice-sealed at the surface) within a week or more following freeze-up.

3.6.3. Estimation of whole-lake methane flux

Our image-based analysis shows the whole-lake flux to be 174 ± 28 and 216 ± 33 mL gas m^{-2} d^{-1} for the year 2011 and 2012, respectively. The uncertainty terms are based on the standard error of the means of field-measured fluxes for seep classes. The higher-flux estimate in 2012 is due to the presence of a large number of bubble patches in 2012 (0.185 seeps m^{-2}) compared to 2011 (0.119 seeps m^{-2}) (Table 3.1). The field-based estimate of whole-lake ebullition for Goldstream Lake using ice-bubble transect surveys (170 ± 54 mL gas m^{-2} d^{-1}), was slightly at the low end of the estimates based on optical imagery analysis from 2011 and 2012 respectively. It is conceivable that the field-based transect surveys might yield a lower flux than whole-lake seep analyses given that seeps are spatially rare, and field surveys often cover < 1 % of the lake surface area (Walter Anthony and Anthony, 2013). However, on Goldstream Lake, where our

field transect bubble surveys covered 13 % of the lake area for A, B, and C-type seeps and 100% of the lake area for hotspots, the higher estimates based on optical imagery appear to be due to an overestimation of hotspots in the early-acquisition date aerial image analysis. It is important to note that while the whole-lake methane flux estimates from our aerial survey are close to those based on ground surveys, the flux estimates for individual seep types may vary between the methods. It is also possible that with aerial surveys we are underestimating the total contribution of methane flux from low-flux seeps because they had not expressed completely when we acquired our aerial photos and that we are overestimating the contribution from high-flux seeps.

3.6.4. Spatial distribution of bubble patches in relation to the thermokarst lake margin

High methane production in response to thermokarst activity on the Goldstream Lake is evident from the distribution pattern of ebullition bubble patches at the eroding margins in different years. We found a strong inverse relationship (R^2 values of 0.86 and 0.79 for the years 2011 and 2012, respectively, with p values < 0.05) between the ebullition bubble patch area covering the lake ice and the distance from the rapidly eroding eastern margin of the lake (Figure 3.5). The percent surface area of lake ice covered with ebullition bubble patches ice decreased with distance from the active erosion margin. Thermo-erosion as well as talik growth on the expanding eastern shore releases labile Pleistocene-aged organic matter as permafrost thaws, enhancing anaerobic microbial activity in the lake and talik sediments, and leading to enhanced methane emissions along this shore (Brosius et al., 2012; Walter Anthony and Anthony, 2013). Holocene-aged carbon from vegetation and active layer soils is also eroded and additionally produced within the lake, further fueling microbial methane production (Walter Anthony et al., 2014). Walter Anthony and Anthony (2013) found an interesting relationship between lake bed morphology and ebullition bubble seep density on Goldstream Lake. They found dense clusters of ebullition seeps distributed ~ 10 m apart across the lake that matched the spacing of baydjarkah on the lake bed. This indicates that most of the methane gas bubbles originated from the top of baydjarakhs, consisting of organic-rich thawed permafrost soil. While we did not conduct specific analyses in our study, such patterns should be detectable in optical remote sensing images of lake ice as well.

We observed fewer ebullition bubble patches in the center of the lake, which we interpret as a sign that labile Pleistocene-aged organic carbon in the talik under this area has been largely

depleted, and unlike at the edge along the active erosion margin, there is no significant additional accumulation of ancient labile carbon in the lake center (Brosius et al., 2012). Radiocarbon dating of bubble patches found in the lake center showed that these seeps originate from Holocene-aged and more recent organic matter that is found in the upper lake sediments (Brosius et al., 2012). Generally, methane bubbling was the lowest along the 1949 eastern lake margin and the highest along the 2012 eastern lake margin (Figure 3.5), indicating that depletion of labile carbon progressed since these areas were included in the lake, and the active thermo-erosion margin migrated eastward. This shows that optical remote sensing is a powerful tool to understand the spatial variability of methane ebullition on thermokarst lakes.

3.6.5. Multi-year comparison of bubble patch characteristics: 2011 and 2012

We observed four possible characteristics of bubble patch dynamics in our images (Figure 3.6). (i) Bubble patches may move horizontally; (ii) bubble patches do not maintain the same morphology between years (e.g., single bubble patches re-appear in a cluster of multiple patches the next year or vice-versa); (iii) bubble patches appear in an image in one year and not another; and (iv) bubble patches maintain the location and shape but patch size is different between the years. It is important to note that these observations are made during the two very short windows of time 2–4 days after freeze-up. Our analysis does not take into account the changes in long-term bubble patch morphology. Hence, it is important to highlight that the characteristics of bubble patches are driven by the dynamics of bubble formation and transport, hydrostatic pressure, and ice growth. Other changes in the characteristics of bubble patches could be because of evolution of point sources or changes in point-source conduits (bubble tubes) in the sediment (Walter et al., 2008; Scandella et al., 2011). Atmospheric pressure dynamics can also strongly impact bubbling over short timescales, resulting in different ice-bubble patterns one year from the next if insufficient time passes to allow all seeps to be expressed in the lake ice cover. Field measurements have shown that ebullition is inversely related to changes in hydrostatic pressure (Mattson and Likens, 1990; Varadharajan, 2009; Casper et al., 2000; Glaser et al., 2004; Tokida et al., 2005; Scandella et al., 2011). A significant air pressure drop during the week preceding image acquisition in October 2012 may have allowed methane that previously accumulated in the sediment during high-pressure days to rise up into the water column, manifesting itself as larger numbers of bubbles (Figure 3.7), and larger and brighter bubble patches in the lake ice

(Figure 3.6). Conversely, air pressure change in October 2011 was not large enough to enhance ebullition before the image was acquired. As a result, bubble patch density was 55% higher in 2012 (0.185 m^{-2}) compared to 2011 (0.119 m^{-2}). Similarly, the estimated mean whole-lake ebullition was 24% higher in 2012 compared to 2011 due to different atmospheric pressure dynamics. However, the general spatial distribution of bubble patches remained the same between the two years: ebullition bubble patches were more concentrated towards the eastern thermokarst lake shore.

We rejected the null hypothesis of complete spatial randomness to show that the difference in spatial patterns of bubble patches and hotspots between years is not random, i.e., that the locations of seeps in the years 2011 and 2012 are not independent. The Gcross distribution function showed that a statistically significant number of second-year bubble patch center points are less than 2 m away from the first-year center points and that there are far fewer than expected that are 3 m or more apart (Figure 3.8a). For the hotspots, a statistically significant number of seeps moved less than a meter (Figure 3.8b). Since our image rectification accounted for a geolocation error of less than 20 cm and DGPS geolocation error is even smaller and considered negligible, we conclude that the seep locations are consistent between years 2011 and 2012.

Based on our DGPS data, the number of hotspots was relatively stable among the various surveys with about 105 hotspots for the whole lake as the average of various measurements during different years and spring and fall field seasons (Greene et al., 2014). UAV-based aerial images taken 5 days after ice formation when snow covered the lake also demonstrated close agreement with the hotspot seep numbers and locations. We were able to identify 78 dark open water holes in the white, snow-covered UAV lake image acquired in early winter of 2012. Among these 78 locations there was a total of about 95–100 active open-hole hotspot seeps since some large, irregularly shaped holes consisted of multiple, coalesced holes produced by hotspot seeps of close proximity (Supplement Figure S4).

When we compared the location of bubble patches in 2011 and 2012, we found that 47.2% of a total of 1195 ebullition bubble patches mapped in 2011 reappeared in 2012, which is 35.7% of a total of 1860 ebullition bubble patches mapped in 2012. We found that 37.5, 30, and 17.7% of bubble patches mapped in 2011 reappeared in 2012 with an overlap area of "more than 25%", "more than 50%", and "more than 75% area", respectively. We expect that if more time passed

between the time of freeze-up and aerial image acquisition date we would see an even higher percentage of seep location re-occurrences because more seeps would be actively expressed.

We also observed a relationship between bubble-patch brightness and location stability of bubble patches. Very bright patches in 2012 seemed to appear at locations where bubble patches were already observed in 2011. This could indicate locations of high-flux seeps where methane was able to rise through the sediment even under relatively high hydrostatic pressure conditions that we observed in October 2011. Based on our bubble patch classification results (Table 3.1), we also noticed that seep density of high-flux C- and hotspot-type seeps is less variable during our study period compared to low-flux A- and B-type seeps. However, long-term remote sensing and ground-based observations are required to further test our hypothesis of seep regularity that high-flux seeps are temporally more stable in their location than low-flux seeps. Additionally, long-term data may also help to account for the difference in pressure and look at possible changes in seep type over the years.

The regularity of bubble patches observed despite the differences in atmospheric pressure conditions following the lake freeze-up events in 2011 and 2012 as well as the location stability of hotspots indicates that a large number of point-source seeps in thermokarst lakes are stable over at least annual timescales. Walter Anthony et al. (2010) also found seeps to maintain stable locations in Goldstream Lake when submerged bubble traps were placed over individual seeps to monitor their ebullition dynamics for periods of up to 700 days. In Siberia one hotspot seep location was marked and found stable for at least 8 years (Walter Anthony et al., 2010).

3.7. Benefits and challenges of aerial image analysis for ebullition seep mapping

We found numerous significant benefits of using aerial images for characterizing ebullition seeps on lake ice. Aerial images of early winter lake ice without snow cover allowed us to map and characterize bubble patches on the entire lake surface as well as assess their spatial distribution more accurately. Snow-covered lake ice images allowed us to map open-hole hotspots. We were able to differentiate high-methane-emitting seeps from low-methane-emitting seeps on the lake based on PC 1 brightness values of bubble patches. Image-derived estimates of seep densities by class agreed with those of field-based survey methods, except for some overestimation of hotspots and underestimation of A-type seeps. We were able to differentiate lake areas with high

seep densities versus low seep densities; having this ability is especially useful for quantifying methane ebullition on larger lakes that are harder to survey extensively by foot.

Our results also imply a potential to apply high-resolution optical images at a regional scale to quantify relative methane flux from many lakes, which at a minimum should allow for the classification of high-ebullition versus low-ebullition lakes and their distribution in a region. It is important to note that while image analysis is useful to comprehensive mapping of lake ice bubbles, for the estimation of whole-lake methane emissions, this technique should be coupled with bubble-trap field measurements and laboratory measurements of methane concentration in bubbles.

But because ebullition is a temporally dynamic phenomenon, our ability to accurately identify the distinct seep type of bubble patches on a snapshot of ebullition activity during only 2 and 4 days since lake ice formation is limited. The morphology and distribution of bubbles can undergo significant changes in response to freeze/thaw cycles during winter (Jeffries et al., 2005). Furthermore, ebullition is highly controlled by the balance between atmospheric pressure and sediment strength, making it an episodic phenomenon (Varadharajan, 2009; Scandella et al., 2011). Ebullition is triggered following the fall of hydrostatic pressure or after a sufficient volume of gas is produced in the sediment that allows bubble tubes or gas conduits in lake sediments to open or dilate (Scandella et al., 2011). Bubbles previously trapped in lake sediment then break out through these open bubble tubes and rise up in the water column. Moreover, microbial activity of methane-producing bacteria is temperature-dependent. As a result, seep ebullition slows down when the lake surface sediments cool down in winter and it increases as lake sediment warms up in summer (Walter Anthony and Anthony, 2013). Therefore, discrepancies arise in estimates of the number of seeps and seep morphology derived from observations made at different times of the ice cover season (Wik et al., 2011). Ideally, optical image acquisition would occur at least several weeks following freeze-up of lakes to allow more time for seep expression in lake ice. Unfortunately, snow-free conditions several weeks after freeze-up are rare in many regions of the Arctic; and early snow cover inhibits the mapping of bubble patches with optical data.

SAR data have an advantage over optical remote sensing data in detecting methane bubbles trapped in lake ice under snow cover conditions (Walter et al., 2008; Engram et al., 2012).

Engram et al. (2012) showed that particularly L-band SAR data acquired in the fall have the potential to estimate whole-lake methane ebullition since a longer-wavelength L-band is able to detect bubbles under other conditions such as the presence of snow, a thin layer of white ice, and aquatic vegetation. However, the moderate spatial resolution of current L-band SAR systems can be a limiting factor to estimate methane emission from small lakes and to capture delicate spatial patterns of ebullition seeps on lakes. SAR lake images further tend to have false backscatter signals from the lake shore (Walter et al., 2008; Engram et al., 2012), therefore limiting its usability in proximity to shores (about 1 pixel around lake shores is excluded in SAR analyses) where we showed an important component of ebullition may take place on eroding thermokarst margins. Thus, high-resolution optical images can supplement SAR-based studies by revealing the location of methane ebullition seeps and their types on the lake more precisely. Our study shows that optical high-resolution remote sensing methods have the potential, given the caveats raised above, to improve understanding of spatial and temporal variability of ebullition and therefore the dynamics of microbial processing of organic matter within an individual lake.

3.8. Conclusions

It is important to understand the dynamics of methane ebullition from thermokarst lakes to estimate the amount of carbon release from thawing permafrost and to evaluate its feedback to the global carbon cycle. Our study focusing on Goldstream Lake, Interior Alaska, shows that high-resolution optical remote sensing is a promising tool to map the distribution of point-source methane ebullition seeps across an entire thermokarst lake surface, a task that is difficult to achieve through field-based surveys alone. This method helps to reveal the location and relative sizes of high- and low-flux seepage zones within lakes. We also demonstrated that a large proportion of ebullition seeps in the study lake were location-stable over at least two winter seasons in the 2011–2012 observation period. Such observations may be used to indirectly characterize permafrost carbon mobilization in a lake since lake portions with greater numbers of high-flux seeps likely indicate either the presence of rapidly thawing organic-rich permafrost deposits or eroding lake margins. Our approach is also applicable to other regions and will help to characterize methane ebullition emissions from seasonally ice-covered lakes, including thermokarst and non-thermokarst lakes in tundra and boreal zones. It will help to differentiate lakes in a region based on methane emission by estimating ebullition seep density, and their

relative methane flux. This differentiation could potentially be used to identify presence or absence of organic-rich permafrost deposits such as yedoma in the area. For example, yedoma-type thermokarst lakes, such as Goldstream Lake, where large amounts of labile carbon are readily available for microbes to decompose, emit more methane than non-yedoma-type thermokarst lakes. This can be a useful supplement to surveying soil carbon pools and yedoma distribution at a regional scale. Multi-temporal spatial information derived from remotely sensed optical data allows the identification of variables that control methane ebullition dynamics and spatial patterns. However, the timing of optical image acquisitions is a critical and a potentially limiting factor, with respect to both atmospheric pressure changes and snow/no-snow conditions during early lake freeze-up. Therefore, high-resolution remotely sensed optical images in combination with SAR and field data could be a very valuable tool to improve the estimation of methane emission from lakes at the regional scale.

3.9. Acknowledgements.

We thank A. Bondurant for harvesting ice blocks; P. Anthony for statistical coding; and A. Strohm, M. Engram, and J. Lenz for assistance with other fieldwork. We thank J. Cherry for aerial image acquisitions and B. Crevensten and G. Walker for UAV image acquisitions. We thank the editor I. Laurion and other reviewers for their valuable feedback. This research was funded by NASA Carbon Cycle Science, grant no. NNX11AH20G. Additional support came from NSF no. 1107892.

3.10. Figures

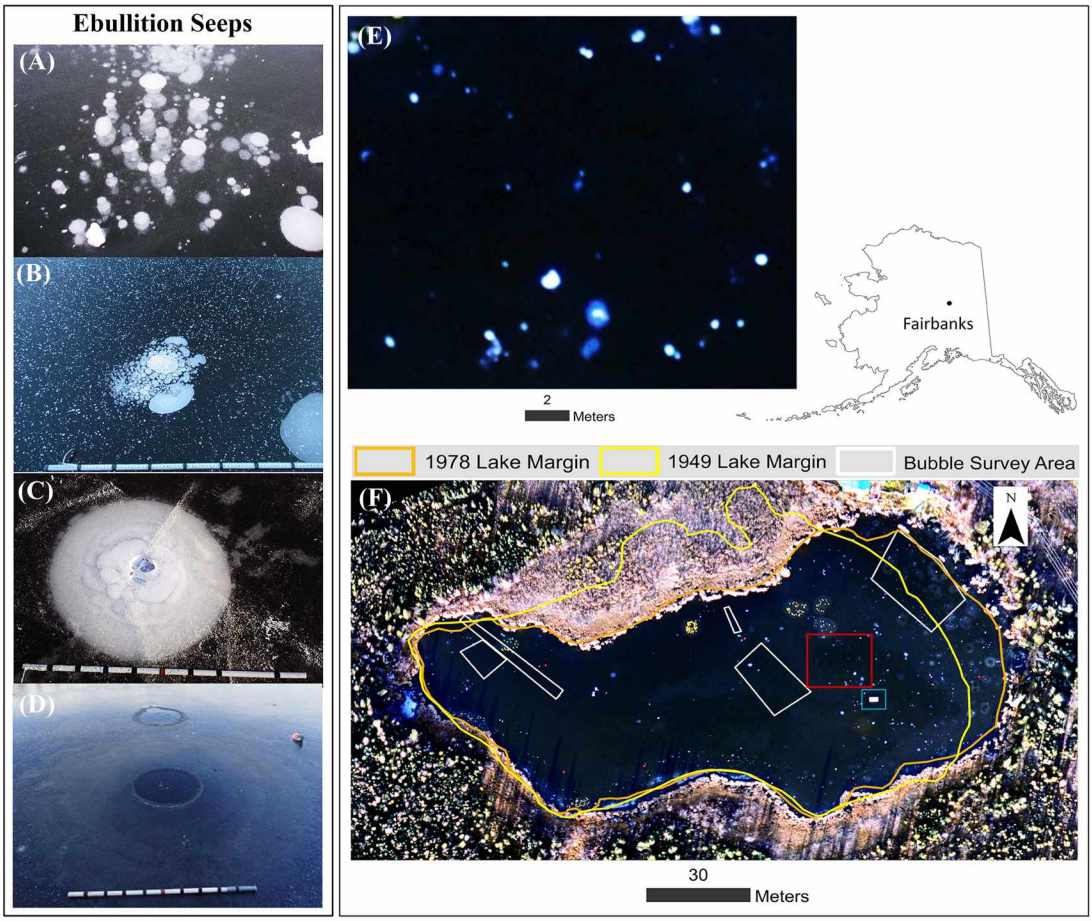

Figure 3.1. Photos showing four distinct patterns of point source ebullition seeps in early winter lake ice: **(a)** A-type; **(b)** B-type; **(c)** C-type; **(d)** Hotspot. The white speckles on the background lake ice surface in **b** are snow/hoar ice crystals, not bubbles; **(e)** a close-up (red box in the lake image shown in panel **f**) shows the appearance of ebullition bubble patches as bright white spots on the aerial image (natural color composite of red, green and blue bands) of Goldstream Lake (64.91°N, 147.84°W), Fairbanks, Alaska acquired on 14 October 2011. A rectangular wooden instrument platform (highlighted in blue box) also appears bright.

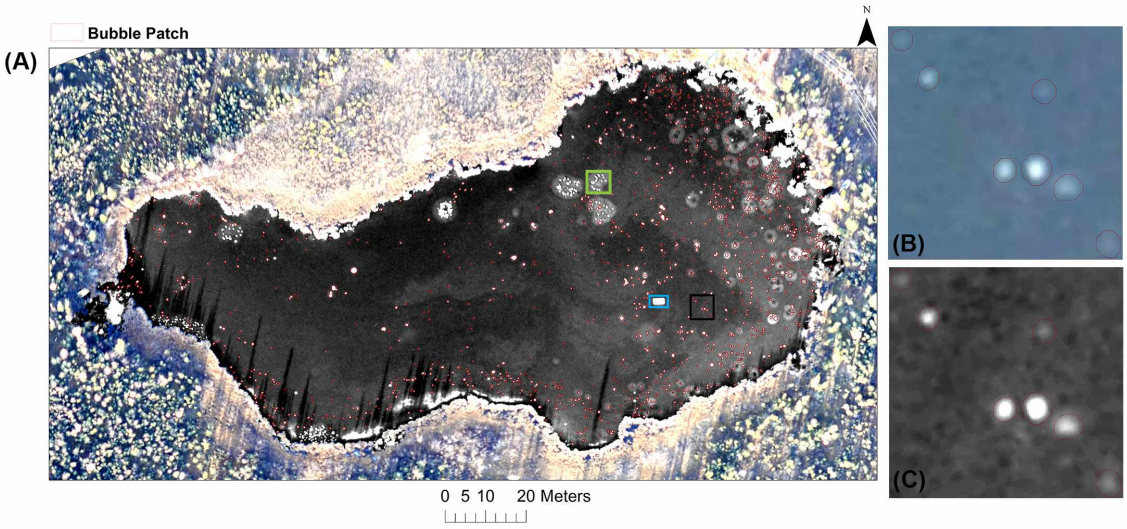

Figure 3.2. (a) 2011 bubble patch map of Goldstream Lake overlaid on Principal Component 1 image (PC 1, inverted). The land around the lake is shown in a true color composite of red, green and blue bands (RGB); **(b)** and **(c)** show the area highlighted in the black box in panel **a** overlaid on RGB composite and PC 1 respectively. Bright bubble patches appear distinct against dark lake ice on PC 1. A rectangular wooden instrument platform in the center of the lake (blue box) as well as clusters of lily pads (one example highlighted in green box) on the northern and south-western parts of the lake (see Fig. 3.1) also appear bright on PC 1.

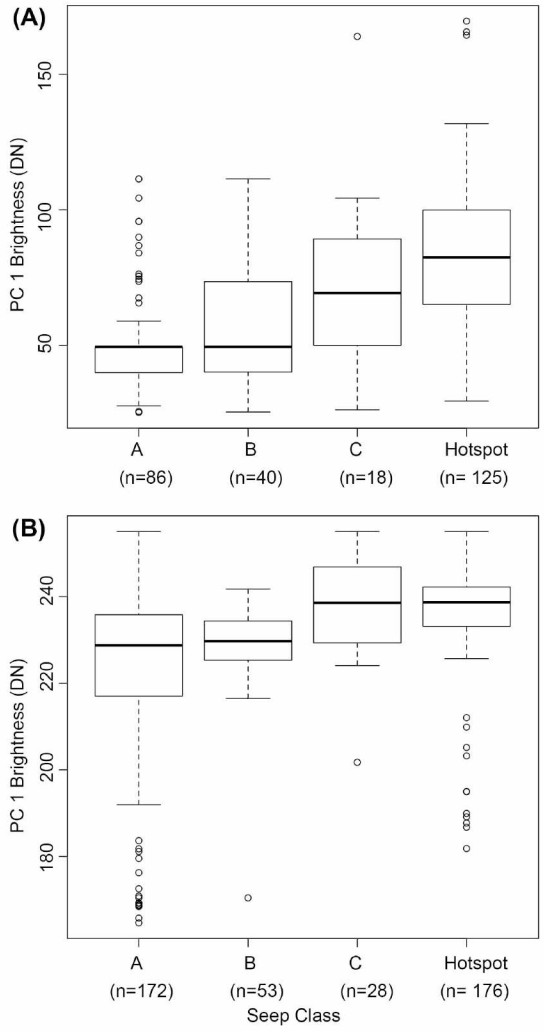

	PC 1 Brightness			
	Year 2011		Year 2012	
Seep Class	Mean	Std. Dev	Mean	Std. Dev
A-type	51.86	18.92	222.34	20.83
B-type	58.29	23.83	228.76	10.04
C-type	72.14	32.51	237.71	11.58
Hotspot	84.59	28.03	235.86	12.57

Figure 3.3. Box plots of PC 1 brightness values for bubble patches with different classes of seeps in 2011 **(a)** and 2012 **(b)**. Significant differences (p-values < 0.05) based on their PC 1 mean brightness values were found between C- and A- type seeps, Hotspot and A-type seeps, and Hotspot and B-type seeps for 2011; and C- and A- type seeps, Hotspot and A-type seeps for 2012.

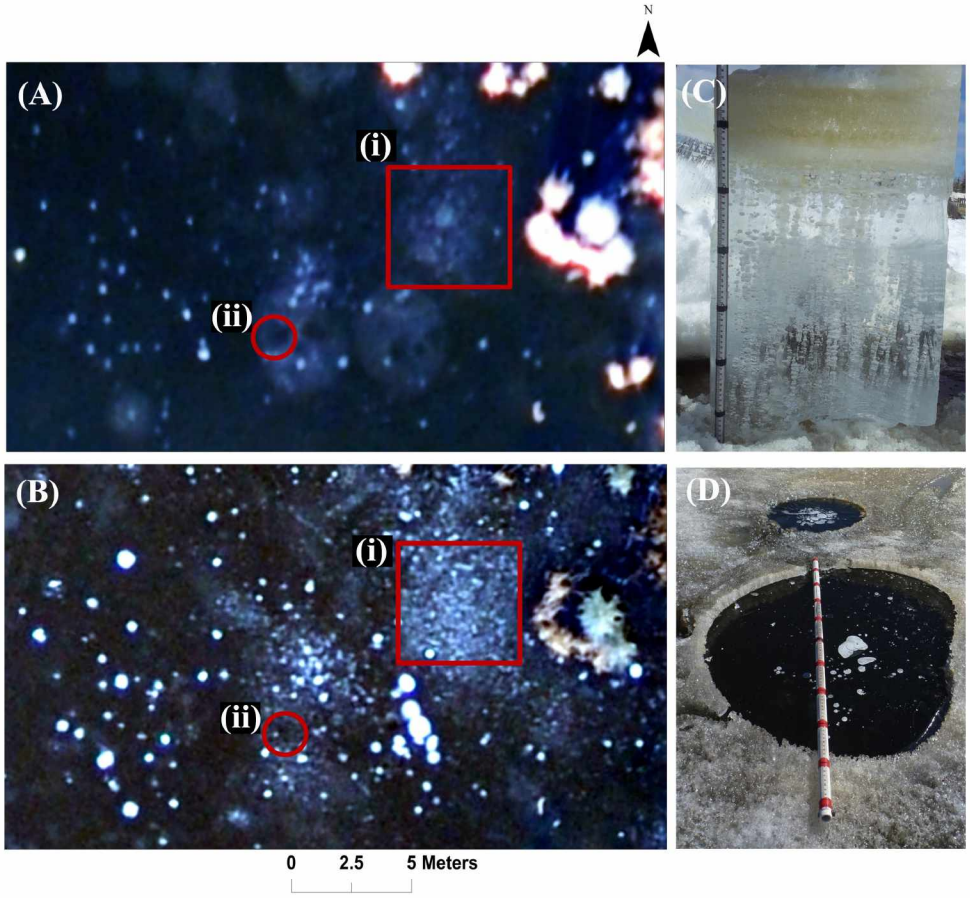

Figure 3.4. (a-b) Close-up of low-altitude aerial images from Goldstream Lake (~10-15 m from the eastern thermokarst margin), Fairbanks, Alaska [the same aerial extent shown in **(a)** – October 2011; **(b)** – October 2012]. The red box (i) highlights a densely packed cluster of mm-scale ebullition bubbles (Tiny-type seep) in both years. A few B or C-type seeps also occurred among the Tiny-type ebullition bubbles inside the area marked by the red square. The red circle (ii) shows an area of Hotspots. In 2011, the Hotspots appear dark similar to clear black ice surrounded by a bright circular patch, likely hoar frost formed around open water holes; **(c)** An ice block cross-section with the Tiny-type seep bubbles in the bubble cluster area shown in area (i); **(d)** In April 2012, the Hotspot highlighted in area (ii) seems to be mostly covered with a very thin layer of fresh black ice with a few bubbles trapped beneath; however there was a mostly ice-free cavity in the ice above the Hotspots locations while the rest of the lake ice was still ~ 50 cm thick.

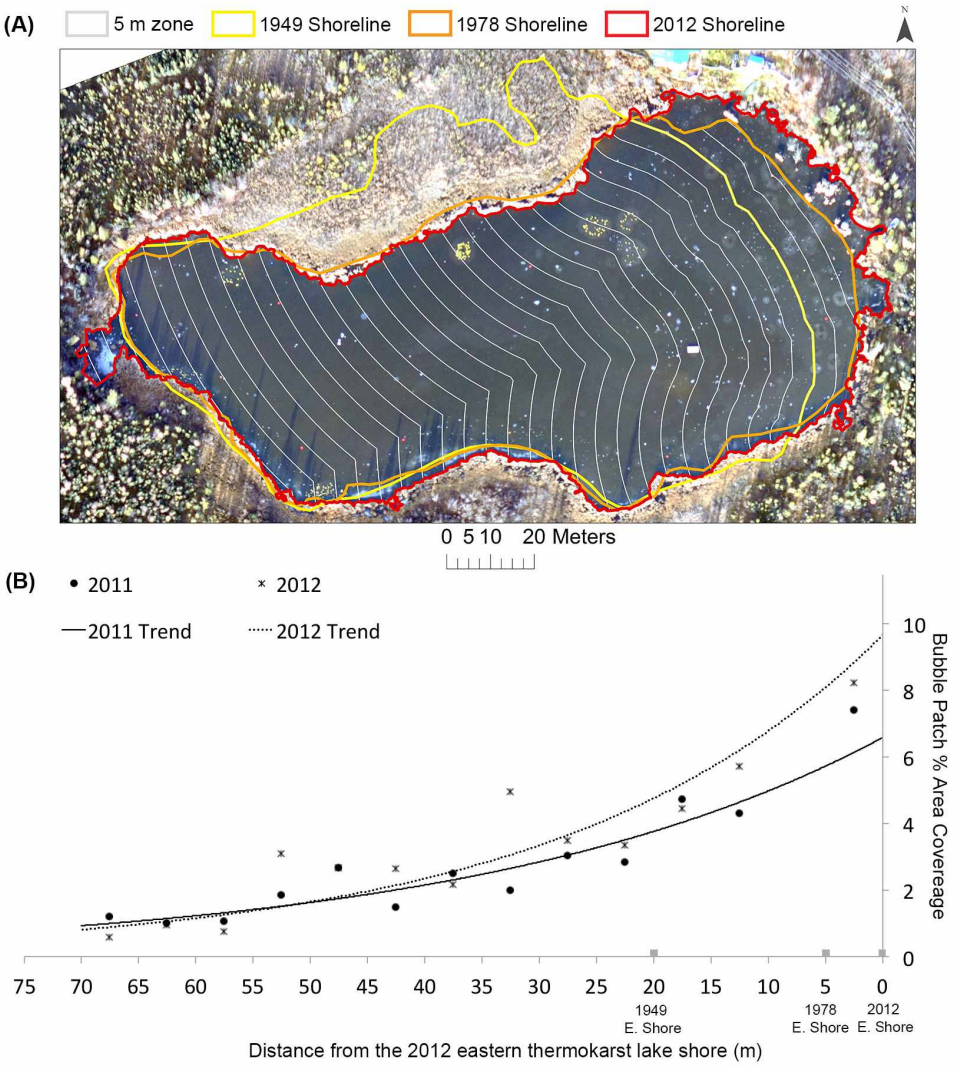

Year	Regression Equation	R^2	Standard Error
2011	Bubble % Coverage = $6.58*e^{\ln(\text{Distance from thermokarst margin})*-0.028}$	0.86	0.012
2012	Bubble % Coverage = $9.65*e^{\ln(\text{Distance from thermokarst margin})*-0.035}$	0.79	0.015

Figure 3.5. (a) Aerial image acquired on 14 October 2011 with lake perimeters from 1949 (yellow shoreline), 1978 (orange) and 2012 (red). Lake area change between 2011 and 2012 is minimal. The lake is divided in zones of 5 m width (white lines), for which percent bubble patch area was calculated for comparison to the distance from the rapidly expanding eastern lake margin. **(b)** Inverse exponential relationship between bubble patch percent cover and distance from the eastern thermokarst margin of Goldstream Lake, Fairbanks, Alaska.

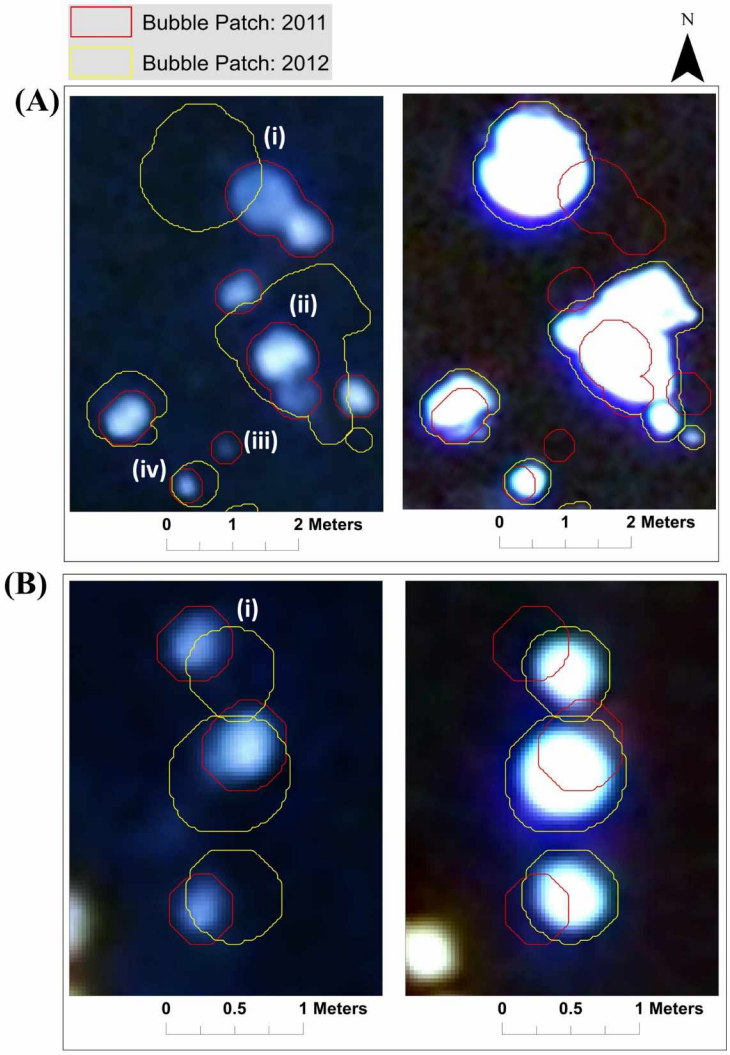

Figure 3.6. Comparison of bubble patches visible in thin lake ice two days after freeze-up in October 2011 (left-side images) and four days after freeze-up in October 2012 (right side images). Image pairs in **a** and **b** represent the same locations in 2011 and 2012. Four major characteristics of bubble patches are identified in panel **a**: (i) Bubble patches may shift up to 50 cm in location (geolocation error < 20 cm) in non-consistent directions; (ii) Bubble patch size and morphology varies between years during the first few days following freeze-up; (iii) Bubble patches visible during the first few days of freeze-up in one year are not visible during the first few days of freeze-up in another year; and (iv) Bubble patches are similar in shape but not in size. Panel **b** shows another example of horizontal shift of bubble patches (i).

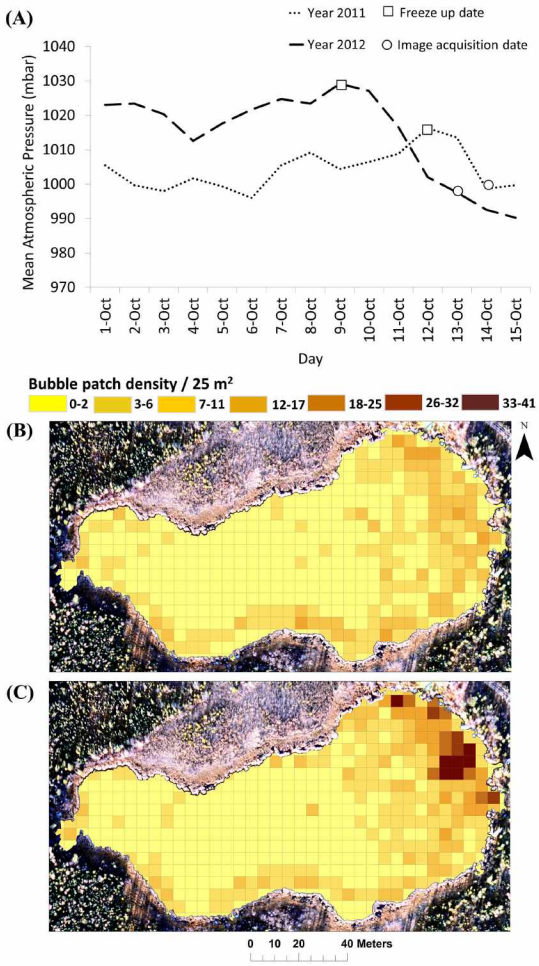

Figure 3.7. (a) The graph of mean daily atmospheric pressure (mbar) observed between 1-15 October in 2011 and 2012 shows that the magnitude of atmospheric pressure drop prior to image acquisition was twice as high in 2012 and 2011; pressure drops are known to induce ebullition. Bubble patch density in a 5 x 5 m grid as seen in the October images of the year **(b)** 2011; and **(c)** 2012. Generally darker grid cell colors in panels **b** and **c** suggest a higher density of seeps in 2012 compared to 2011, which is consistent with (1) a two-times longer period of ice formation (four days in 2012 vs. two days in 2011) for bubbles to accumulate and (2) atmospheric pressure patterns. Spatial distribution of bubble patches clearly shows a higher concentration of methane emission along the rapidly expanding eastern thermokarst margin in both years.

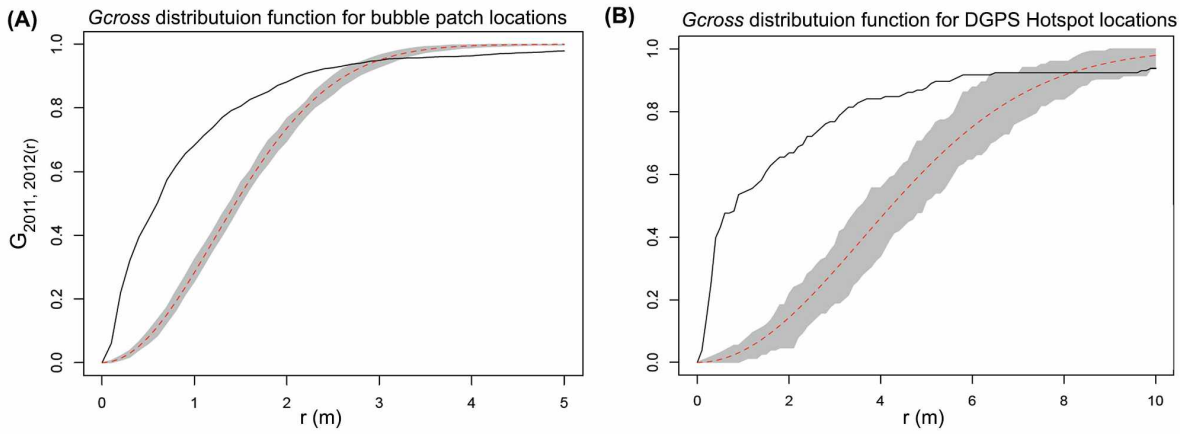

Figure 3.8. Cumulative distribution function of distances (r) between seeps identified in two different years 2011 and 2012. The black line shows actual observed data and the red line shows the theoretical expected value assuming the points are completely random. The gray shaded area shows a theoretical seep distance function for a random seep distribution (95% confidence band). The deviation between the observed empirical value (black curve) and theoretical expected value (red curve) suggests that a large and statistically significant number of seeps show spatial dependence between 2011 and 2012. **(a)** Distance function for bubble patches derived from image dataset. The actual curve is well above the theoretical curve over separation distances of 0 to 2 meters and thus a statistically significant number of second year bubble patch center points are less than 2 meters away from the first year center points. The actual curve is below the theoretical curve at the top after 3 meter distance separation suggesting that there are far less number of seeps at large distances; **(b)** Distance function for seeps derived from DGPS field-measured Hotspots. The observed function for the DGPS Hotspot locations rises almost vertically over separation distances of 0 to 1 meter deviating away from the theoretical function, i.e. a statistically significant number of Hotspot seeps did not move much from the first year location.

3.11. Tables

Table 3.1. Seep density and estimated mean whole-lake ebullition flux of Goldstrema Lake, Fairbanks, Alaska derived from 2011 and 2012 optical aerial image dataset and from ground surveys. The ground survey estimates are from previously published studies by Walter Anthony and Anthony, 2013, and Greene et al., 2014 based on ground survyes conducted over multiple years (2077-2011) at Goldstream Lake.

Surveys	Seep Density (seeps m^{-2})					Mean Whole-Lake Ebullition
	A	B	C	Hotspot	All Seeps	(ml gas m^{-2} d^{-1})
Aerial (14-Oct-11)	0.026	0.059	0.019	0.017	0.119	174±28
Aerial (13-Oct-12)	0.061	0.083	0.021	.021	0.185	216±33
Ground surveys	0.366	0.099	0.032	.011	0.508	170±54

3.12. References

Baddeley, A. and Turner, R.: Spatstat: An R package for analyzing spatial point patterns, J. Stat. Softw., 12, 1–42, www.jstatsoft.org (last access: August 2014), ISSN: 1548–7660, 2005.

Bastviken, D.: Methane emissions from lakes: Dependence of lake characteristics, two regional assessments, and a global estimate, Global Biogeochem. Cy., 18, 1–12, doi:10.1029/2004GB002238, 2004.

Bastviken, D., Tranvik, L. J., Downing, J. A., Crill, P. M., and Enrich-Prast, A.: Freshwater methane emissions offset the continental carbon sink, Science, 331, 6013, doi:10.1126/science.1196808, 2011.

Bivand, R. S., Pembesma, E. J., and Gomez-Rubio, V.: Applied Spatial Data Analysis with R, Springer, New York, 2008.

Blaschke, T. and Strobl, J.: What's wrong with pixels? Some recent developments interfacing remote sensing and GIS, GIS – Zeitschrift für Geoinformationssysteme, 14, 12–17, 2001.

Blaschke, T., Lang, S., and Hay, G. J.: Object based image analysis: Spatial concepts for knowledge-driven remote sensing applica- tions, Springer-Verlag Berlin, Heidelberg, Germany, 2008.

Brosius, L. S., Walter Anthony, K. M., Grosse, G., Chanton, J. P., Farquharson, L. M., Overduin, P. P., and Meyer, H.: Using the deuterium isotope composition of permafrost meltwa- ter to constrain thermokarst lake contributions to atmospheric CH_4 during the last deglaciation, J. Geophys. Res., 117, G01022, doi:10.1029/2011JG001810, 2012.

Casper, P., Maberly, S. C., Hall, G. H., and Finlay, B. J.: Fluxes of methane and carbon dioxide from a small productive lake to the atmosphere, Biogeochemistry, 49, 1–19, 2000.

Definiens: Segmentation Algorithms In Definiens Developer 7 Reference Book, Document Version 7.0.0.843, 15–27, Definiens AG, München, Germany, 2007.

Engram, M., Walter Anthony, K. M., Meyer, F. J., and Grosse, G.: Synthetic aperture radar (SAR) backscatter response from methane ebullition bubbles trapped by thermokarst lake ice, Can. J. Remote Sens., 38, 667–682, 2012.

Fechner-Levy, E. J. and Hemond, H. F.: Trapped methane volume and potential effects on methane ebullition in a northern peatland, Limnol. Oceanogr., 41, 1375–1383, 1996.

Glaser, P. H., Chanton, J. P., Morin, P., Rosenberry, D. O., Siegel, D. I., Ruud, O., Chasar, L. I., and Reeve, A. S.: Sur- face deformations as indicators of deep ebullition fluxes in a large northern peatland, Global Biogeochem. Cy., 18, GB1003, doi:10.1029/2003GB002069, 2004.

Greene, S., Walter Anthony, K. M., Archer, D., Sepulveda-Jauregui, A., and Martinez-Cruz, K.: Modeling the impediment of methane ebullition bubbles by seasonal lake ice, Biogeosciences, 11, 6791-6811, doi:10.5194/bg-11-6791-2014, 2014.

Grosse, G., Harden, J., Turetsky, M., McGuire, A. D., Camill, P., Tarnocai, C., Frolking, S., Schuur, E. A. G., Jorgen- son, T., Marchenko, S., Romanovsky, V., Wickland, K. P., French, N., Waldrop, M., Bourgeau-Chavez, L., and Striegl, R. G.: Vulnerability of high-latitude soil organic carbon in North America to disturbance, J. Geophys. Res., 116, 1–23, doi:10.1029/2010JG001507, 2011.

Grosse, G., Jones, B., and Arp, C.: Thermokarst Lakes, Drainage and Drained Basins, Treatise Geomorphol., 8, 325–353, 2013.

Hinzman, L. D., Bettez, N. D., Bolton, W. R., Chapin, F. S., Dyurgerov, M. B., Fastie, C. L., Griffith, B., Hollister, R. D., Hope, A., Huntington, H. P., Jensen, A. M., Jia, G. J., Jorgenson, T., Kane, D. L., Klein, D. R., Kofinas, G., Lynch, A. H., Lloyd, A. H., Mcguire, A. D., Nelson, F. E., Oechel, W. C., Osterkamp, T. E., Racine, C. H., Romanovsky, V. E., Stone, R. S., Stow, D. A., Sturm, M., Tweedie, C. E., Vourlitis, G. L., Walker, M. D., Walker, D. A., Webber, P. J., Welker, J. M., and Winker, K. S.: Evidence and Implications of Recent Climate Change in Northern Alaska and Other Arctic Regions, Climatic Change, 72, 251– 298, doi:10.1007/s10584-005-5352-2, 2005.

Hugelius, G., Strauss, J., Zubrzycki, S., Harden, J. W., Schuur, E. A. G., Ping, C. L., Schirrmeister, L., Grosse, G., Michaelson, G. J., Koven, C. D., O'Donnell, J. A., Elberling, B., Mishra, U., Camill, P., Yu, Z., Palmtag, J., and Kuhry, P.: Estimated stocks of circumpolar permafrost carbon with quantified uncertainty ranges and identified data gaps, Biogeosciences, 11, 6573-6593, doi:10.5194/bg-11-6573-2014, 2014.

Jeffries, M. O., Morris, K., and Kozlenko, N.: Ice Characteristics and Remote Sensing of Frozen Rivers and Lakes, Remote Sensing in Northern Hydrology, Geoph. Monog. Series, 163, 63–90, 2005.

Jorgenson, M. T. and Shur, Y.: Evolution of lakes and basins in northern Alaska and discussion of the thaw lake cycle, J. Geo- phys. Res., 112, 1–12, doi:10.1029/2006JF000531, 2007.

Kanevskiy, M., Shur, Y., Fortier, D., Jorgenson, M. T., and Stephani, E.: Cryostratigraphy of late Pleistocene syngenetic permafrost (yedoma) in northern Alaska, Itkillik River exposure, Quaternary Res., 75, 584–596, doi:10.1016/j.yqres.2010.12.003, 2011.

Keller, M. and Stallard, R. F.: Methane emission by bubbling from Gatun Lake, Panama, J. Geophys. Res., 99, 8307–8319, doi:10.1029/92JD02170, 1994.

Kessler, M. A., Plug, L. J., and Walter Anthony, K. M.: Simulating the decadal- to millennial-scale dynamics of morphology and sequestered carbon mobilization of two thermokarst

lakes in NW Alaska, J. Geophys. Res.-Biogeo., 117, 1–22, doi:10.1029/2011JG001796, 2012.

Kokelj, S. V. and Jorgenson, M. T.: Advances in thermokarst research, Permafrost Periglac., 24, 108–119, doi:10.1002/ppp.1779, 2013.

Koven, C. D., Ringeval, B., Friedlingstein, P., Ciais, P., Cadule, P., Khvorostyanov, D., Krinner, G., and Tarnocai, C.: Permafrost carbon-climate feedbacks accelerate global warming, P. Natl. Acad. Sci. USA, 108, 14769–14774, doi:10.1073/pnas.1103910108, 2011.

Lindgren, P. R., Grosse, G., Meyer, F. J., and Walter Anthony, K. M.: Development of an object-based classification model to detect methane ebullition bubbles in early winter lake ice, in preparation, 2015.

Mather, P.: Pattern Recognition Principles In Classification for Re- motely Sensed Data, Second Edn., CRC Press, New York, 41–75, 2009.

Mattson, M. D. and Likens, G. E.: Air pressure and methane fluxes, Nature, 347, 718–719, 1990.

Navulur, K.: Multispectral image analysis using the object-oriented paradigm, CRC Press, Boca Raton, FL, 2007.

Péwé, T. L.: Quaternary geology of Alaska, US Geol. Survey Professional Paper 835, 1–145, 1975.

Plug, L. J. and West, J. J.: Thaw lake expansion in a two- dimensional coupled model of heat transfer, thaw subsidence, and mass movement, J. Geophys. Res., 114, F01002, doi:10.1029/2006JF000740, 2009.

Rowland, J. C., Travis, B. J., and Wilson, C. J.: The role of advective heat transport in talik development beneath lakes and ponds in discontinuous permafrost, Geophys. Res. Lett., 38, 1–5, doi:10.1029/2011GL048497, 2011.

Scandella, B. P., Varadharajan, C., Hemond, H. F., Ruppel, C., and Juanes, R.: A conduit dilation model of methane venting from lake sediments, Geophys. Res. Lett., 38, 1–6, doi:10.1029/2011GL046768, 2011.

Schuur, E. A. G., Bockenheim, J., Canadell, J. P., Euskirchen, E., Field, C. B., Goryachkin, S. V., Hagemann, S., Kuhry, P., Lafleur, P. M., Lee, H., Mazhitova, G., Nelson, F. E., Rinke, A., Ro- manovsky, V. E., Shiklomanov, N., Tarnocai, C., Venevsky, S., Vogel, J. G., and Zimov, S. A.: Vulnerability of permafrost carbon to climate change: implications for the global carbon cycle, BioScience, 58, 701–714, doi:10.1641/B580807, 2008.

Smith, L. C., Sheng, Y., and MacDonald, G. M.: A first pan-Arctic assessment of the influence of glaciation, permafrost, topography and peatlands on northern hemisphere lake distribution, Permafrost Periglac., 18, 201–208, 2007.

Tokida, T., Miyazaki, T., and Mizoguchi, M.: Ebullition of methane from peat with falling atmospheric pressure, Geophys. Res. Lett., 32, L13823 doi:10.1029/2005GL022949, 2005.

Varadharajan, C.: Magnitude and spatio-temporal variability of methane emissions from a eutrophic freshwater lake, PhD thesis, Massachusetts Institute of Technology, Cambridge, MA, 2009.

Walter, K. M., Zimov, S. A., Chanton, J. P., Verbyla, D., and Chapin, F. S.: Methane bubbling from Siberian thaw lakes as a positive feedback to climate warming, Nature, 443, 71–75, doi:10.1038/nature05040, 2006.

Walter, K. M., Smith, L. C., and Chapin, F. S.: Methane bubbling from northern lakes: present and future contributions to the global methane budget, Philos. T. R. Soc. A, 365, 1657–1676, doi:10.1098/rsta.2007.2036, 2007.

Walter, K. M., Engram, M., Duguay, C. R., Jeffries, M. O., and Chapin, F. S.: The potential use of Synthetic Aperture Radar for estimating methane ebullition from Arctic lakes, J. Am. Water Resour. As., 44, 305–315, 2008.

Walter Anthony, K., Vas, D. A., Brosius, L., Chapin III, F. S., and Zimov, S. A.: Estimating methane emissions from northern lakes using ice-bubble surveys, Limnol. Oceanogr.-Meth., 8, 592–609, 2010.

Walter Anthony, K. M. and Anthony, P.: Constraining spatial variability of methane ebullition seeps in thermokarst lakes using point process models, J. Geophys. Res.-Biogeo., 118, 1–20, doi:10.1002/jgrg.20087, 2013.

Walter Anthony, K. M., Anthony, P., Grosse, G., and Chanton, J.: Geologic methane seeps along boundaries of Arctic permafrost thaw and melting glaciers, Nat. Geosci., 5, 419–426, doi:10.1038/ngeo1480, 2012.

Walter Anthony, K. M., Zimov, S. A., Grosse, G., Jones, M. C., An- thony, P., Chapin III, F. S., Finlay, J. C., Mack, M. C., Davydov, S., Frenzel, P., and Frolking, S.: A shift of thermokarst lakes from carbon sources to sinks during the Holocene epoch, Nature, 511, 452–456, doi:10.1038/nature13560, 2014.

West, J. J. and Plug, L. J.: Time-dependent morphology of thaw lakes and taliks in deep and shallow ground ice, J. Geophys. Res., 113, 1–14, doi:10.1029/2006JF000696, 2008.

Wik, M., Crill, P. M., Bastvikenm D., Danielsson, Å., and Nor- bäck, E.: Bubbles trapped in arctic lake ice: Potential implications for methane emissions, J. Geophys. Res., 116, 1–10, doi:10.1029/2011JG001761, 2011.

Zimov, S. A., Voropaev, Y. V., Semiletov, I. P., Davidov, S. P., Prosiannikov, S. F., Chapin III, F. S., Chapin, M. C., Trumbore, S., and Tyler, S.: North Siberian Lakes: A methane source fueled by Pleistocene carbon, Science, 277, 800–802, doi:10.1126/science.277.5327.800, 1997.

Zimov, S. A., Davydov, S. P., Zimova, G. M., Davydova, A. I., Schuur, E. A. G., Dutta, K., and Chapin III, F. S.: Permafrost carbon: Stock and decomposability of a glob- ally significant carbon pool, Geophys. Res. Lett., 33, , 1–5, doi:10.1029/2006GL027484, 2006.

Chapter 4. Characterizing post-drainage succession in thermokarst lake basins on the Seward Peninsula, Alaska with TerraSAR-X backscatter and Landsat-based NDVI data[3]

4.1. Abstract

Drained thermokarst lake basins accumulate significant amounts of soil organic carbon in the form of peat, which is of interest to understanding carbon cycling and climate change feedbacks associated with thermokarst in the Arctic. Remote sensing is a tool useful for understanding temporal and spatial dynamics of drained basins. In this study, we tested the application of high-resolution X-band Synthetic Aperture Radar (SAR) data of the German TerraSAR-X satellite from the 2009 growing season (July–September) for characterizing drained thermokarst lake basins of various age in the ice-rich permafrost region of the northern Seward Peninsula, Alaska. To enhance interpretation of patterns identified in X-band SAR for these basins, we also analyzed the Normalized Difference Vegetation Index (NDVI) calculated from a Landsat-5 Thematic Mapper image acquired on July 2009 and compared both X-band SAR and NDVI data with observations of basin age. We found significant logarithmic relationships between (a) TerraSAR-X backscatter and basin age from 0 to 10,000 years, (b) Landsat-5 TM NDVI and basin age from 0 to 10,000 years, and (c) TerraSAR-X backscatter and basin age from 50 to 10,000 years. NDVI was a better indicator of basin age over a period of 0–10,000 years. However, TerraSAR-X data performed much better for discriminating radiocarbon-dated basins (50–10,000 years old). No clear relationships were found for either backscatter or NDVI and basin age from 0 to 50 years. We attribute the decreasing trend of backscatter and NDVI with increasing basin age to post-drainage changes in the basin surface. Such changes include succession in vegetation, soils, hydrology, and renewed permafrost aggradation, ground ice accumulation and localized frost heave. Results of this study show the potential application of X-band SAR data in combination with NDVI data to map long-term succession dynamics of drained thermokarst lake basins.

---

[3] Regmi, P., Grosse, G., Jones, M. C., Jones, B. M., Walter Anthony, K., 2012. Characterizing post-drainage succession in thermokarst lake basins on the Seward Peninsula, Alaska with TerraSAR-X backscatter and Landsat-based NDVI, *Remote Sensing,* 4, 3741–3765. doi:10.3390/rs4123741

4.2. Introduction

Thermokarst lakes and drained thermokarst lake basins (DTLBs) are important indicators of permafrost and thermokarst dynamics in arctic and subarctic lowlands with ice-rich permafrost [1–5]. In Alaska, they occupy a large portion of the Arctic Coastal Plain, the Arctic Foothills and the Seward Peninsula [6–8], forming a complex and dynamic landscape with repeated cycles of lake formation and drainage due to permafrost degradation and aggradation [9–11]. Moreover, DTLBs accumulate soil organic carbon (SOC) in the form of peat, which has important implications for northern SOC pool distribution and high-latitude carbon cycling [10,12,13].

Recent attention has focused on the effect of projected climate warming on the rate of microbial decomposition of SOC stored in northern permafrost and peatland regions that will have an impact on greenhouse gas release to the atmosphere [14–17]. Under warming conditions, northern SOC pools have the potential for large emissions of methane (CH4) or carbon dioxide (CO2), depending on the soil aerobic regime, due to an enhanced rate of microbial decomposition of organic matter that will serve as a positive feedback to climate warming [17,18]. However, the amount of carbon sequestered in DTLBs and its role for the carbon budget in permafrost regions in a warming scenario is yet to be quantified for the Arctic.

Jones et al. [10] and Hinkel et al. [12] demonstrated that basin age can be used to estimate peat thickness and accumulation rates in DTLBs. Long-term dynamics of DTLBs are characterized by post-drainage changes in vegetation, surface hydrology, soil characteristics and often permafrost aggradation, following a relatively predictable pattern reflecting successional stage or the relative age of the drained basin [9,10,12,19,21]. Important processes that shape the evolution of thermokarst lakes and DTLBs include permafrost thaw, ground subsidence and related erosion, ponding, surface and subsurface lake drainage, as well as post-drainage ground ice accumulation and frost heave [5,20,21]. Various models of a "thaw-lake cycle" were proposed to explain the geomorphic processes of origin and drainage of thermokarst lakes [21–24]. The cycle may begin with formation of ponds at the intersection of ice-wedge troughs and in low-center polygons, which upon continued permafrost thaw, eventually coalesce and enlarge to small lakes. As a result of thermo-mechanical shore erosion and thaw slumping, lake dimensions increase over time, both radially and in depth depending on the excess ice content of the permafrost [25–27]. A first cycle is ended when lake drainage is triggered by stream piracy,

tapping, bank overflow or ice-wedge erosion [22,28]. In thin discontinuous permafrost, thermokarst lakes may drain internally through open taliks [20]. Following drainage, re-vegetation and peat accumulation begins in drained basins [10,19,29,30]. Wet, graminoid vegetation is established in recently drained basins in 5–10 years, and peat accumulation starts in the first 20–100 years since drainage [10]. As a result of exposing the lake bottom, cold winter frost can penetrate into the ground, and new permafrost aggradation begins in the drained lake basin [31]. Additionally, over time, basin productivity decreases as wet graminoid vegetation communities, including productive grass (Calamagrostis and Dupontia) and sedge fens (Carex aquatilis), are replaced by ericaceous bog and tussock-dominated ecosystems. Zona et al. [32] have shown very high Gross Primary Productivity (GPP) for graminoid vegetation of younger DTLBs compared to the vegetation community of older DTLBs in Arctic ecosystems. This vegetative succession occurs as nutrients from the fresh lake sediments are consumed, permafrost aggradation causes limitations in rooting depth and liquid water availability, and ground ice formation and frost heave result in surface drying [10,32]. Over time, low-centered ice wedge polygons start to develop in drained basins, indicating the accumulation of massive ground ice bodies [33], which eventually creates preconditions for new ponding and the beginning of a new thermokarst lake cycle [12].

Previously, the thermokarst lake cycle was assumed to have a duration of 2,000–3,000 years in some regions of northwestern Alaska [8,34], but recent studies show that some drained basins older than 5,000 years before present (BP) persisted as basins without redeveloping into a lake [12]. Also, mechanisms associated with ground ice dynamics in the thermokarst lake cycle have remained controversial, and the hypothesis that thermokarst lakes evolve in a direct cyclic order has been questioned for the northern Alaskan Coastal Plain [21]. For the northern Seward Peninsula, Jones et al. [10] and Kessler et al. [35] demonstrated that frequency and timing of a thermokarst lake cycle depends on local factors, such as topography, ground ice content and distribution with depth, climate and the geomorphology and history of lake/basin configurations. A recent study has also found that thermokarst lake "cycling" often is not based on formation of new lakes in a DTLB, but linked to erosion from neighboring lakes that preferentially expand into the low banks of DTLB [27]. Understanding the temporal and spatial dynamics of DTLBs requires substantial geological, cryolithological and geochronological groundwork in remote

regions of the Arctic. Application of remote sensing methods to map drained lake basins and their surface properties is a critical component in upscaling such field results to larger regions. In the past, a number of studies have exploited moderate and low resolution satellite images derived from optical sensors to map DTLBs, evaluate their spatial and temporal dynamics, as well as classify their relative age, relying on relationships of land surface properties to post-drainage succession in vegetation, soils and permafrost aggradation [9,10,12,36]. Hinkel et al. [12] utilized Landsat-7 Enhanced Thematic Mapper Plus (ETM+) imagery to study the spatial extent of DTLBs and classify their relative age on the Barrow Peninsula, Alaska. For age-classification, they established a relationship between radiocarbon-dated surface peat and spectral and textural properties of basins, determined by factors such as vegetation type, degree of ponding and ice wedge polygon development, basin wetness and texture. Zulueta et al. [36] used Moderate Resolution Imaging Spectroradiometer (MODIS) data to link aircraft-based CO_2 flux estimates with NDVI of DTLBs at different successional stages for the same region. Jones et al. [10] used Landsat-5 Thematic Mapper (TM) based Normalized Differential Vegetation Index (NDVI), as well as Minimum Noise Fraction (MNF), to estimate carbon stocks stored in the uppermost peat deposits (~ 50–60 cm) of DTLBs of the northern Seward Peninsula, Alaska. However, remote sensing data derived from optical sensors is generally limited to surface conditions and does not penetrate into the soil. Hence, optical remote sensing data does not reveal much information about soil moisture conditions, which should be a good indicator of basin successional stage, particularly centuries after drainage, when basin vegetation succession slows down. SAR remote sensing data has been frequently used to detect soil surface moisture due to its sensitivity to soil's dielectric constant [37–40]. In addition, SAR sensors also have advantage over optical remote sensing in Arctic regions, as they can image the Earth's surface in all weather conditions and at any time of the day.

In this study, we investigated the application of high resolution X-band SAR data of the German TerraSAR-X (TSX) satellite for determining the time since lake drainage (or drained basin age) based on basin surface properties and to understand the post-drainage succession dynamics for a set of DTLBs. Contrary to most previous studies that investigated post-drainage succession patterns of DTLBs on the Alaska Arctic Coastal Plain, we here study DTLBs located in the ice-rich permafrost region of the northern Seward Peninsula, Alaska, where mean annual

ground and mean annual air temperatures are warmer than in the Arctic Coastal Plain, and where yedoma permafrost and its large soil carbon pool are particularly vulnerable to climate change. This allows an interesting comparison of basin succession patterns across a permafrost and climate gradient.

In the context of radar applications, backscatter at short wavelengths, such as X-band, in vegetated areas is largely dominated by scattering processes in the crown layer of branches and foliage of the canopy and is less sensitive to background properties, such as soil moisture content, while soil moisture will have greater influence on backscatter in the case of exposed soil surface or ground with a thin layer of vegetation [41]. But, the retrieved signal in areas of sparse vegetation corresponds to combined signatures of vegetation and ground properties. The backscatter from vegetation canopies is also affected by many factors, including plant moisture content, size, shape and orientation and distribution of the scatters in a canopy with respect to the sensor's viewing angle [41]. We also utilized NDVI derived from Landsat-5 TM to aid in the interpretation of basin backscatter signal and the understanding of vegetation succession dynamics in DTLBs. NDVI is sensitive to plant biomass and can be useful to differentiate tundra vegetation type [42] in DTLBs at various stages [32,36]. This further helps to identify major biophysical parameters that are influencing basin backscatter. To compare TSX backscatter data with basin age, we used a set of 14 basins that were previously radiocarbon-dated by Jones et al. [10], as well as 60 drained basins identified in aerial and satellite images acquired during 1950–2010 [43].

4.3. Study area

This study was conducted for an area of approximately 3,800 km^2 on the northern Seward Peninsula, Alaska (66.5°N, 164.5°W; Figure 4.1). The study area is situated in an ice-rich permafrost region and is largely covered by thermokarst-affected terrain with a large number of thermokarst lakes and DTLBs and erosional remnants of uplands. The northern Seward Peninsula is identified as one of the major lake districts of Alaska, where 7% of the 6,418 km^2 coastal lowland area is covered with lakes larger than 1 hectare [44] (Figure 4.1). Thermokarst lakes in the lowland plain of the region mainly formed as a result of permafrost degradation due to warming throughout the Holocene [8,45]. Currently, the mean annual ground temperature is recorded as ~ −3 °C [46]. This allows for current formation of permafrost and epigenetic ice

wedges following drainage of thermokarst lakes in the region [47]. The depth of permafrost exceeds 90 m [47] and the active layer is 0.3–0.6 m thick [25]. The permafrost thickness very likely varies due to the distribution and thermal impact of thermokarst lakes [46,48]. However, detailed data on permafrost distribution and thickness is not available for the Seward Peninsula.

The elevation in the study area ranges from close to sea level near the coast, to less than 50 m in most of the uplands that consist of erosional remnants of ice-rich deposits. The landscape is dominated by tundra-type vegetation, which is classified as Bering Tundra [44]. Recently drained thermokarst lake basins are dominated by productive grasses, such as *Calamagrostis canadensis* and *Dupontia fisherii* [10]. The sedge *Carex aquatilis* is also common in some of the very productive younger basins. Older DTLBs have a higher component of a less productive plant community that includes *Carex bigelowii*, *Eriophorum angustifolium* and *Sphagnum sp.* tundra with *Betula nana*, *Salix sp.* and prostrate ericaceous shrubs [10]. Dry surfaces in the older basins, due to heave from reformation of ground ice and the presence of mature ice wedge polygon ridges, may show abundant lichen [10].

Climate in this region is characterized by long cold winters and short growing seasons (May–September) [49]. The mean annual air temperature of the region is − 6.1 °C, and the mean annual precipitation is 255 mm, with roughly 125 mm falling in the form of snow based on historical summaries for the period 1971–2000 recorded at Kotzebue, Alaska [27], which is located 60 km to the northeast, but has a similar coastal position as the northern Seward Peninsula [25].

4.4. Data

4.4.1. Remotely sensed data

We acquired six TSX stripmap HH polarization images with 3 m spatial resolution (Table 4.1). The scenes were acquired during the 2009 growing season between 20 July and 20 September (Figure 4.1). The image product was received in Multi Look Ground Range Detected (MGD) format with reduced speckle and approximately square resolution cells [50]. To derive NDVI, we utilized a terrain corrected Landsat-5 TM (L1T) scene with 30 m spatial resolution, the best available optical remote sensing data overlapping with our SAR dataset from the growing season of the year 2009 (Table 4.1). The dataset was received from the United States Geological Survey

(USGS) Earth Resources Observation Systems (EROS) center. The image was acquired on 13 July 2009, around the time of mid-growing season when plant growth has reached sufficient levels and NDVI allows better differentiation of vegetation status [51,52]. We further investigated the surface properties of DTLBs by visually analyzing high resolution oblique aerial photographs of several of the DTLBs and a few available Quickbird and Ikonos images. Aerial photographs were collected in June of 2010 and 2011, whereas the Quickbird and Ikonos images were acquired in the growing season of the year 2006 and 2007.

4.4.2. DTLB data layer

We used a set of 74 DTLBs covered in TSX scenes with known age since drainage (Figure 4.1). For 14 of these DTLBs, age was determined using accelerated mass spectrometry (AMS) radiocarbon-dating of the basal portion of terrestrial peat covering lake sediments, ranging in the age from 225 to 9,410 years BP [10]. For another 60 DTLBs (3–47 years old), the age since their last drainage was determined from multi-sensor aerial and satellite image time series covering the 1950–2010 period using the change detection technique [43]. The ages of these DTLBs were used to compare SAR backscatter and surface spectral properties of each basin for determination of relationships of basin age with backscatter and with NDVI. All radiocarbon-dated basins were completely drained, while basins that drained in the past decades were either partially (approximately less than 10% water by basin area observed in 2009 images) or completely drained.

4.5. Methods

4.5.1. Image processing

Absolute radiometric calibration and orthorectification of TSX data was done with GAMMA^{TM} software. The best available digital elevation model (DEM) for our study region, the National Elevation Dataset (NED) with 60 m spatial resolution, was used to perform orthorectification. The performance of this correction was assessed visually by overlaying geocoded TSX images on the terrain-corrected Landsat-5 TM image. Speckle removal in the TSX images was performed using IDRISITM image processing software by applying a 5X5 window mean filter. Since GAMMA provided the radar backscatter (σ°) values in linear unit (intensity values), they were converted to decibels (dB) after we performed filtering and extracted the mean backscatter

value of drained basins for further analysis. A NDVI dataset was produced using Landsat-5 TM band-3 (red) and band-4 (near infrared) using Equation (4.1) [53].

$$\text{NDVI} = \frac{\text{Near Infrared} - \text{Red}}{\text{Near Infrared} + \text{Red}} \qquad \text{(Equation 4.1)}$$

Since the objective of the study was to investigate the relationship between backscatter and NDVI with basin age, remnant water bodies in all DTLBs were masked from all TSX scenes, as well as the Landsat NDVI image using IDRISI software. To mask water bodies, a threshold method separating land from water surfaces was applied to the TSX images, and the same method was applied to band-5 (first shortwave infrared band) of the Landsat image. A threshold of −14 dB was chosen to mask out water bodies from TSX images, and a threshold of 31 DN (digital numbers) was chosen for Landsat band 5.

4.5.2. TSX backscatter and NDVI of DTLBs

Both backscatter and NDVI of DTLBs were examined using the desktop geographical information system (GIS) software ArcMap 10. Using the Zonal Statistics tool, the mean backscatter value (σ° intensity) of 60 DTLBs (younger than 50 years) was extracted from all six TSX scenes, and the mean backscatter (σ° intensity) of 14 radiocarbon-dated DTLBs (older than 50 years) was extracted from 27 August and 09 September 2009 TSX scenes. We selected these two scenes because their spatial coverage includes all 14 radiocarbon-dated DTLBs completely. The final mean σ° was converted from intensity to dB. We could extract NDVI of only 57 modern DTLBs that were visible in the cloud- and cloud shadow-free portions of the Landsat image from 13 July 2009. We were able to extract NDVI for all 14 radiocarbon-dated DTLBs. Mean basin backscatter (dB) and mean basin NDVI were used to investigate the backscatter and spectral properties of DTLBs with different ages. We used age classes based on calendar years in correspondence with those used by Jones et al. [10] (Table 4.2): 0–50 years (modern), 50–500 years (young), 500–2,000 years (medium), 2,000–5,000 years (old) and older than 5,000 years (ancient).

To investigate the relationship between backscatter and NDVI of DTLBs, we performed a regression analysis between mean basin backscatter and mean basin NDVI with basin age in three subsets of our DTLB dataset: (1) 0–50 years since drainage, or modern DTLBs; (2) 50–

10,000 years since drainage, or radiocarbon-dated DTLBs; and (3) 0–10,000 years since drainage, or combined modern and radiocarbon-dated DTLBs.

The analysis of mean backscatter versus basin age was performed for each TSX image separately on all 60 modern DTLBs that were covered by respective scenes acquired on different dates (Figure 4.1) to avoid biases in our basin age analysis that could be produced from seasonal dynamics of basin parameters. Similarly, for 14 radiocarbon dated DTLBs, we used mean basin backscatter extracted from 27 August 2009 and 09 September 2009 TSX scenes (Figure 4.1) to investigate if backscatter signals reflect their successional stage. Mean NDVI of 57 modern and 14 radiocarbon-dated DTLBs were used to investigate the relationship between NDVI of modern and radiocarbon-dated DTLBs and their age.

To explore the relationship between backscatter properties with age of basins ranging from 0 to 10,000 years, we analyzed backscatter signals of DTLBs that were covered in 27 August 2009 and 09 September 2009 TSX scenes separately. Also, we explored the relationship between NDVI signals on 13 July of these basins with their age. We excluded three modern DTLBs from our analysis of basin backscatter and NDVI due to clouds or cloud shadows or being located outside of the Landsat extent from our analysis to make the basin backscatter property comparable with its NDVI property. In total, there were 39 DTLBs, among which 25 were modern and 14 were radiocarbon-dated.

4.6. Results

4.6.1. TSX backscatter and NDVI properties of modern DTLBs (0–50 years since drainage) analysis

Analysis of TSX backscatter of modern DTLBs did not result in a clear relationship between basin age and mean basin backscatter. We did not find strong relationships for 16 and 29 August ($R^2 < 0.25$, $p < 0.05$), and no statistically significant relations were established for other dates. Also a strong relationship could not be established between NDVI on 13 July and basin age for modern basins ($R^2 < 0.25$, $p < 0.05$).

During aerial field surveys, we observed strong local variation in early post-drainage surface backscatter and NDVI properties within most modern basins based on varying vegetation communities and variable soil moisture conditions (Figure 4.2(a,b)). Additionally, backscatter

and NDVI properties varied between modern basins of the same age. Most of the vegetated DTLBs that drained in the last five years consisted of early assemblages of highly productive, high canopy (50–130 cm tall) graminoid vegetation, often densely growing in very shallow water (<30 cm deep) (Figure 4.2(a)). These DTLBs exhibited the highest NDVI, but had a very low backscatter signal. Some of the DTLBs were still in the process of draining (Figure 4.2(b)). Many of the partially drained basins contained lush vegetation growing in remnant ponds, some of which was partly emergent from the water, but did not cover the water surface uniformly, while other areas formed floating vegetation mats growing around the edges of water surfaces [54]. Such DTLBs dominated by emergent vegetation and floating vegetation showed a very high X-band backscatter. However, their NDVI was highly variable depending on vegetation type and density versus open water areas in between patches of vegetation. Further, some DTLBs had areas drained more and primarily covered with moss and lichen. This type of surface exhibited relatively low NDVI and intermediate to low backscatter.

4.6.2. TSX backscatter and NDVI properties of radiocarbon-dated DTLBs (50–10,000 years since drainage)

Analysis of TSX backscatter on 27 August of the radiocarbon-dated DTLBs indicated a significant logarithmic relationship ($R^2 = 0.58$; $p < 0.05$) between basin age and mean basin backscatter (Figure 4.3). Younger radiocarbon-dated DTLBs showed higher backscatter, while backscatter decreased for older and ancient basins. However, there was no significant relationship between 09 September backscatter and basin age. Similarly, NDVI from 13 July did not show a significant relation between NDVI of DTLBs and their radiocarbon-dated age.

Young DTLBs had relatively high backscatter values that ranged between − 6.1 dB and − 5.5 dB. They had variable but relatively high NDVI values. They largely had not yet developed polygonal networks and had more productive vegetation than older basins (Figure 4.2(c)), except one that drained 294 years BP situated in the northern coastal lowland. This particular basin was less productive, also indicated by its very low NDVI value, and had developed early stage low-centered polygons. The basins were already characterized by drier surfaces and were affected by frost heave. We observed that DTLBs of medium age (younger than ~1,000 years BP) were generally drier and exhibited early low-center ice-wedge polygonal networks (Figure 4.2(d)). Consequently, backscatter values decreased within the range of − 6.7 dB and − 6 dB for these

basins. They generally had similar vegetation cover and NDVI to that of young DTLBs, but with much less variability, indicating homogenization of vegetation cover in the basins with ongoing succession. Only one medium-aged basin dated to 615 years BP in the northern coastal lowland had already developed characteristics of older medium aged DTLBs (older than ~ 1,000 years). Older medium aged DTLBs exhibited lower backscatter. They had fully established low-centered polygonal networks with some wet centers and ponded polygons. Moreover, less productive lowland tundra vegetation had dominated these basin floors.

Mean basin backscatter values continued to decrease for old and ancient DTLBs ranging between − 7.1 dB and − 6.2 dB. Old and ancient DTLBs were characterized by fully established ice-wedge polygonal networks either with dry soil surfaces or with a significant number of ponded low-centered polygons in some cases, indicating the potential for coalescence into a new lake. DTLBs with a large topographic gradient within and downstream of their drainage channels often did not appear to pool sufficient surface runoff for forming new ponds and development into a new lake, while basins with a low topographic gradient had often more ponds. We observed emergent vegetation in some of the inundated centers of the polygons. Such parts of DTLBs exhibited high backscatter. Some old DTLBs also contained fully developed large hydrostatic pingos. These pingos exhibited high NDVI compared to the basin floor surrounding it, but their backscatter signal was affected by geometric distortion on the steep pingo slopes. Geometric distortion, an inherent problem in SAR acquisition mainly of rugged terrain, is a spatial distortion due to complex relationships between SAR look direction, incident angle, target object platform altitude and object configuration relative to radar beam. It causes terrain slope of elevated targets, such as large pingos, facing towards the SAR sensor to appear compressed and brighter [55]. Even though some parts of older DTLBs contained features that exhibited higher NDVI and backscatter signals, such features were considerably less in number and, thus, had a small contribution to total mean backscatter and NDVI values of DTLBs, which was therefore relatively lower than younger DTLBs.

4.6.3. TSX backscatter and NDVI properties of modern and radiocarbon-dated DTLBs (0–10,000 years since drainage)

Analysis of TSX backscatter in the 27 August scene of the entire suite of DTLBs of known age (modern and radiocarbon-dated DTLBs) resulted in a significant logarithmic relation ($R^2 = 0.36$,

$p < 0.05$) between basin age and mean basin backscatter (Figure 4.3). However, a strong relationship could not be established ($R^2 < 0.2$, $p < 0.05$) between backscatter and basin age for the 09 September TerraSAR-X scene. A significant and even stronger logarithmic relation of $R^2 = 0.53$ ($p < 0.05$) was found between basin age and Landat-5 TM based NDVI (Figure 4.4). There was a decreasing trend in basin scale backscatter as basin age increased. A similar trend was observed in NDVI, but this relationship did not hold for the ancient basin (older than 5,000 years). NDVI value increased for the only ancient basin in our dataset.

The most notable successional transition was found between modern and young DTLBs. Modern DTLBs exhibited a generally higher variability in their spectral and backscatter properties compared to older DTLBs (Figures 4.5 and 4.6), indicative of their highly variable surface properties, while young basins were already characterized by tundra vegetation and drier and refrozen soils. Modern basins had a wide range of backscatter values between − 6.8 dB to − 3.2 dB. Several of them had low backscatter values similar to those of young and medium-aged DTLBs, even though they were characterized by different surface properties. We found that the basin productivity decreased significantly within 50–500 years after lake drainage. Modern DTLBs exhibited relatively high NDVI in the range of 0.32 to 0.52, compared to NDVI for radiocarbon-dated DTLBs that ranged from 0.27 to 0.47. We noticed that the rate of basin floor modification was much slower when basins reached medium age, as also reflected from their backscatter and NDVI values that did not vary much after this point. The characteristics of drained basins are illustrated in Figure 4.7 and summarized in Table 4.2.

4.7. Discussion

4.7.1. Uncertainties

Several components in this study are associated with uncertainties, though a detailed quantification of these uncertainties remains difficult due to a lack of appropriate data for comparison at this point. First, the remote sensing data represents, like in any other remote sensing study, a snapshot in time that reflects specific environmental conditions on the ground. Comparison with climate data from the Kotzebue climate station for the times of image acquisition indicated that the images were not taken in or directly after periods of unusual weather events and the image data seems generally representative for the observation periods.

Second, NDVI and backscatter may be scale-dependent, and a comparison between these parameters should ideally be done at the same pixel resolution. In our case, no suitable high-resolution data was available for the time of the TSX acquisitions, and we therefore chose Landsat data for NDVI closest to the TSX acquisition date. Though the Landsat data is from earlier in the growing season than our TSX images, the present general patterns of NDVI still provide a valuable insight into basin-wide vegetation distribution and phenology that are useful for interpreting TSX backscatter results.

Eventually, some uncertainty in this study arises from the relatively low number of samples for radiocarbon dated basins. In our study, several basins were dated by radiocarbon dating of basal terrestrial peat in a single core from a central portion of the basin [10]. These locations were considered to be representative for the entire basin based on aerial image and field analyses. Arguably, there may be heterogeneity in drained lake basins based on geological and hydrological history that also could affect the timing of peat accumulation. Only cost-intensive, additional radiocarbon dating could provide detailed insights in these particular uncertainties. However, radiocarbon basal peat dates of overlapping neighboring basins indicate that the method is suitable, as the ages of these basins were generally in agreement with their geomorphological position towards each other. Jones et al. [10] and Hinkel et al. [12] address some of the issues related to basin sampling and basin age determination in more detail. Due to a relatively small available sample size of basins with known age, we also were not able to explore general differences between upland and lowland basins. While lowland basins have low topography and a lower drainage gradient, upland basins usually have a steeper drainage gradient, likely resulting in different succession patterns of post-drainage soil moisture, vegetation and permafrost development. We suggest that some of the heterogeneity in our dataset results from mixing these two types of basins.

4.7.2. Surface characteristics of modern DTLBs (0–50 years since drainage)

Based on our results, a 50-year time period after lake drainage appears too short to observe a predictable succession of vegetation and changes in soil properties using a space-for-time substitution approach with TSX backscatter and Landsat-based NDVI data of DTLBs with varying ages. However, this may not exclude the presence of clear relationships due to successional changes within individual basins that could be observed with a time series of

imagery. Local variations of the draining process related to drainage gradient, basin size and watershed size likely played a significant role in determining successional stage and hydrologic regimes of modern basins. For enhanced differentiation, the application of a high resolution Digital Elevation Model (DEM) would be useful to stratify basins based on their hydro-geomorphic regime [11] and allow an enhanced evaluation of the relationship between basin age and backscatter or spectral data on different basin subsets. However, due to a lack of fine resolution DEM for our study region, we could not follow this approach. Similarly, due to variation in surface drainage within a basin floor, the basin floor was characterized by diverse soil moisture and vegetation composition. This resulted in mixed and spatially complex backscatter and spectral pixel-signal that largely prevented a solid discrimination of successional stages of modern DTLBs after lake drainage. Eisner and Peterson [19] and Hinkel et al. [12] have also observed this variability within one basin as an inherent source of error in age classification of basins on the Barrow Peninsula, North Alaska.

The high backscatter of sparsely distributed emergent vegetation and floating vegetation mats in our study is likely due to deeper penetration of the shorter wavelength X-band radiation through a vegetation canopy, which then results in the double bounce reflection from the water and vegetation [56]. In our study, incidence angles of all the TSX scenes were very close to each other, ranging from 28.8° to 35.3°. A smaller incidence angle shortens the path through canopy and reduces the canopy attenuation on the radar signal, allowing it to penetrate deeper [57]. Töyrä et al. [58] showed similar results for radar backscattering from flooded willow, grasses and sedges in the Peace-Athabasca Delta, Canada.

For very young DTLBs (younger than five years old) with shallow water and an early assemblage of densely populated and productive graminoid vegetation, the low backscatter value can be explained by a decreasing contribution of a signal from the wet soil surface and the increasing biomass [59]. In this case, even at a low incidence angle, the shorter wavelength of X-band cannot penetrate through the denser canopy layer and detect the background. The interaction of canopy and radiation takes place within the volume of the vegetation canopy that is composed of multiple scatterers with different sizes and orientation [56]. This results in volume and multiple scattering with low return signal. Similar radiation-canopy interaction is observed in parts of other modern DTLBs, which have dense graminoid cover.

For some dry basin surfaces with moss and lichen cover or exposed ground, likely a result of higher elevated surfaces of the former lake bottom exposed very early in the drainage process, it is possible that X-band could have penetrated the upper thin vegetation layer covering the basin floor [40,60]. Therefore, the moisture of the underlying soil could have contributed more to the total backscatter from dry basin surfaces. Aubert et al. [61] in their analysis of TSX data sensitivity to bare soil moisture and roughness have shown that the sensitivity of the radar signal to soil moisture for TSX is higher at smaller incidence angles similar to the ones we have used in our study. In contrast, it is less sensitive to soil roughness. Past studies have documented that soil with low moisture content exhibits lower backscatter and that backscatter increases linearly with increasing moisture for soil with volumetric soil moisture contents between 0 % and approximately 35–40 %, after which the backscatter coefficient stays constant and then decreases with increasing soil moisture [39,61].

The moderate resolution Landsat data was generally useful to derive mean basin NDVI. Due to a lack of suitable high resolution multispectral optical remote sensing images overlapping with our SAR dataset from the growing season of the year 2009, we could not perform detailed vegetation pattern analysis in basins, particularly in areas influenced by spectral mixing due to partly submerged vegetation in water or small patches of vegetation mats interspersed with patches of open water.

4.7.3. Surface characteristics of modern and radiocarbon-dated DTLBs (0-10,000 years since drainage)

We attribute the logarithmic relationships of basin age with mean basin backscatter and mean basin NDVI in the summer season to post-drainage change in vegetation, soil formation and peat accumulation, and permafrost aggradation. Our analysis also showed seasonal differences in backscatter between the 27 August and 9 September scenes and the lack of a clear relationship in the September scene backscatter with basin age. A plausible explanation could be that seasonal changes in vegetation phenology and soil moisture properties of basin floors obscure the link between backscatter and basin age later in the fall. This suggests that the time of image acquisition should be taken into consideration when investigating post-drainage succession patterns of thermokarst basins using radar datasets. Reidel et al. [52] have already demonstrated variations in NDVI throughout the season and its implications for estimating plant

productivity more accurately for the tundra ecosystem. To fully understand the seasonal behavior of basin backscatter and the basin age relationship, further analysis of multi-temporal data is required.

Diverse surface properties among modern DTLBs, as well as within a modern drained basin, affected the SAR signal in separating modern basins from young and medium-aged basins. This is because of complex and non-linear interaction between radar backscatter and diverse biophysical parameters [41,57] that dominated basin floors during early successional stages after lake drainage. Since modern DTLBs exhibited relatively high NDVI due to mostly dense graminoid vegetation compared to older DTLBs, NDVI was a good indicator of basin age over a period of 0–10,000 years. However, TSX data performed much better when used to discriminate basins older than modern basins (50–10,000 years BP), likely due to the better sensitivity of soil moisture. This shows that the usefulness of NDVI for discrimination of DTLB successional stage diminishes when the rate of vegetation succession slows down in older and less productive basins.

A decreasing trend in basin backscatter with increasing basin age can be explained by the decrease in soil moisture and presence of patterned ground with the increasing number of small ponded low-center polygons in medium-aged, old and ancient DTLBs. It is likely that the reduced specular property resulted in a lower backscatter signal as soil moisture decreased [57] with increased basin age. In the case of some older radiocarbon-dated DTLBs that were dominated by fully developed polygonal networks with a significant number of small ponds, ponded polygons contributed the most to the overall very low backscatter value. Even though a water mask was created to exclude backscatter of larger water bodies from our study, microscale ice wedge polygonal ponds below TSX image resolution had an impact on backscatter properties. However, we found vegetation growing in some inundated areas exhibited high backscatter due to the double bounce effect of the radar signal [56,58]. Despite an overall decrease in productivity of old basins, the waterlogged conditions in low-center ponds in older DTLBs could have created preferential conditions for growth of productive wetland plant communities [32].

The relationship of decreasing NDVI with increasing basin age agrees with findings by Hinkel et al. [12], Zona et al. [32] and Zulueta et al. [36] from their study on DTLBs on the

Arctic Coastal Plain of Alaska. Jones et al. [10] also highlighted a significant relation between Landsat-derived NDVI and basin peat thickness on the northern Seward Peninsula, Alaska. They observed a decrease in basin scale NDVI as basin peat depth increased. Decreasing basin productivity, as indicated by decreasing NDVI, is caused by a lack of nutrient availability in older DTLBs as nutrients become sequestered in the peat as the basin ages [32]. It was demonstrated that the highest rate of peat accumulation on the northern Seward Peninsula occurs in young DTLBs [10]. Also, permafrost aggradation and ground ice formation due to thermal insulation by accumulating peat is likely to have an impact on basin vegetation properties, further favoring less productive tundra moss and sedge species over highly productive wetland grass and sedge species. However, the relationship of ancient basin age with NDVI signal is only based on one sample and, therefore, adds an uncertainty in our analysis, whether there are specific biophysical reasons for a repeated increase in NDVI in ancient basins or whether the single data point for ancient basins in our dataset is an outlier. The cause of increased NDVI in ancient basins requires further investigation.

In general, the rate of ice-wedge polygonization we observed for DTLBs in Seward Peninsula is slower than that observed by Hinkel et al. [12] in their study on DTLBs for the Barrow Peninsula, Alaska. They noticed a high rate of polygonization during the first 500 years of basin history. This difference could be related to the relatively warmer climatic conditions of the northern Seward Peninsula compared to the cold climate on the Barrow Peninsula that could restrict regular ice-wedge formation in our study area. The depth of the lake occupying the basin before drainage also makes an important contribution to ice volume in drained basins. Portions of ice-wedges may remain under shallow lakes that freeze to the bottom during winter and do not form deep taliks. Therefore, the presence of fully developed ice wedge polygonal networks in some younger radiocarbon-dated basins in our study could be a result of reactivation of old ice wedge networks when exposed to cold temperatures. Further analysis of geomorphic characteristics of these basins can help to better evaluate ice-wedge formation [21].

4.7.4. Discussion of long-term DTLB development

Several authors have described changes in vegetation composition and structure, changes in soil moisture, peat accumulation, permafrost aggradation and development of ponded low-centered polygons in DTLBs [10,12,19,29,32]. The results from our remote sensing study of DTLBs on

the northern Seward Peninsula agree with the general findings from the previous studies on DTLBs on the Arctic Coastal Plain of Alaska [12,19,29,32,36]. There is a post-drainage pattern of vegetation succession and change in surface soil properties as DTLBs age. However, our observation is not consistent with the classical concept of a "thaw lake cycle" that assumes that a thermokarst lake goes through a complete cycle from lake to drained basin and back to a lake in a specific time period [8,34]. For the northern Seward Peninsula, there is no absolute frequency for a thermokarst lake cycle [10]. In addition to time since drainage, other factors determine the successional stage of a basin and formation of a new lake, including climate variability, basin topography, hydrologic framework, geomorphology and history of lake and basin evolution. A recent study on thermokarst lake dynamics in the northern Seward Peninsula that used multi-temporal satellite and aerial images from 1950 to 2007 demonstrated that small new lakes may reform just decades after drainage of large shallow thermokarst lakes, while remnant lakes from partially drained lake basins often start expanding into neighboring DTLBs or uplands due to shore thermal erosion [27]. The study found that the increase in lake numbers between 1950 and 2007 can be attributed to the partial drainage of larger thermokarst lakes and the formation of multiple smaller remnant ponds and lakes. In our study, the appearance of ponding in some radiocarbon-dated basins and the absence of distinct signs of new lake formation in others suggest that the formation of a new lake in an old drained basin is closely tied to the amount of ice content, local topography, hydrological regime, the rate of vegetation succession and polygonal development [12].

There is a complex relationship between vegetation, topography, hydrology, geomorphic and climatic variables that determines the rate of lake expansion, lake drainage [62,63], as well as permafrost aggradation following lake drainage [33]. This consequently affects the thermokarst lake cycle frequency. Jorgenson and Shur [21] proposed a new conceptual model for the evolution of thermokarst lakes and DTLBs, taking into account the influence of basin topography, soil stratigraphy and ground ice dynamics for the development of the thermokarst lake cycle. However, this model for the North Slope of Alaska does not reflect the strong lateral dynamics we observe on the Seward Peninsula with multiple, mostly partially overlapping lake and basin generations. Future research should be directed towards improving knowledge on

factors influencing lake drainage and post-drainage successional patterns of DTLBs and how they interact.

4.8. Conclusion

We used high-resolution TerraSAR-X (TSX) images in combination with Landsat-5 TM-based Normalized Difference Vegetation Index (NDVI) to explore the application of SAR data for characterizing post-drainage succession in thermokarst lake basins on the Seward Peninsula, Alaska. Backscatter and NDVI properties of 60 known drained thermokarst lake basins (DTLBs) that drained partially or completely since 1950 (modern DTLBs), as well as the properties of 14 DTLBs radiocarbon-dated to be up to 10,000 years BP (young, medium-aged, old and ancient DTLBs) were investigated in three subsets: (1) 0–50 years since drainage, modern basins; (2) 50–10,000 years since drainage, radiocarbon-dated basins; and (3) 0–10,000 years since drainage, modern and radiocarbon-dated basins. Our findings indicate that TSX backscatter and Landsat NDVI can trace long-term (0–10,000 years) succession dynamics of DTLBs related to vegetation, soil and permafrost changes. The logarithmic relationships of basin age with mean basin backscatter and with mean basin NDVI resulted in $R^2 = 0.36$ ($p < 0.05$) and $R^2 = 0.53$ ($p < 0.05$), respectively. For the 50–10,000 year period, TSX backscatter data outperformed NDVI in discriminating basin successional stage, likely due to its ability to partially detect soil moisture conditions. We here found $R^2 = 0.58$ ($p < 0.05$) between radiocarbon-dated basin age and mean basin backscatter. Overall, there was a decreasing trend in both backscatter and NDVI as basin age increased as a result of post-drainage changes in basin surface properties that include decreasing vegetation productivity after an initial productivity spike, decreasing soil moisture, renewed ice-wedge growth and development of either ponded or dry polygonal networks. However, in modern basins, the 50 year time scale was insufficient to find a clear relationship of basin age with TSX backscatter and NDVI. We noticed that not only time since drainage, but a combination of local environmental factors highly influences the successional stages of a basin. This was more prominent in modern basins. Over time with continuing basin succession and stabilization of basin floor, variability in basin surface properties decreased within a basin, as well as among basins of an age class. Since DTLB dynamics likely affect landscape-scale carbon fluxes in high northern latitudes, it is necessary to better understand the spatial and temporal distribution of thermokarst lakes and DTLBs across large regions. Our study highlights the

excellent opportunity to use and combine various remote sensing tools for better estimation of the areal extent of high latitude carbon pools and sources of greenhouse gases associated with thermokarst dynamics. Future research should be directed toward utilizing high-resolution topographic data with SAR data, including short and long wavelengths, as well as optical remote sensing data, to better understand the processes driving the evolution of basins. Additionally, multi-temporal analysis of SAR data for basins would increase our understanding of seasonal soil moisture dynamics and their influence on post-drainage vegetation and soil succession.

4.9. Acknowledgements

We acknowledge support from NASA Carbon Cycle Sciences grant NNX08AJ37G, NSF grant OPP-0732735, and the Western Alaska LCC. We thank the German Space Agency DLR for providing TerraSAR-X images through IPY grant LAN0351. We thank the US National Park Service for permitting our research in Bering Land Bridge National preserve and providing Ikonos imagery. We thank four anonymous reviewers and two external USGS reviewers (L. Liu, J. Rover) for helpful comments on the manuscript. Any use of trade, product or firm names is for descriptive purposes only and does not imply endorsement by the US Government.

4.10. Figures

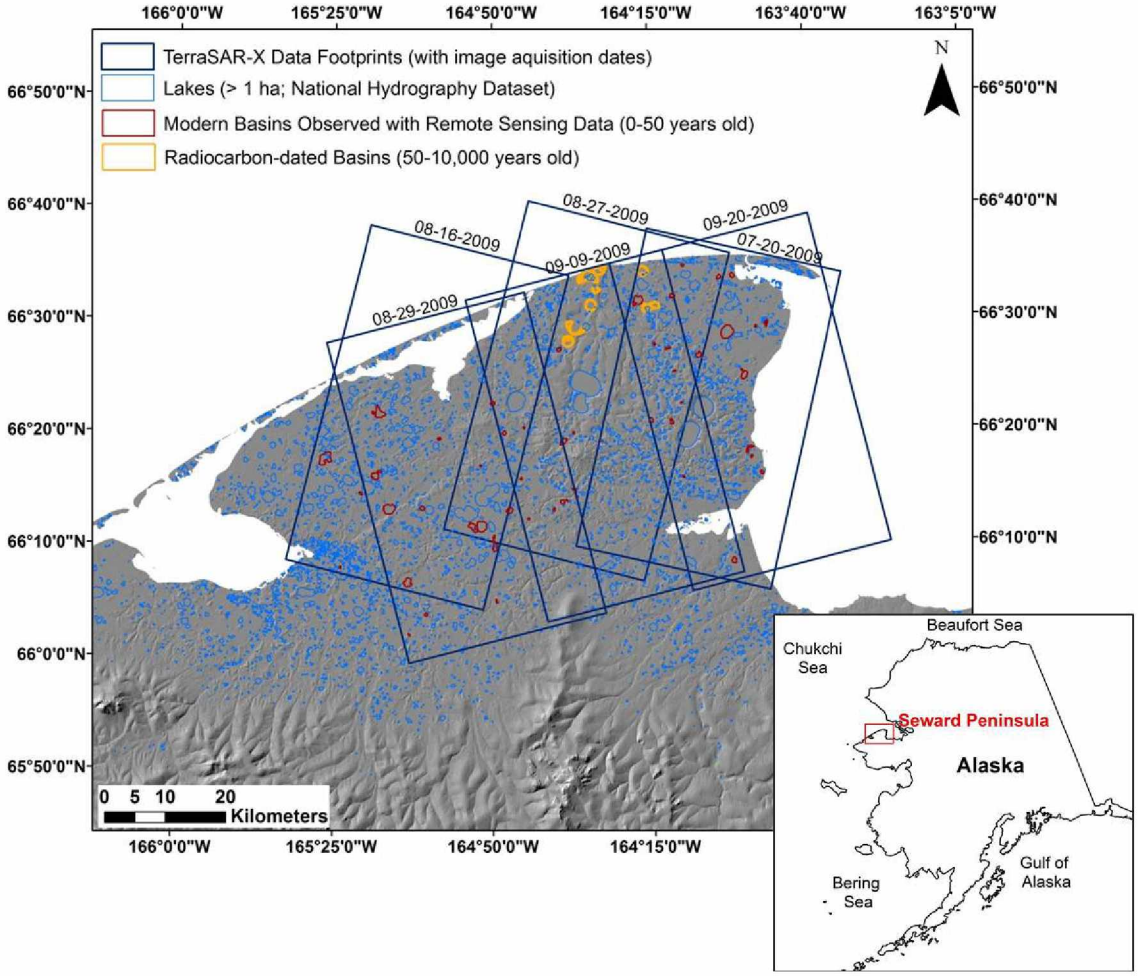

Figure 4.1. Digital Elevation Model (DEM) base map of the Seward Peninsula showing the location of lakes (>1 ha) mapped in National Hydrography Dataset (NHD) and DTLBs that drained (>90% of surface area loss) 0–50 years ago (based on times series analysis of aerial and satellite images from 1950 to 2010 [43]) and 50–10,000 years BP (based on radiocarbon dating [10]). The footprints of six TerraSAR-X scenes used in analysis are outlined in blue with their respective acquisition dates.

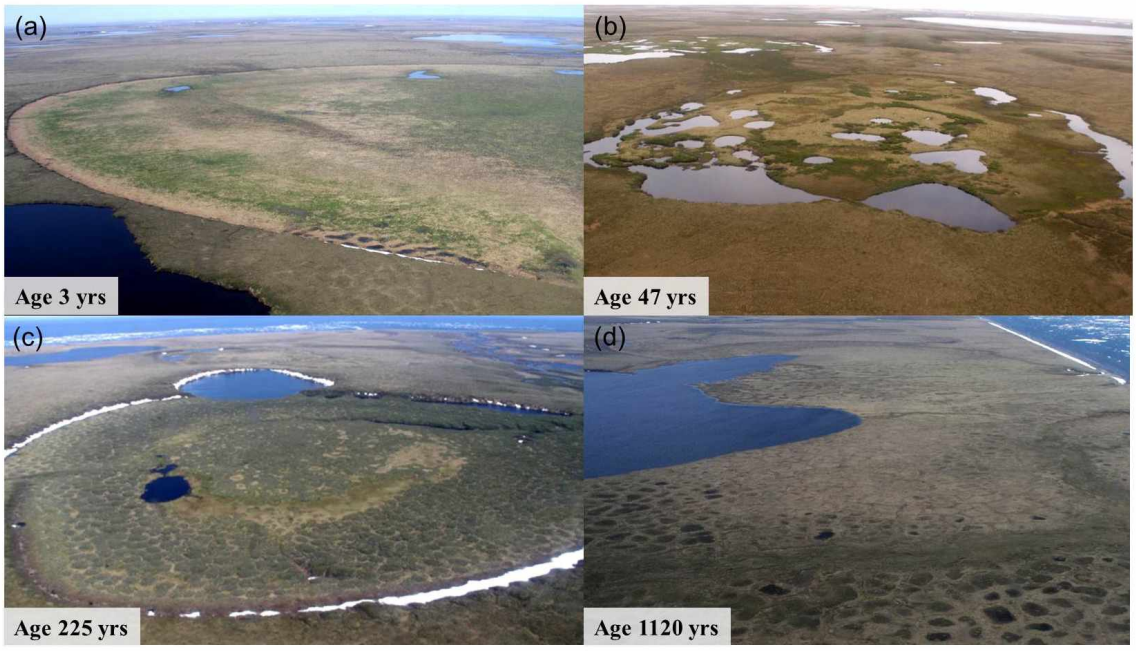

Figure 4.2. Oblique aerial photographs of DTLBs located on the northern Seward Peninsula at various stages after drainage showing evolution of basin floor characteristics. Photos were collected during field visits in late June 2010 and 2011. **(a)** Early assemblage of highly productive grass vegetation emerging from very shallow water in recently drained modern basin. As the growing season progresses, the graminoid vegetation grows to 50–130 cm tall, densely covering the basin floor. **(b)** A typical characteristic of modern shallow basins after a few decades after drainage is that some parts of the basin get drier and some remain inundated, depending on local topography and hydrological characteristics. A mixed vegetation community is observed in such basin types. **(c)** Dry basin floor with willows growing in a young basin. **(d)** Polygonization and ponding in a medium age basin.

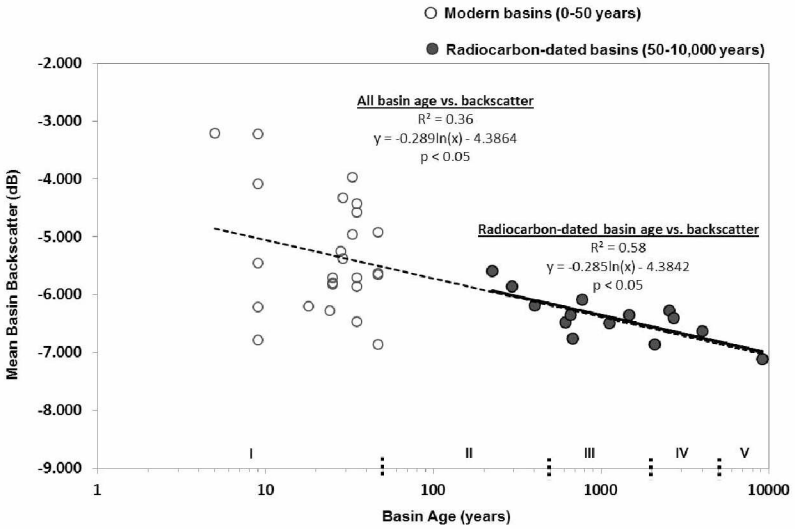

Figure 4.3. Plot of mean basin backscatter observed on 27 August 2009 against basin age showing a logarithmic relationship for the period of 0–10,000 years and 50–10,000 years. Basin age class is shown as: I. Modern basins; II. Young basins; III. Medium age basins; IV. Old basins; and V. Ancient basins.

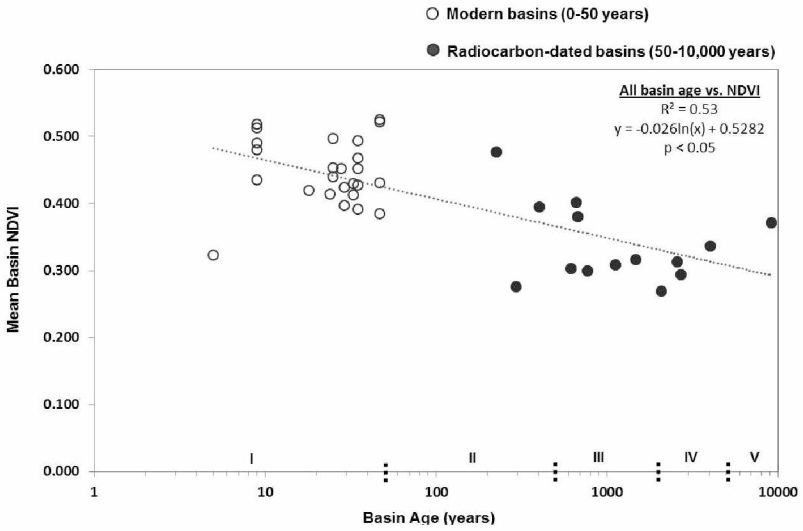

Figure 4.4. Plot of mean basin NDVI observed on 13 July 2009 against basin age showing a logarithmic relationship for the period of 0–10,000 years. Basin age class is shown as: I. Modern basins; II. Young basins; III. Medium age basins; IV. Old basins; and V. Ancient basins.

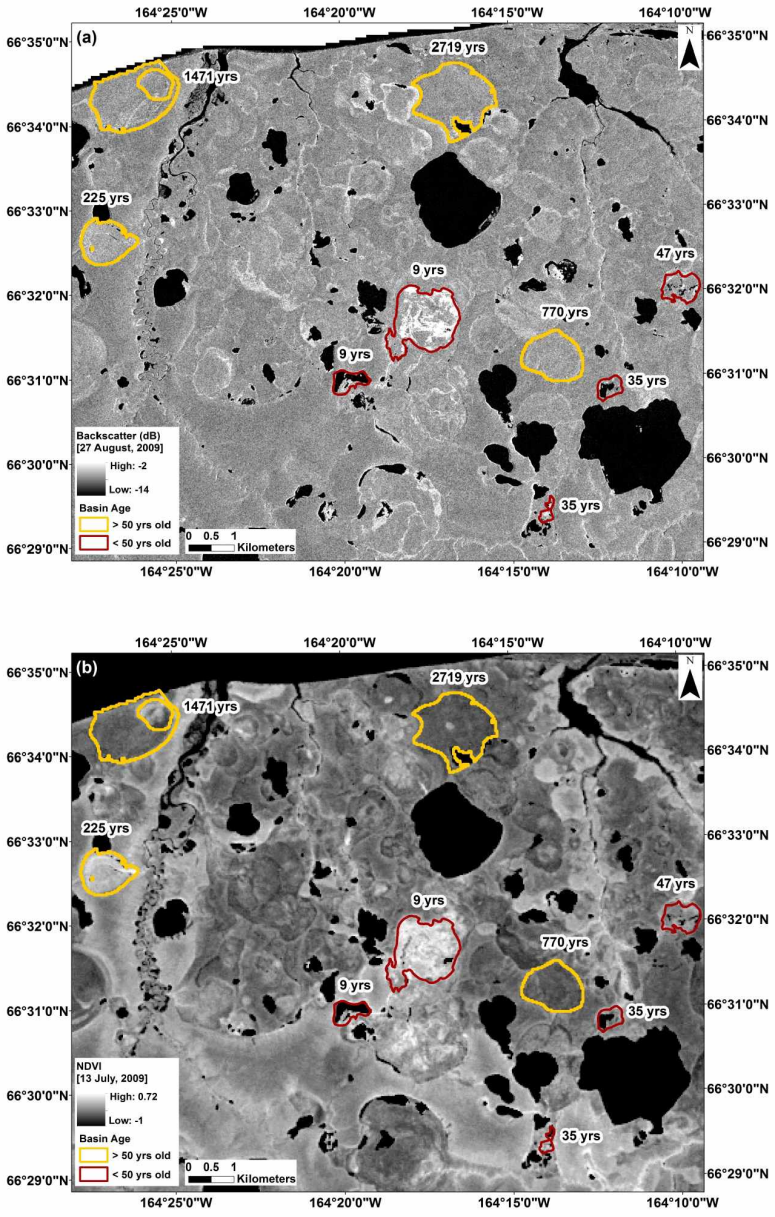

Figure 4.5. Backscatter and NDVI properties of DTLBs at various stages in a subset of the study area on the northern Seward Peninsula as observed in: (**a**) TerraSAR-X image (3 m spatial resolution) on 27 August 2009; and (**b**) Landsat-5 TM based NDVI (30 m spatial resolution) on 13 July 2009.

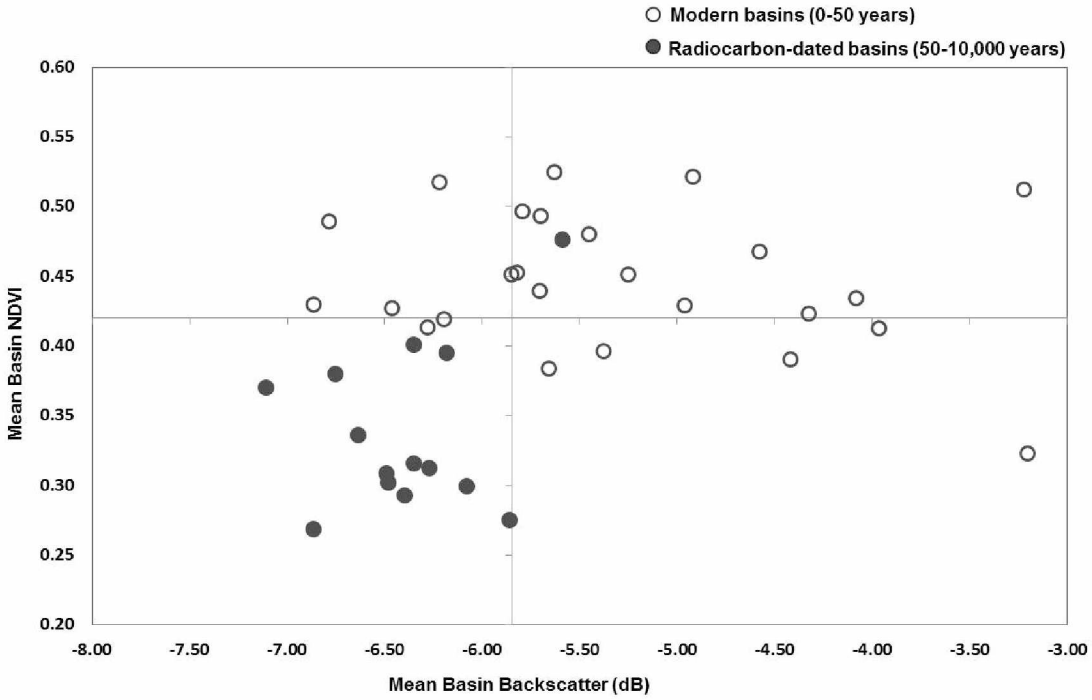

Figure 4.6. Distribution of backscatter and NDVI values of DTLBs showing the differences in backscatter and spectral properties of modern and radiocarbon-dated basins. The axes intersect at the median of each parameter.

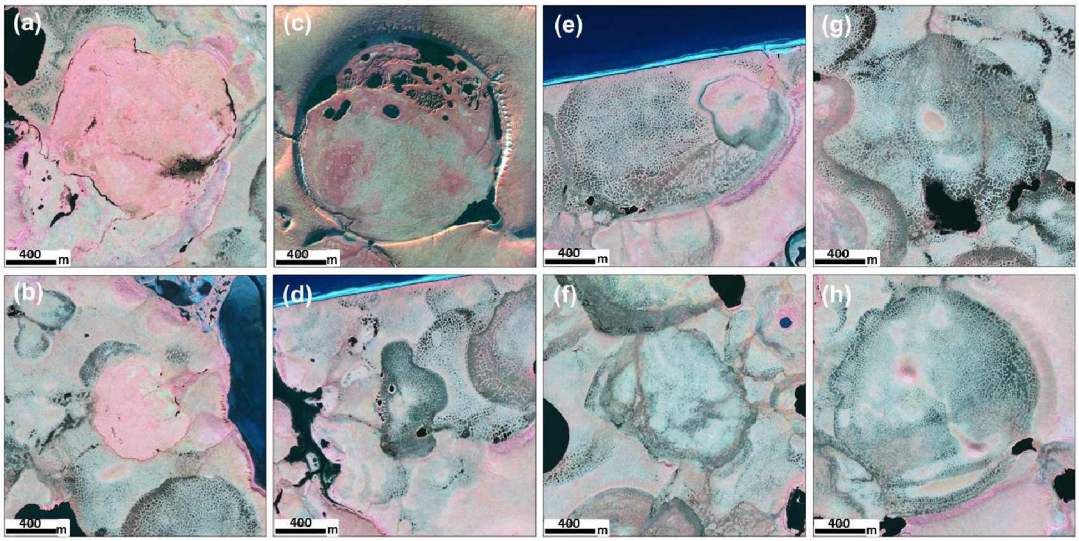

Figure 4.7. DTLB of different age classes located in the northern Seward Peninsula (Modern: (**a**) 9 yrs old, (**b**) 29 yrs old; Young: (**c**) 403 ± 55 cal·yr·BP, (**d**) 294 ± 15 cal·yr·BP; Medium: (**e**) 1471 ± 60 cal·yr·BP, (**f**) 770 ± 35 cal·yr·BP; Old: (**g**) 2719 ± 40 cal·yr·BP, (**h**) 2567 ± 80 cal·yr·BP; Modern basin ages from Grosse et al. [43] and radiocarbon dates from Jones et al. [10]). All images show bands 4-3-2 (near-infrared, red, green) and are in same scale. Image C is from Quickbird © DigitalGlobe; all others are from IKONOS © GeoEye. Vegetation appears in shades of pink with darker color representing high biomass. Water appears dark bluish or black, and bare or sparsely vegetated soil appears in shades of light blue or grey.

4.11. Tables

Table 4.1. Satellite images used in the study.

Scenes	Acquisition Date	Spatial Resolution	Incidence Angle	Orbit Direction	Polarization
TerraSAR-X 1	07/20/2009	3 m	35.3°	Descending	HH
TerraSAR-X 2	08/16/2009	3 m	31.0°	Descending	HH
TerraSAR-X 3	08/27/2009	3 m	28.8°	Descending	HH
TerraSAR-X 4	08/29/2009	3 m	31.1°	Ascending	HH
TerraSAR-X 5	09/09/2009	3 m	33.2°	Ascending	HH
TerraSAR-X 6	09/20/2009	3 m	35.3°	Ascending	HH
Landsat-5 TM	07/13/2009	30 m	-	-	-

Table 4.2 Characteristics of basins of different age on the northern Seward Peninsula

Basin Class*	Modern (0–50 years)	Young (50–500 years)	Medium (500–2,000 years)	Old (2,000–5,000 years)	Ancient (>5,000 years)
Number of basins studied	60	3	6	4	1
Mean late summer (27 Aug) TSX backscatter (dB)	−5.3 ± 0.99	−5.88 ± 0.24	-6.42 ± 0.20	−6.54 ± 0.23	−7.11
Mean mid-summer (13 Jul) NDVI	0.45 ± 0.05	0.38 ± 0.08	0.33 ± 0.04	0.30 ± 0.02	0.37
Vegetation	High average gross primary productivity with dominating plant species* *Calamagrostis canadensis, Dupontia fisherii, Carex aquatilis.*	Gradual decrease in productivity →		Low average gross primary productivity with dominating plant species* *Carex bigelowii, Eriophorum angustifolium* and *Sphagnum fuscum* , *Betula nana*, *Salix* sp., and prostrate ericaceous shrubs. However, low-centered polygonal ponds in older basins contain productive species such as *Carex aquatilis*.	
Permafrost aggradation	Lake sediment starts to refreeze after drainage over several years to decades as a result of exposed lake bottom.	Frost heave occurs due to refreezing of lake sediments and taliks and ground ice accumulation. Frost cracking occurs; in basins that only had very shallow lakes, not thawed-out ice wedge networks, may become reactivated.	Low-center ice-wedge polygonal networks are largely well developed.	Basins have very well developed low-center ice-wedge polygonal networks. Some basins have fully developed hydrostatic pingos. In some basins, ground ice is sufficient to allow development of new thermokarst ponds and expansion of small remnant lakes.	
Basin wetness	High soil moisture and standing water in most lowland basins, low soil moisture in upland basins where steeper topographic gradient allows better drainage.	Beginning development of polygonal networks creates micro-mosaic of wetter and drier areas in basins, polygonal ponds develop.	Polygonal ponds appear widely in low center polygons. Ponded polygons are more distinct in older medium aged basins (>1000 years).	Long-term frost heave, including pingo formation, results in drying of central basin areas. Some basins have increased number of polygonal and ice wedge through ponds, whereas basins with a steep topographic gradient become drier.	
Peat carbon stocks* (kg C m^{-2})	<10	11.8 ± 2.4	17.3 ± 7.8	34 ± 8.9	83.3

* Jones et al. [10]

4.12. References

1. Czudek, T.; Demek, J. Thermokarst in Siberia and its influence on the development of lowland relief. Quaternary Res. 1970, 1, 103–120.

2. Soloviev, P.A. Thermokarst phenomena and landforms due to frost heaving in central Yakutia. Biul. Peryglacjalny 1973, 23, 135–155.

3. Burn, C.R.; Smith, M.W. Development of thermokarst lakes during the Holocene at sites near Mayo, Yukon territory. Permafrost Periglac. Process. 1990, 1, 161–175.

4. Morgenstern, A.; Grosse, G.; Günther, F.; Fedorova, I.; Schirrmeister, L. Spatial analyses of thermokarst lakes and basins in Yedoma landscapes of the Lena Delta. Cryosphere 2011, 5, 849–867.

5. Grosse, G.; Jones, B.; Arp, C. Thermokarst Lakes, Drainage, and Drained Basins. In Treatise in Geomorphology; Elsevier: New York, NY, USA, 2012; in press.

6. Livingstone, D.A.; Bryan, K.; Leahy, R.G. Effects of an arctic environment on the origin and development of fresh-water lakes. Limnol. Oceanogr. 1958, 3, 192–214.

7. Sellmann, P.V.; Brown, J.; Lewellen, R.I.; McKim, H.; Merry, C. The Classification and Geomorphic Implications of Thaw Lakes on the Arctic Coastal Plain, Alaska; US Army CRREL Research Report 344; US Army Cold Regions Research and Engineering Laboratory: Hanover, NH, USA, 1975; p. 21.

8. Hopkins, D.M.; Kidd, J.G. Thaw Lake Sediments and Sedimentary Environments. In Proceedings of the 5th International Permafrost Conference, Trondheim, Norway, 2–5 August 1988; pp. 790–795. 9.

9. Frohn, R.C.; Hinkel, K.M.; Eisner, W.R. Satellite remote sensing classification of thaw lakes and drained thaw lake basins on the North Slope of Alaska. Remote Sens. Environ. 2005, 97, 116–126.

10. Jones, M.C.; Grosse, G.; Jones, B.M.; Walter Anthony, K. Peat accumulation in drained thermokarst lake basins in continuous, ice-rich permafrost, northern Seward Peninsula, Alaska. J. Geophys. Res. 2012, 117, 1–16.

11. Wang, J.; Shen, Y.; Hinkel, K.M.; Lyons, E.A. Drained thaw lake basin recovery on the western Arctic Coastal Plain of Alaska using high resolution digital elevation models and remote sensing imagery. Remote Sens. Environ. 2012, 119, 325–336.

12. Hinkel, K.M.; Eisner, W.R.; Bockheim, J.G.; Nelson, F.E.; Peterson, K.M.; Dai, X. Spatial extent, age, and carbon stocks in drained thaw lake basins on Barrow Peninsula, Alaska. Arctic Antarct. Alpine Res. 2003, 35, 391–300.

13. Bockheim, J.G.; Hinkel, K.M.; Eisner, W.R.; Dai, X.Y. Carbon pools and accumulation rates in an age-series of soils in drained thaw-lake basins, Arctic Alaska. Soil Sci. Soc. Am. J. 2004, 68, 697–704.

14. Gorham, E. Northern peatlands: Role in the carbon cycle and probable responses to climatic warming. Ecol. Appl. 1991, 1, 182–195.

15. Walter, K.M.; Smith, L.C.; Chapin, F.S., III Methane bubbling from northern lakes: Present and future contributions to the global methane budget. Phil. Trans. R. Soc. Lond. B. 2007, 365, 1657–1676.

16. Zimov, S.A.; Davydov, S.P.; Zimova, G.M.; Davydova, A.I.; Schuur, E.A.G.; Dutta, K.; Chapin III, F.S. Permafrost carbon: Stock and decomposability of a globally significant carbon pool. Geophys. Res. Lett 2006, 33, L20502.

17. Schuur, E.A.G.; Bockheim, J.; Canadell, J.G.; Euskirchen, E.; Field, B.F.; Goryachkin, S.V.; Hagemann, S.; Kuhry, P.; Lafleur, P.M.; Lee, H.; et al. Vulnerability of permafrost carbon to climate change: Implications for the global carbon cycle. BioScience 2008, 58, 701–714.

18. Sitch, S.; McGuire, A.D.; Kimball, J.; Gedney, N.; Gamon, J.; Engstrom, R.; Wolf, A.; Zhuang, Q.; Clein, J.; McDonald, K.C. Assessing the carbon balance of circumpolar Arctic tundra using remote sensing and process modeling. Ecol. Appl. 2007, 17, 213–234.

19. Eisner, W.R.; Peterson, K.M. Pollen, Fungi and Algae as Age Indicators of Drained Lake Basins near Barrow, Alaska. In Proceedings of the 7th International Permafrost Conference, Yellowknife, NWT, Canada, 23–27 June 1998; Lewkowicz, A.G., Allard, M., Eds.; Centre d'études nordiques de l'Université Laval: Quebec, QC, Canada, 1998; pp. 790–795.

20. Yoshikawa, K.; Hinzman, L.D. Shrinking thermokarst ponds and groundwater dynamics in discontinuous permafrost near Council, Alaska. Permafrost Periglac. Process. 2003, 14, 151–160.

21. Jorgenson, M.T.; Shur, Y. Evolution of lakes and basins in northern Alaska and discussion of the thaw lake cycle. J. Geophys. Res. 2007, 112, 1–12.

22. Hopkins, D.M. Thaw lakes and thaw sinks in the Imuruk Lake area, Seward Peninsula, Alaska. J. Geol. 1949, 57, 119–131.

23. Carson, C.E.; Hussey, K.M. The oriented lakes of Arctic Alaska. J. Geol. 1962, 70, 417–439.

24. Billings, W.D.; Peterson, K.M. Vegetational change and ice wedge polygons through the thaw-lake cycle in Arctic Alaska. Arctic Alpine Res. 1980, 1, 413–432.

25. West, J.J.; Plug, L.J. Time-dependent morphology of thaw lakes and taliks in deep and shallow ground ice. J. Geophys. Res. 2008, 113, 1–14.

26. Kokelj, S.V.; Lantz, T.C.; Kanigan, J.; Smith, S.L.; Coutts, R. Origin and polycyclic behaviour of tundra thaw slumps, Mackenzie Delta region, Northwest Territories, Canada. Permafrost Periglac. Process. 2009, 20, 173–184.

27. Jones, B.; Grosse, G.; Arp, C.D.; Jones, M.C.; Walter Anthony, K.M.; Romanovsky, V.E. Modern thermokarst lake dynamics in the continuous permafrost zone, northern Seward Peninsula, Alaska. J. Geophys. Res.-Biogeosci. 2011, 116, G00M03.

28. Mackay, J.R. Catastrophic lake drainage, Tuktoyaktuk Peninsula area, District of Mackenzie. Curr. Res.-Bull. Geol. Surv. Can. 1988, 88–1D, 83–90.

29. Bliss, L.C.; Peterson, K.M. Arctic Ecosystems in a Changing Climate. In Plant Succession, Competition, and the Physiological Constraints of Species in the Arctic: An Ecophysiological Perspective; Chapin, F.S., III, Jefferies, R.L., Reynolds, J.F., Shaver, G.R., Svoboda, J., Chu, E.W., Eds.; Academic Press: San Diego, CA, USA, 1992; pp. 111–136.

30. Hinkel, K.M.; Frohn, R.C.; Nelson, F.E.; Einser, W.R.; Beck, R.A. Morphometric and spatial analysis of thaw lakes and drained thaw lake basins in the western Arctic Coastal Plain, Alaska. Permafrost Periglac. Process. 2005, 16, 327–341.

31. Ling, F.; Zhang, T.J. Modeling study of talik freeze-up and permafrost response under drained thaw lakes on the Alaskan Arctic Coastal Plain. J. Geophys. Res. 2004, 109, D01111.32.

32. Zona, D.; Oechel, W.C.; Peterson, K.M.; Clements, R.J.; Paw, U.K.T.; Ustin, S.L. Characterization of the carbon fluxes of a vegetated drained lake basin chronosequence on the Alaskan Arctic Coastal Plain. Global Change Biol. 2010, 16, 1870–1882.

33. Mackay, J.R.; Burn, C.R. The first 20 years (1978–1979 to 1998–1999) of ice-wedge growth at the Illisarvik experimental drained lake site, western Arctic coast, Canada. Can. J. Earth Sci. 2002, 39, 95–111.

34. Carson, C.E. Radiocarbon dating of lacustrine strands in Arctic Alaska. Arctic 1968, 21, 12–26.

35. Kessler, M.A.; Plug, L.; Walter Anthony, K. Simulating the decadal to millennial scale dynamics of morphology and sequestered carbon mobilization of two thermokarst lakes in northwest Alaska. J. Geophys. Res. 2012, 117, GM00M06.

36. Zulueta, R.C.; Oechel, W.C.; Loescher, H.W.; Lawrence, W.T.; Paw U, K.T. Aircraft-derived regional scale CO2 fluxes from vegetated drained thaw-lake basins and interstitial tundra on the Arctic Coastal Plain of Alaska. Global Change Biol. 2011, 17, 2781–2802.

37. Newton, R.W.; Rouse, J.W., Jr. Microwave radiometer measurements of soil moisture content. IEEE Trans. Antenn. Propag. 1980, 28, 680–686.

38. Shi, J.; Wang, J.; Hsu, A.Y.; O'Neill, P.E.; Engman, E.T. Estimation of bare surface soil moisture and surface roughness using L-band SAR image data. IEEE Trans. Geosci. Remote Sens. 1997, 35, 1254–1266.

39. Baghdadi, N.; Aubert, M.; Cerdan, O.; Franchistéguy, L.; Viel, C.; Martin, E.; Zribi, M.; Desprats, L.F. Operational mapping of soil moisture using Synthetic Aperture Radar data: Application to the Touch Basin (France). Sensors 2007, 7, 2458–2483.

40. Baghdadi, N.; Cresson, R.; Todoroff, P.; Moinet, S. Multitemporal observations of sugarcane by TerraSAR-X images. Sensors 2010, 10, 8899–8919.

41. Bindlish, R.; Barros, A.P. Parameterization of vegetation backscatter in radar-based, soil moisture estimation. Remote Sens. Environ. 2001, 76, 130–137.

42. Stow, D.; Daeschner, S.; Boynton, W.; Hope, A. Arctic tundra functional types by classification of single-date and AVHRR bi-weekly NDVI composite datasets. Int. J. Remote Sens. 2000, 21, 1773–1779. 43.

43. Grosse, G.; et al. Personal Communication. November 2012.

44. Arp, C.D.; Jones, B.M. Geography of Alaska Lake Districts: Identification, Description, and Analysis of Lake- Rich Regions of a Diverse and Dynamic State; US Geological Survey Scientific Investigations Report 2008–5215; USGS National Center: Reston, VA, USA, 2009; p. 40.

45. Charron, S.D. Surficial Mapping of the Cape Espenberg-Devil Mountain Region and Lake Core Analyses from North Killeak Lake, Bering Land Bridge National Preserve, Western Alaska. Master Thesis, University of Massachusetts, Amherst, MA, USA, 1995.

46. Smith, S.L.; Romanovsky, V.E.; Lewkowicz, A.G.; Burn, C.R.; Allard, M.; Clow, G.D.; Yoshikawa, K.; Throop, J. Thermal state of permafrost in North America: A contribution to the International Polar Year. Permafrost Periglac. Process. 2010, 21, 117–135.

47. Hopkins, D.M.; Karlstrom, T.N.V.; Black, R.; Pewe, T.L.; Fernold, A.T.; Muller, E.H. Permafrost and Ground Water in Alaska; US Geological Survey Professional Paper 264-F; USGS: Washington, DC, USA, 1955; p. 70.

48. Burn, C.R.; Kokelj, S.V. The environment and permafrost of the Mackenzie Delta area. Permafrost Periglac. Process. 2009, 20, 83–105.

49. Rupp, T.S.; Chapin, F.S., III; Starfield, A.M. Response of subarctic vegetation to transient climatic change on the Seward Peninsula in north-west Alaska. Global Change Biol. 2000, 6, 541–555.

50. Roth, A.; Hoffmann, J.; Esch, T. TerraSAR-X: How can High Resolution SAR Data Support the Observation of Urban Areas? In Proceedings of the ISPRS WG VII/1 "Human Settlements and Impact Analysis", 3rd International Symposium Remote Sensing and Data Fusion Over Urban Areas (URBAN 2005) and 5th International Symposium Remote Sensing of Urban Areas (URS 2005), Tempe, AZ, USA, 14–16 March 2005.

51. Stow, D.A.; Hope, A.; McGuire, D.; Verbyla, D.; Gamon, J.; Huemmrich, F.; Houston, S.; Racine, C.; Sturm, M.; Tape, K.; et al. Remote sensing of vegetation and land-cover change in Arctic tundra ecosystems. Remote Sens. Environ. 2004, 89, 281–308.

52. Riedel, S.M.; Epstein, H.E.; Walker, D.A. Biotic controls over spectral reflectance of arctic tundra vegetation. Int. J. Remote Sens. 2005, 26, 2391–2405.

53. Tucker, C.J. Red and photographic infrared linear combinations for monitoring vegetation. Remote Sens. Environ. 1979, 8, 127–150.

54. Parsekian, A.D.; Jones, B.M.; Jones, M.C.; Grosse, G.; Walter Anthony, K.M.; Slater, L. Geometry of floating vegetation mats on the expanding margins of thermokarst lakes, Northern Seward Peninsula, Alaska, USA. Earth Surf. Process. Landf. 2011, 36, 1889–1897.

55. Li, S. Summer environmental mapping potential of a large-scale ERS-1 SAR mosaic of the state of Alaska. Int. J. Remote Sens. 1999, 20, 387–401. 56.

56. Costa, M.P.F.; Niemann, O.; Novo, E.; Ahern, F. Biophysical properties and mapping of aquatic vegetation during the hydrological cycle of the Amazon floodplain using JERS-1 and Radarsat. Int. J. Remote Sens. 2002, 23, 1401–1426.

57. Wang, Y.; Hess, L.L.; Filoso, S.; Melack, J.M. Understanding the radar backscattering from flooded and non-flooded Amazonian Forests: Results from canopy backscatter modeling. Remote Sens. Environ. 1995, 54, 324–332.

58. Töyrä, J.; Pietroniro, A.; Lawrence, W.M. Multisensor hydrologic assessment of a freshwater wetland. Remote Sens. Environ. 2001, 75, 162–173.

59. Svoray, T.; Shoshany, M.; Curran, P.J.; Foody, G.M.; Perevolotsky, A. Relationship between green leaf biomass volumetric density and ERS-2 SAR backscatter of four vegetation formations in the semi-arid zone of Israel. Int. J. Remote Sens. 2001, 22, 1601–1607.

60. Baghdadi, N.; Camus, P.; Beaugendre, N.; Issa, O.M.; Zribi, M.; Desprats, J.F.; Rajot, J.L.; Abdallah, C.; Sannier, C. Estimating surface soil moisture from TerraSAR-X data over two small catchments in the Sahelian Part of Western Niger. Remote Sens. 2011, 3, 1266–1283.

61. Aubert, M.; Baghdadi, N.; Zribi, M.; Douaoui, A.; Loumagne, C.; Baup, F.; Hajj, M.E.; Garrigues, S. Analysis of TerraSAR-X data sensitivity to bare soil moisture, roughness, composition and soil crust. Remote Sens. Environ. 2011, 115, 1801–1810.

62. Brewer, M.C.; Carter, L.D.; Glenn, R. Sudden Drainage of a Thaw Lake on the Alaskan Arctic Coastal Plain. In Proceedings of Sixth International Conference on Permafrost, Beijing, China, 5–9 July 1993; South China University of Technology Press: Guangzhou, China, 1993; Volume 1, pp. 48–53.

63. Marsh, P.; Russell, M.; Pohl, S.; Haywood, H.; Onclin, C. Changes in thaw lake drainage in the western Canadian Arctic from 1950 to 2000. Hydrol. Process. 2009, 23, 145–158.

Chapter 5. Landsat-based lake distribution and changes in western Alaska between 1972 and 2014[4]

5.1. Abstract

Lakes are an important landscape and ecosystem component in the high northern latitudes. In this study, we utilized Landsat MSS and OLI images from the 1970s and 2014 to assess broad-scale distribution and changes of lakes larger than 1 ha in 6 major lake-rich areas across various permafrost zones (continuous, discontinuous, sporadic, and isolated extent) located in western Alaska. The lake-rich regions included Beringia, Baldwin Peninsula, Kobuk Delta, Selawik, Central Seward Peninsula, and Yukon-Kuskokwim Delta, covering a total area of 68,830 km^2. For three study regions (Baldwin Peninsula, Kobuk Delta, and Yukon-Kuskokwim Delta) an increase in total lake area by less than 4% was observed, while the other three regions (Beringia, Central Seward Peninsula, and Selawik) showed lake area decrease ranging between ~ 4-15%. The study shows that despite differences in net lake area change among regions, drainage of mainly large lakes is widespread in the western Alaska study region. Not surprisingly, partial drainage of large lakes (>10 ha) created numerous remnant lakes and ponds of <10 ha and hence, the total number of lakes increased in all regions by 2.2-27.1%. We found that lake drainage dominated the non-continuous permafrost zones in all study regions. In contrast, areas of continuous permafrost zones showed both trends of lake area expansion and shrinkage accompanied by major lake drainage events that led to a regional lake area loss in the continuous permafrost zone. In general, the observations indicate that both lake expansion and drainage are phenomenon ongoing in parallel in western Alaska, which may offset each other or shift a regional lake change pattern towards a certain direction. The identified regional trends suggest that widespread lake area loss is already happening at a significant pace in western Alaska. As climate gets warmer and permafrost continues to thaw, increased numbers of drainage events in this region are expected. Therefore, assessment of lake area change in high northern latitudes

[4]Lindgren, P. R., Grosse, G., Romanov sky, V. E., Farquharson., L. M., Landsat-based lake distribution and changes in western Alaska between 1972 and 2014, *In preparation for Journal of Hydrology.*

needs to be continued to quantify the biogeochemical and ecological feedbacks in a warming climate as well as to assist in future planning and decision-making for land and resource management issues.

5.2. Introduction

Permafrost, perennially frozen ground that remains at or below 0 ^{o} C for two or more years, is an important part of the cryosphere and is widely distributed in the high northern latitudes (Zhang et al., 2008). The occurrence of permafrost with its characteristics as a subsurface water barrier has significant impacts on the distribution of lakes and allows lakes to occur in high abundance in the permafrost regions (Smith et al., 2007; Grosse et al., 2013).

Climate warming is pronounced in the Arctic and Subarctic (Hinzman et al., 2005). Consequently, permafrost temperatures have increased throughout the region particularly since the last two to three decades (Osterkamp and Romanovsky, 1999; Romanovsky et al., 2010; Smith et al., 2010). Due to permafrost degradation, in some areas more lakes are developing while in some places lakes are draining more rapidly (Smith et al., 2005; Yoshikawa and Hinzman, 2003; Jones et al., 2011; Roach et al., 2013). Temporal and spatial heterogeneity in lake area change also indicates regional and temporal variation likely related to climate and environment (Smith et al., 2005; Riordan et al., 2006; Chen et al., 2014).

In the northern high latitudes, lakes are important ecosystem components forming a complex and dynamic landscape sometimes with repeated cycles of lake formation and drainage (Frohn et al., 2005; Jorgenson and Shur, 2007; Arp and Jones, 2009; Jones et al., 2012). Their dynamics and evolution at the landscape level have important implications for carbon budgets in permafrost regions (Walter et al., 2007a), hydrologic change that accompanies permafrost degradation (Rowland et al., 2011), and both aquatic and terrestrial habitat character and distribution (Jorgenson et al., 2010; Clark et al., 2010). They are important resources to indigenous communities as these lakes provide fresh drinking water as well as supporting subsistence hunting and fishing (Eisner et al., 2009). Lakes and ponds have also been used as a source of fresh water for industrial applications, such as ice road construction (Alessa et al., 2008; Jones et al., 2009). These factors combined with a projected air temperature increase (IPCC, 2007) in the coming century has led to increasing interest among scientists as well as land, wildlife and resource managers in data about the spatial distribution of lakes in permafrost

regions, how lake area is changing, and how lakes will respond to projected climate change. Such information is important to assess future hydrological characteristics of the region, feedbacks to climate change associated with the regional and global carbon cycle, and wildlife habitat changes, as well as to assess stability of water resources for the indigenous community and for industrial uses.

In Alaska, lakes are abundant in large portions of the Arctic Coastal Plain, the Arctic Foothills, North Western Alaska, Yukon-Kuskokwim Delta region, Interior Alaska, and the Alaskan Peninsula (Livingstone et al., 1958; Jorgenson and Osterkamp, 2005; Arp and Jones, 2009; Roach et al., 2011; Hinkel et al., 2012; Chen et al., 2014). Arp and Jones (2009) have identified 20 key lake districts distributed across these regions based on the U.S. Geological Survey National Hydrography Dataset (NHD) of lakes greater than 1 ha originally derived from topographic maps that are based on aerial imagery collected between the 1950s and 1990s. Several of the important lake districts, including Beringia, Kobuk Delta, Iliamna, Selawik, Tikchik, and Yukon-Kuskokwim Delta, are located in western Alaska. Among all 20 key lake districts identified by Arp and Jones (2009), Yukon-Kuskokwim Delta, Iliamna, Selawik, and Kobuk Delta have the highest limnetic ratio (percentage lake surface area) of greater than 15%. In addition, lake districts in western Alaska do occur along a wide North to South gradient of varying permafrost extent which makes these lake districts an interesting domain for studying the effects of permafrost characteristics on regional lake distribution and change.

Published studies on spatial distribution of lakes and changes in western Alaska are sparse. Recent studies carried out by Jones et al. (2011) in small regions of Beringia and Roach et al. (2013) in portions of Selawik demonstrated that lake surface area is declining in both regions owing to permafrost degradation. Jones et al. (2011) recorded numerous significant lake drainage events in Beringia since 1950/51. They estimated long-term mean expansion of thermokarst lakes in the region between 1950/51 and 2006/07 to be about 0.37 m/year, whereas they found that a large number of lakes, mostly lakes greater than 40 ha, drained in their 700 km^2 study region with a drainage rate of 2.3 lakes/year. Roach et al. (2013) estimated that lake area declined by 0.81% per year on average between 1985-86 and 2007-09 in their study site located within the Selawik National Wildlife Refuge and predicted that lake area could decline by almost 33% within 50 years. This evidence of rapid lake drainage events in some portions of western

Alaska demonstrates the need to identify trends in lake dynamics for other major lake districts of this region.

In this study we used medium resolution Landsat images to understand lake distribution and changes in six lake districts spanning a wide gradient of permafrost extents from continuous to sporadic within the Western Alaska Land Conservation Cooperative (WALCC) region. This region encompasses several villages such as Nome, Kotzebue, Bethel, Selawik and important conservation areas such as multiple National Parks and Preserves (Bering Land Bridge National Preserve, Kobuk Valley National Park) and multiple Fish and Wildlife Refuges (Selawik National Wildlife Refuge, Yukon Delta Wildlife Refuge), and is therefore of very high interest to land and resource managers. The main objectives of this study are to (1) understand broad-scale lake distribution in the major lake districts of the WALCC region; (2) investigate changes in lake area in the region since the 1970s; and (3) investigate how changes in lakes may vary between different permafrost zones of that region.

5.3. Study area

The study sites represent six lake-rich areas located in the northern and central WALCC region covering a total area of 68,831 km^2; (1) Baldwin Peninsula (2) Beringia (northern Seward Peninsula lowlands as named by Arp and Jones (2009)) (3) Central Seward Peninsula, (4) Kobuk Delta, (5) Selawik, (5) Central Seward Peninsula, and (6) Yukon-Kuskokwim Delta (YK Delta) (Figure 5.1). Four of these areas were already identified as major lake districts by Arp and Jones (2009) (Beringia, Kobuk Delta, Selawik, and YK Delta), while two smaller areas rich in lakes are additionally included (Baldwin Peninsula and Central Seward Peninsula) based on the concentration of lakes relative to other areas in western Alaska and their proximity to major villages. The outlines of the lake study areas in Beringia and YK Delta do not match with the same lake districts in Arp and Jones (2009) because the study domain boundaries were determined by useable cloud-free imagery available for the study time period (1970s and 2014). Hence, the study areas in Beringia and YK Delta are subareas covering about 91% and 64%, respectively, of the original lake districts delineated by Arp and Jones (2009) (Figure 5.1). We did not cover lake districts in the southern WALCC region.

Permafrost characteristics in the studied WALCC lake regions are extracted from the digital dataset from Jorgenson et al. (2008) at the map scale of 1:7,200,000 and vary from continuous

extent in the north to isolated extent in the south (Supplementary Table 5.1). Based on this data, continuous permafrost (> 90% permafrost cover) is found in the Northern Seward Peninsula and Baldwin Peninsula. More than 90% of the Kobuk Delta study area is also covered by continuous permafrost and the rest of the area in the east is covered by discontinuous permafrost (50-90% permafrost cover). Most of the Central Seward Peninsula is characterized by continuous permafrost and a small portion in the south is characterized by discontinuous permafrost. Selawik is also characterized by continuous and discontinuous permafrost but continuous permafrost is distributed over the southern lowland. Isolated permafrost (up to 10% permafrost cover) is distributed in the outer western belt of YK Delta, while discontinuous and sporadic permafrost (10-50% permafrost cover) cover the eastern delta lowlands. Permafrost temperatures are available from some sites in the study domain through Global Terrestrial Network – Permafrost (GTN-P) boreholes. They are coldest in the northern areas with -3.6 ^{o}C at 20 m depth recorded at the Kotzebue borehole on the Baldwin Peninsula (Romanovsky et al., 2010). Based on the Jorgenson et al. (2008) permafrost map, ground ice content is high in Beringia and moderate in Kobuk Delta. It is largely moderate to high in Central Seward Peninsula, Baldwin Peninsula, and Selawik. In YK-Delta, ground ice content is low to high (Supplementary Table 5.2).

The study regions encompass various types of lakes; thermokarst lakes are the most common type, while oxbow and delta lakes are also widely distributed in the river floodplains and delta regions. Additional lake types include maar, tidal, and coastal lakes. The study regions contain extensive loess deposits in the uplands and sandy or silty alluvial and fluvial deposits in the river floodplains and delta regions. Other types of geologic deposit found are sand dunes, old glaciolacustrine deposits, glaciofluvial outwash, modified moraine and volcanic deposits (Supplementary Table 5.3). Mean annual air temperature is characterized by a south to north gradient with temperatures ranging from 0-6 ^{o}C (Jorgenson et al., 2008).

5.4. Data and methods

5.4.1. Data

We collected Landsat L1T-processed, terrain-corrected images acquired during two different time periods (MSS, 60m, 1972-1975; and OLI, 30m, 2013-2014) from the USGS Landsat repository (http://earthexplorer.usgs.gov) (Supplementary Table 5.4).

The selection criteria included imagery with less than 10% cloud cover acquired during the summer (June – early September) of 1970s and 2010s. All images for the 1970s were from 1974/75 with the exception of one tile from 1972 that covered a portion of Beringia for which useable imagery from 1974/75 was not available. For the second time period of 2010s, we used the images acquired during the summer of 2014. However, we had to use two image tiles from the year 2013 to map lakes in some portions of Selawik and YK Delta since useable 2014 images were not available. Altogether, we used 12 Landsat MSS image tiles covering a total land surface area of 377,400 km^2 and 14 Landsat OLI image tiles covering a total land surface area of 435,540 km^2 to extract lakes for these two time steps.

We further used a digital permafrost dataset linked to permafrost extent map created by Jorgenson et al. (2008) to understand the role of permafrost extent on lake area changes in the study regions.

5.4.2. Lake mapping and change analysis

In order to map lakes greater than 1 ha in Landsat images we applied a semi-automated lake classification using Object-Based Image Analysis (OBIA) methods in the commercial software package eCognition™ Developer 8. OBIA consists of two steps: (1) image segmentation, i.e. aggregation of homogenous image pixels based on their spatial and spectral homogeneity into meaningful clusters known as image objects, and (2) classification of image objects (Navulur, 2007; Blaschke and Strobl, 2001). Rather than identifying a surface feature simply based on spectral pixel information in a single step as in a traditional classification technique, OBIA requires users to decompose an image into meaningful objects, organize them in a conceptual hierarchy based on their relationships and integrate object semantics in classification rulesets in an iterative fashion until the target objects are identified more accurately (Blaschke and Strobl, 2001; Navulur, 2007; Blaschke et al., 2008).

In the first step, prior to image segmentation, we performed spectral transformation on visible and infrared bands utilizing Principal Component Analysis (PCA) on all images for image enhancement and better spectral separation of water bodies from various surface features (Mather and Koch, 2011). For further analysis, we only used the first two PC bands that carried the most variance (> 99%).

We implemented OBIA techniques that involved segmentation of the original set of image bands and the first two PC components followed by a classification of image objects based on a range of classification rulesets. The Normalized Difference Water Index (NDWI) and Modified Normalized Difference Water Index (MNDWI) guided the waterbody identification on Landsat MSS and OLI images, respectively (McFeeters, 1996; Xu, 2006; Li et al., 2013). NDWI and MNDWI were calculated using the following equations:

For Landsat MSS:

$$NDWI = \frac{G - NIR}{G + NIR}$$

Equation (5.1)

For Landsat OLI:

$$MNDWI = \frac{G - SWIR2}{G + SWIR1}$$

Equation (5.2)

(Definitions of bands: G – Green, NIR – Near Infrared, SWIR-2 – Short-Wave Infrared 2)

Water surfaces are characterized by a high absorption in infrared wavelengths making them dark against their surrounding terrain in infrared image bands (NIR, SWIR). Because of this property of water surfaces, NDWI and MNDWI spectral indices can help enhance the contrast between water bodies and the surrounding land surface (McFeeters 1996; Xu, 2006; Li et al., 2013). The enhancement in the MNDWI index was previously found to result in more accurate identification and delineation of open water features (Xu, 2006; Li et al., 2013). However, because a SWIR band is not available in early Landsat images, we used NDWI for mapping water bodies on the 1970s MSS images.

We used the U.S. Geological Survey National Elevation Dataset (NED) DEM and a derived hillshade to remove misclassified non-water objects associated with terrain shadows, which appear dark on imagery similar to water surfaces. Manual assessment, correction, and removal of streams and channels were conducted to remove spurious misclassifications of water bodies that still persisted. Lake-connected rivers, streams and drainage channels were also removed manually to create clean lake polygon layers for each image. We merged water body polygons derived from multiple Landsat tiles from the same time period to create one single final product that represented lake distribution for that particular time step. Among the duplicated lake polygons from the image-overlapping areas, we selected lakes extracted from the latest imagery for the final output. We classified lakes greater than 1 ha into four different size classes (1) 1-10 ha (<10 ha); (2) 10-50 ha; (3) 50-100 ha; and (4) greater than 100 ha (>100 ha).

For each study region, we (1) calculated limnicity (percent lake cover), total lake number and lake area for 1970s and 2014, and net change between 1970s and 2014 to identify the direction of change over time for each study area, and (2) estimated total lake number and lake area for 1970s and 2014, and net change between 1970s and 2014 for each lake size class for comparing changes among four size classes in each study region.

For each permafrost extent type (continuous, discontinuous, sporadic, isolated; Jorgenson et al., 2008) we (1) estimated limnicity, total lake number and lake area for 1970s and 2014, and net change between 1970s and 2014 to identify the direction of change over time for each permafrost zone, (2) calculated total lake number and lake area for 1970s and 2014, and net change between 1970s and 2014 for each lake size class for comparing changes among four size classes in each permafrost extent type, and (3) investigated changes between 1970s and 2014 in lake abundance ratio for individual lakes to the total lake abundance (LN_{ratio}) and lake surface area ratio for individual lakes to the total lake surface area (LA_{ratio}) with respect to lake size. Since net change only summarizes a regional gain or loss, lake abundance and lake surface area ratio for individual lakes account for all changes and help to identify specific trends in regional lake distribution pattern.

5.5. Results

5.5.1. Lake distribution in each study region (ca. 2014)

The highest limnicity values for lakes larger than 1 ha among the six studied regions is found in YK Delta where approximately 16% of the area mapped is covered with lakes (Table 5.1). The lowest limnicity is found on Baldwin Peninsula with an average of only about 3.5%. The lake districts in river deltas have the highest average limnicity with all three regions dominated by deltas (Kobuk Delta, Selawik and YK Delta) having a limnicity above 10% (Table 5.1).

All studied regions are governed by a large number of lakes smaller than 10 ha (Table 5.1). More than 70% of the total number of lakes larger than 1 ha in all the study regions are smaller than 10 ha and less than 3% are larger than 100 ha. However, in five out of six study regions (Beringia, Central Seward Peninsula, Kobuk Delta, Selawik, and YK Delta) large lakes greater than 100 ha make up 40% or more of the total lake surface area mapped in the region (Table 5.1). In Central Seward Peninsula, about 72% of the total lake surface area is contributed by two very large lake systems (>100 ha) (Imuruk Basin, a large lagoonal lake system, and Imuruk Lake, located in a lava plateau); while the remaining percent lake cover is made up of small thermokarst lakes. In Beringia, there are many small as well as large thermokarst lakes and 5 large maar lakes (average maar lake size of ~ 1000 ha). Kobuk Delta and Selawik have many thermokarst, delta, and oxbow lakes. In Selawik, there is one large lake called Inland Lake that makes up 25% of the total lake surface area. In the analysis we did not include Selawik Lake, which is a very large lagoon. In the YK Delta, there are many thermokarst, delta, oxbow, and tidal flat lakes of all sizes as well as some small maar lakes. In contrast, Baldwin Peninsula shows a dominance of lakes smaller than 50 ha, mostly thermokarst lakes, making up 70.8% of total lake surface area.

5.5.2. Lake changes in each study region (1972-2014)

5.5.2.1. Changes in lake area

Lake area change was found to be positive in some study areas while negative in others and within all study sites we observed a mix of lake dynamics, including lake expansion and lake drainage. (Table 5.1, Figure 5.2). Examples of lake drainage and expansion are illustrated in Figure 5.3 and Figure 5.4. For three study regions (Baldwin Peninsula, Kobuk Delta, and YK

Delta) a net increase in total lake area by less than 4% was observed, while the other three regions (Beringia, Central Seward Peninsula, and Selawik) showed a net lake area decrease ranging between ~ 4-15% (Tables 5.1, 5.5). The most significant change was noticed in Beringia and Central Seward Peninsula due to the drainage of very large lakes. We found that about 15.3% (-6318.1 ha or -115.9 ha/100 km^2) and 12.4% (-6542.1 ha or -110.2 ha/100 km^2) of total lake surface area was lost since the 1970s in Beringia and Central Seward Peninsula, respectively. We noticed that 66.2% of lake area lost came from drainage of lakes >100 ha in Beringia and estimated a total area loss of 23.2% for lakes >100 ha (-4471.8 ha or -82 ha/100 km^2). In Central Seward Peninsula, we found that 93.4% of area loss came from drainage of lakes larger than 100 ha. Here the total area of lakes >100 ha declined by 15.2% (-6391.1 ha, -107.6 ha/100 km^2). The drainage of lakes <100 ha contributed to a total area loss of 15% (-2284.5 ha or -41.9 ha/100 km^2) in Beringia and 6.5% (-448.9 ha or -2.5 ha/100 km^2) in Central Seward Peninsula. However, lakes <10 ha gained total surface area in both Beringia and Central Seward Peninsula by 6.5% (438.1 ha 8 ha/100 km^2) and 7.7% (297.87 ha 5 ha/100 km^2), respectively.

Selawik experienced the highest number of drainage events but because most of the lakes that drained were small, the net lake area loss in Selawik is the smallest among all study areas. Drained lakes in the 1-50 ha category in Selawik contributed a total area loss of 5021.1 ha, which is about 81% of the area loss (-6171.2 ha or -79 ha/100 km^2) in the region. Contrary to other regions, Selawik experienced a loss in total area of lakes <10 ha by 6.3% (-914.9 ha or -14.4 ha/100 km^2). In contrast, we saw expansion of lakes >100 ha by 7% (2812.3 ha or 44.3 ha/100 km^2). Hence, the net lake area loss in Selawik was 3.9% (-3358.9 ha or -52.9 ha/km^2).

The largest net lake area increase was observed in Baldwin Peninsula with an increase of 3.9% (204 ha or 13.4 ha/100 km^2). Here, lakes <10 ha as well as large lakes >100 ha gained surface area by 16.8% (259.6 ha or 16.9 ha/100 km^2) and 14.9% (119.7 ha or 7.8 ha/100 km^2), respectively. There was only a very small increase in area for lakes in the category 10-50 ha by 0.1% (2.7 ha or 0.2 ha/100 km^2). In contrast, lake surface area declined for lakes in the category 50-100 ha by 20.4% (-177.2 ha or –11.6 ha/100 km^2). Similarly, in Kobuk Delta we observed an increase in surface area for lakes <10 ha as well as large lakes >100 ha by 4.8% (194.4 ha or 10.1 ha/100 km^2) and 4.3% (479.5 ha or 24.9 ha/100 km^2), respectively. But the surface area declined

for lakes in categories 10-50 ha and 50-100 by 1.9% (-152.2 ha or -7.9 ha/100 km^2) and 3.1% (-137.9 ha or -7.2 ha/100 km^2), respectively. This contributed to a net lake area increase in the Kobuk Delta region by 1.4% (383.7 ha or 19.9 ha/100 km^2). In YK Delta, we observed only a slight net increase in lake area by 0.5% (3922.8 ha or 8.4 ha/100 km^2). The largest change and the only increase in lake surface area of 10.2% (11,907.8 ha or 25.5 ha/100 km^2) was observed for lakes smaller than 10 ha. We observed that that total surface area of lakes >10 ha decreased by 1.2% (-7985.2 ha or -0.3 ha/100 km^2), with the smallest change observed in lakes larger than 100 ha by 0.8% (-3643.5 ha or -7.8 ha/100 km^2).

5.5.2.2. Change in lake number

The analysis indicated that the total number of individual lakes increased in all study regions ranging between 1.3-27.1% (Table 5.1, Figure 5.5). Baldwin Peninsula, Central Seward Peninsula, and YK Delta observed a net increase in number of lakes by more than 10%; 27.1% (154 lakes or 10.1 lakes/100 km^2), 12.6% (178 lakes or 3 lakes/100 km^2) and 11.4% (5215 lakes or 11.2 lakes/100 km^2), respectively. In Beringia, Selawik, and Kobuk Delta, we observed a net increase of 6.4% (160 lakes or 2.9 lakes/100 km^2), 2.2% (111 lakes or 1.7 lakes/100 km^2), and 1.3% (22 lakes or 1.1 lakes/100 km^2), respectively.

Baldwin Peninsula, Beringia, Central Seward Peninsula, and YK Delta had an increase in the number of small lakes <10 ha by more than 14%. The largest increase of 34.7% (155 lakes or 10.1 lakes/100 km^2) was observed in Baldwin Peninsula. The YK Delta region also showed a significant increase in number of lakes by 14.4% (5354 lakes or 11.5 lakes/100 km^2). The number of lakes <10 ha increased by 14.9% (278 lakes or 5.1 lakes/100 km^2) and 16.3% (185 lakes or 3.1 lakes/100 km^2) in Beringia and Central Seward Peninsula, respectively. Selawik showed an increase of 9.2% (185 lakes or 3.1 lakes/100 km^2) in number of lakes <10 ha. The smallest increase was observed in Kobuk Delta. Here, the number of lakes <10 ha increased by 3.5% (40 lakes or 2.1 lake/100 km^2).

We noticed the largest decline in number of lakes >10 ha in Selawik (-238 lakes or -3.7 lakes/100 km^2) and Beringia (-118 lakes or -2.2 lakes/100 km^2). In Selawik, a large number of small lakes drained, but in Beringia a significant number of large lakes drained. In Selawik 92% of the draining lakes were in the 10-50 ha size class compared to 72% in Beringia. In Selawik the number of lakes in size class 10-50 ha declined by 20.1% (-219 lakes or -3.4 lakes /100 km^2)

(Table 5.1, Figure 5.5). In Beringia the lake number declined by 17.3% (-85 lakes or -1.6 lakes/100 km^2). For 50-100 ha size class, the lake number declined by 13.8% in Selawik (-18 lakes or -0.3 lakes/100 km^2) and by 16% in Beringia (-13 lake or -0.2 lakes/100 km^2). In Beringia, 20 lakes >100 ha drained (-27.4% or -0.4 lakes/100 km^2) but only 1 lake >100 ha drained (-1.7% or -0.02 lakes/100 km^2) in Selawik.

Central Seward Peninsula, Kobuk Delta and YK Delta also lost in total 7, 18, and 139 lakes >10 ha, respectively, i.e., less than 1% decline in number of lakes or loss of less than 1 lake/100 km^2. More than 55% of the draining lakes were in the 10-50 ha size category in Kobuk Delta (-10 lakes, or -2.7%) and YK Delta (-96 lakes, or -1.4%). In Central Seward Peninsula, 42.9% of the draining lakes (-3 lakes, or -1.3%) were in the 10-50 ha size class. Central Seward Peninsula, Kobuk Delta and YK Delta lost in total 2 (-7.7%), 6 (-9.4%) and 14 (-1.5%) lakes in the 50-100 ha size category, respectively. For the YK Delta we observed a loss of lakes >100 by 3.4% due to drainage of 29 very large lakes. Two lakes >100 ha drained in Central Seward Peninsula and Kobuk Delta, that contributed towards the decline in number of lakes >100 ha by 11.8% and 4.1%, respectively. Baldwin Peninsula had the least decline in number of lakes >10 ha. It lost 2 lakes (-15.4%) in the 50-100 ha size category but gained 1 lake >100 ha (33.3%), i.e. change in lake number by less than 1 lake/100 km^2.

5.5.3. Lake changes in the continuous permafrost zone (1972-2014)

5.5.3.1. Overall changes in the continuous permafrost zone

The limnicity of the continuous permafrost zone was 6.2% in the 1970s and decreased to 5.8% in 2014 (Table 5.2). There was a predominance of small lakes in the continuous permafrost zone with more than 74% of the lakes being smaller than 10 ha. However, lakes >100 ha made up almost 40% of the total surface area of lakes mapped in the region (Table 5.2, Figure 5.6). Between 1970s and 2014, LN_{ratio} of lakes <10 ha increased the most in the continuous permafrost zone among all permafrost zones by 4.83%. In contrast, LN_{ratio} of lakes >10 ha also showed the largest decline with the maximum decline of 3.67% happening in 10-50 ha size class. The LN_{ratio} of lakes >50 ha decreased by less than 0.6%, while the LA_{ratio} of lakes <50 ha increased by approx. 2% with an increase of 2.7 % happening in lakes <10 ha. The LA_{ratio} slightly increased by about 2% for very large lakes >500 ha despite a decrease in LA_{ratio} of 1.47% in lakes >100 ha.

Lakes in the continuous permafrost zone increased in number by 9.4% (615 lakes or 4.2 lakes/100 km^2) but shrunk in area by 6.7% (-6527.4 ha or -44 ha/100 km^2), the largest area loss among all permafrost zones (Table 5.2). The total lake number and total surface area of lakes <10 ha increased by 16.5% (804 lakes or 5.4 lakes/100 km^2) and 7.1% (1255.7 ha or 8.5 ha/100 km^2), respectively. The number of lakes in size classes 10-50 ha, 50-100 ha and >100 ha declined by less than 1 lake/100 km^2 with a loss of 10.5% (-139 lakes), 12.9% (-26 lakes) and 15.6% (-24 lakes), respectively. The area of lakes in size classes 10-50 ha, 50-100 ha and >100 ha also decreased by 8.8% (-2395.4 ha or -16.2 ha/100 km^2), 10.5% (-1420 ha or -9.6 ha/100 km^2) and 10.1% (-3967 ha or -26.8 ha/100 km^2), respectively.

5.5.3.2. Regional changes in the continuous permafrost zone

We observed that small lakes in the continuous permafrost zone dominate all regions and a significant increase in LN_{ratio} of small lakes is recorded for the Baldwin Peninsula, Beringia, Central Seward Peninsula and Selawik with an increase in LN_{ratio} of lakes <10 ha by more than 4% (Figure 5.6). In Beringia and Selawik, we observed the highest increase of 5.9% in LN_{ratio} of lakes <10 ha. Kobuk Delta had the least increase of 1.2%. We observed a decrease in LN_{ratio} in the other 3 size classes of lakes except in Baldwin Peninsula, where lakes >100 ha showed a slight increase in LN_{ratio} by 0.03%.

All regions showed an overall increase of LA_{ratio} for smaller lakes (Figure 5.6). In Beringia LA_{ratio} of lakes <100 increased by 4.06% due to a significant LA_{ratio} increase of 4.22% for lakes <10 ha but LA_{ratio} for lakes >100 ha decreased by 4.34%. In Baldwin Peninsula LA_{ratio} for lakes <50 ha increased by 2.2%. Central Seward Peninsula and Selawik also show an increased LA_{ratio} for lakes <20 ha by 1.3% and 3.4%, respectively. In these three regions, Baldwin Peninsula, Central Seward Peninsula, and Selawik, lakes >100 ha also had an increase in LA_{ratio} by 1.6%, 1.4%, and 0.7%, respectively. The change in LA_{ratio} of smaller lakes in Kobuk Delta is not as large as in other areas. However, this study region shows an overall increase in LA_{ratio} for lakes >50 ha by 0.5% and an increase by 1.02% for lakes >100 ha.

The study shows that there was a slight increase in total lake surface area in three out of five study sites that have continuous permafrost distribution. Baldwin Peninsula, Central Seward Peninsula and Kobuk Delta had an increase (<4%) of lake surface area in the continuous permafrost region (Table 5.3, Figure 5.7). Baldwin Peninsula gained the highest lake surface area

with a net increase of 3.9% (204.9 ha or 13.4 ha/100 km^2). Central Seward Peninsula had the smallest net increase in lake area of 0.3% (19.8 ha or 0.5 ha/100 km^2) and Kobuk Delta had a net increase of 1.8% (475.6 ha or 29.8 ha/100 km^2). In contrast, Beringia and Selawik showed a net decrease in lake area by 15.3% (-6318 ha or -115.9 ha/100 km^2) and 4.8% (-909.6 ha or -37.3 ha/100 km^2), respectively (Table 5.3, Figure 5.7).

There was a net increase in total number of lakes by 27.1% (154 lakes or 10.1 lakes/100 km^2) for Baldwin Peninsula, 15.1% (221 lakes or 9.1 lakes/100 km^2) for Selawik, 13.9% (65 lakes or 1.7 lakes/100 km^2) for Central Seward Peninsula, 6.4% (160 lakes or 2.9 lakes/100 km^2) for Beringia, and 1% (15 lakes or 0.9 lakes/100 km^2) for Kobuk Delta (Table 5.3, Figure 5.7).

We observed an increase in number of lakes <10 ha by 34.7% (155 lakes or 10.1 lake/100 km^2) for Baldwin Peninsula, 24.1% (269 lakes or 11 lakes/100 km^2) for Selawik, 19.5% (72 lakes or 1.9 lakes/100 km^2) for Central Seward Peninsula, and 14.9% (278 lakes or 5.1 lakes/100 km^2) for Beringia (Table 5.3, Figure 5.7). Kobuk Delta had the smallest increase of 2.8% (30 lakes, 1.9 lakes/100 km^2). The total area of lakes <10 ha showed a similar pattern as the lake number with an increasing area by 16.8% (259.6 ha or 16.9 ha/100 km^2) for Baldwin Peninsula, 7% (301.8 ha or 12.4 ha/100 km^2) for Selawik, 6.5% (438.1 ha or 8 ha/100 km^2) for Beringia, 8.3% (106.9 ha or 2.8 ha/100 km^2) for Central Seward Peninsula, and 3.9% (149.2 ha or 9.3 ha/100 km^2) for Kobuk Delta (Table 5.3, Figure 5.7).

Total area of lakes in the 10-50 ha size class declined the most by 15.4% (-1525.7 ha or -28 ha/100 km^2) in Beringia and by 12% (-718.1 ha or -29.5 ha/100 km^2) in Selawik (Table 5.3, Figure 7). The smallest positive change of 0.1% (2.7 ha or 0.2 ha/100 km^2) was observed for Baldwin Peninsula. The increase in area of lakes in the 10-50 ha size class was 5.3% (84.3 ha or 2.2 ha/100 km^2) for Central Seward Peninsula and 0.9% (70 ha or 4.4 ha/100 km^2) for Kobuk Delta. A similar pattern was observed for lakes in the 50-100 ha size class with the largest decrease of 20.4% (-177.2 ha or -11.6 ha/100 km^2) in Baldwin Peninsula and the smallest decrease of 1.7% (-72.2 ha or -4.5 ha/100 km^2) in Kobuk Delta (Table 5.3, Figure 5.7). The decrease in area of lakes in the 50-100 ha size class was 14.4% (-758.8 ha or -13.9 ha/100 km^2) for Beringia, 14.2% (-95.2 ha or -2.5 ha/100 km^2) for Central Seward Peninsula, and 12.9% (-316.8 ha or -13 ha/100 km^2) for Selawik.

Similarly, the number of lakes in both the 10-50 ha and 50-100 ha size classes declined in all five regions that have continuous permafrost with the largest decline observed in Beringia and Selawik (Table 5.3, Figure 5.7). There was a decrease in the number of lakes in the 10-50 ha size class by 17.3% (-85 lakes or -1.6 lakes/100 km^2) for Beringia, 14% (-41 lakes or -1.7 lakes/100 km^2) for Selawik. Central Seward Peninsula and Kobuk Delta experienced fewer lake drainages in the 10-50 ha size class with 6.4% (-5 lakes) and 2.3% (-8 lakes), respectively, which amounts to a loss of less than 1 lake/100 km^2. In contrast, there was no change in number of lakes in the 10-50 ha size class for Baldwin Peninsula. The number of lakes in the 50-100 ha size class declined by 16% (-13 lakes) for Beringia, 15.4% (-2 lakes) for Baldwin Peninsula, 13.9% (-5 lakes) for Selawik, 11.1% (-1 lake) for Central Seward Peninsula, and 8.1% (-5 lakes) for Kobuk Delta, i.e. by less than 1 lake/100km^2 in all regions (Table 5.3, Figure 5.7).

Beringia and Selawik experienced drainage of lakes >100 ha by 23.2% (-4471.7 ha or -82 ha/100 km^2) and 2.8% (-176.5 ha or -2.8 ha/100 km^2), respectively (Table 5.3, Figure 5.7). In contrast, the total area of lakes >100 ha increased in Baldwin Peninsula, Central Seward Peninsula and Kobuk Delta by 14.9% (119.7 ha or 7.8 ha/100 km^2), 4.2% (92.4 ha or 1.6 ha/100 km^2) and 4.3% (468.6 ha or 24.3 ha/100 km^2), respectively, contributing towards the total lake area increase in the region. There was a change in number of lakes >100 ha by less than 1 lake/100 km^2 in all regions. The total number of lakes >100 ha decreased by 27.4% for Beringia (-20 lakes), 10.5% (-2 lakes) for Selawik, 8.3% (-1 lake) for Central Seward Peninsula, and 4.3% for Kobuk Delta (-2 lakes). In contrast, Baldwin Peninsula had an increase in total number of lakes >100 ha by 33.3% (1 lake) (Table 5.3, Figure 5.7).

5.5.4. Lake changes in the discontinuous permafrost zone (1972-2014)

5.5.4.1. Overall changes in the discontinuous permafrost zone

The limnicity of the discontinuous permafrost zone was 14.7% in 1970s and decreased to 14.5% in 2014 (Table 5.2). We observed a predominance of small lakes in the discontinuous permafrost zone with more than 80% of the lakes being smaller than 10 ha. However, lakes >100 ha made up 50% of the total surface area of lakes mapped in the region (Table 5.2, Figure 5.8). We observed similar patterns of change in the LN_{ratio} for lakes in the discontinuous permafrost zone as in the continuous permafrost (Figure 5.8). There was an overall increase in abundance of

smaller lakes with an increase in LN_{ratio} for lakes <10 ha by 2.5%. Unlike in the continuous permafrost zone, LA_{ratio} of small lakes in the discontinuous permafrost region did not show a significant change between 1970s and 2014 with only a slight increase of 0.8% in LA_{ratio} of lakes for lakes <10 ha (Figure 5.8). In addition, there was a decrease in LA_{ratio} for lakes <50 ha by 0.7%. However, there was a large increase of 1.3% in LA_{ratio} for lakes >100 ha.

Lakes in the discontinuous permafrost zone increased in number by 6.7% but their total area decreased by 1.64 % (Table 5.2). The total lake number and total surface area of lakes <10 ha increased by 10% (1861 lakes or 8.2 lakes/100 km^2) and 2.5% (1547.7 ha or 6.8 ha/100 km^2), respectively. The total number of lakes in the size class 10-50 ha decreased by 7.4% (-265 lakes or -1.2 lakes/100 km^2) and their total surface area also declined by 8.1% (-5915.2 ha or -26 ha/100 km^2). The number of lakes in sizes class 50-100 ha and >100 ha declined by 7.6% (-35 lakes) and 5.8% (-23 lakes), respectively, i.e. a decline by less than 1 lake/100 km^2. The area of lakes belonging to the size class 50-100 ha decreased by 6.8% (-2173.5 ha or -9.6 ha/100 km^2). In contrast, total surface area of lakes >100 ha increased by 0.6% (1044.9 ha or 4.6 ha/100 km^2).

5.5.4.2. Regional changes in the discontinuous permafrost zone

The LNratio and LAratio of different lake size categories in the discontinuous permafrost zone from different lake districts show larger variability than in the continuous permafrost zone (Figure 5.8). We observed that small lakes also dominated the discontinuous permafrost zones of Central Seward Peninsula, Kobuk Delta, Selawik, and YK Delta (Figure 5.8) with an increase in LNratio for lakes <10 ha in all regions. The largest increase in LNratio of small lakes is observed in Selawik and Kobuk Delta with an increase of 5.07% and 4.66% in lakes <10 ha. The LNratio for lakes <10 ha in Central Seward Peninsula and YK Delta increased by 1.9% and 2%, respectively. We observed a decrease in LNratio in the other three lake size classes except for Selawik, where lakes >100 ha showed a slight increase in ratio (0.06%).

For three out of four regions with discontinuous permafrost (Central Seward Peninsula, Kobuk Delta and YK Delta) the LAratio for lakes <10 ha increased (Figure 5.8). The largest increase in LAratio of small lakes was observed for the Central Seward Peninsula. Kobuk Delta also showed an increase in LAratio of lakes smaller <50 ha by 1.3% but also an increase in LAratio of lakes >100 ha by 3.4%. In contrast, Selawik showed a decrease in LAratio of lakes <10 ha by 1.1% and an overall increase in LAratio of larger lakes (Figure 5.5d) with the largest

increase of 7% for lakes >100 ha. However, the YK Delta showed only small changes of less than 1% in LAratio compared to the other study sites.

The study shows that there was a net decrease of about 3-7% in total lake surface area in the discontinuous permafrost zone of all lake districts (Table 5.3, Figure 5.7). Kobuk Delta had the largest decline in net surface area by 7.4% (-94.5 ha or -46.9 ha/100 km^2) followed by YK Delta, where we estimated a net surface area decline of 4.8% (-2421.2 ha or -14 ha/100 km^2). Central Seward Peninsula and Selawik experienced lake surface area loss by 3.1% (-242.9 ha or -13 ha/100 km^2) and 4.3% (-2737.4 ha or -81.6 ha/100 km^2) respectively. However, the total number of lakes increased by about 6-11% in three out of four study regions while Selawik had an overall decrease of 3% (-104 lakes or -3.1 lakes/100 km^2) in lake numbers (Table 5.3, Figure 5.7). The number of lakes increased by 11.8% (108 lakes or 5.8 lakes/100 km^2) for Central Seward Peninsula, 6.6% (6 lakes or 3 lakes/1002) for Kobuk Delta and 8.3% (1528 lakes or 8.8 lakes/100 km^2) for YK Delta.

There was an overall increase in total area of lakes <10 ha in Central Seward Peninsula by 6.7% (171 ha or 9.2 ha/100 km^2), in Kobuk Delta by 17% (42.5 ha or 21.1 ha/100 km^2), and in YK Delta by 7% (2437.2 ha or 14.1 ha/100 km^2) (Table 5.3, Figure 5.7). However, Selawik showed a significant decrease of 11.2% (-1103 ha or -32.9 ha/100 km^2) in the total area of lakes <10 ha despite a slight increase in their number by 3.5% (91 lakes or 2.7 lakes/100 km^2). Also, the number of lakes <10 ha increased by 14.2% (107 lakes or 5.7 lakes/100 km^2) for Central Seward Peninsula, 13.2% (9 lakes or 4.5 lakes/100 km^2) for Kobuk Delta, and 10.9% (1654 lakes or 9.5 lakes/100 km^2) for YK Delta (Table 5.3, Figure 5.7).

We observed that lakes in the 10-50 ha size class shrunk in area in all study regions (Table 5.3, Figure 5.7) with the largest decline of 21.2% (-3221.1 ha or -96 ha/100 km^2) for Selawik. The surface area of lakes in the 10-50 ha size class declined by 16.4% (-82.2 ha or -40.8 ha/100 km^2) for Kobuk Delta, 12% (-2456.1 ha or -14.2 ha/100 km^2) for YK Delta, and 4.7% (-155.8 ha or -8.4 ha/100 km^2) for Central Seward Peninsula. The total number of lakes in the 10-50 ha size class showed a similar declining pattern as the lake area except for Central Seward Peninsula where lake numbers increased by 1.9% (3 lakes or 0.2 lakes/100 km^2) (Table 5.3, Figure 5.7). It decreased by 23.6% (-176 lakes or -5.2 lakes/100 km^2) for Selawik, 10.5% (-2 lakes or -1 lake/100 km^2) for Kobuk Delta, and 3.4% (-90 lakes or -0.5 lakes/100 km^2) for YK Delta.

There was also shrinkage in total surface area of lakes in 50-100 ha size class in all study regions with the largest decline of 51.4% (-65.7 ha or -32.6 ha/100 km^2) observed for Kobuk Delta and the smallest decline of 6.9% (-84.5 ha or -4.5 lakes/100 km^2) for Central Seward Peninsula (Table 5.3, Figure 5.7). Selawik and YK Delta also had a large decline in total surface area of lakes in the 50-100 ha size class by 22.4% (-1326.2 ha or -39.5 ha/100 km^2) and 12.9% (-697.1 ha or -4 ha/100 km^2), respectively. The total number of lakes in the 50-100 ha size class decreased by less than 1 lake/100 km^2. It declined by 50% (-1 lake) for Kobuk Delta, 23% (-20 lakes) for Selawik, 6.3% (-1 lake) for Central Seward Peninsula, and 3.6% (-13 lakes) for YK Delta (Table 5.3, Figure 5.7).

Central Seward Peninsula and YK Delta also experienced drainage of lakes >100 ha with a total area loss by 26.89% (-173.6 ha or -9.3 ha/100 km^2) and 2.81% (-1705.3 ha or -9.8 ha/100 km^2), respectively (Table 5.3, Figure 5.7). In contrast, the total area of large lakes >100 ha increased in Kobuk Delta and Selawik by 2.72% (10.9 ha or 5.4 ha/100 km^2) and 8.74% (2912.9 ha or 86.8 ha/100 km^2) respectively. There was a change in the number of lakes >100 ha by less than 1 lake/100 km^2 in all regions except in Kobuk Delta where we did not find any change. The total number of lakes >100 ha decreased by 33.3% (-1 lake) for Central Seward Peninsula, 6.5% (-23 lakes) for YK Delta, and 2.9% (-1 lake) for Selawik (Table 5.3, Figure 5.7).

5.5.5. Changes in sporadic permafrost zone (1972-2014)

The sporadic permafrost zone is only present in the YK Delta region among the six study sites and had the highest limnicity of >24% among all permafrost zones (Table 5.2). We observed a slight increase in limnicity from 24.3% to 24.9%. Here the LN_{ratio} and LA_{ratio} showed smaller variability compared to the continuous and discontinuous permafrost zones even though the patterns of LN_{ratio} and LA_{ratio} were similar (Figure 5.9). Similar to the continuous and discontinuous permafrost zones, the presence of smaller lakes also dominated the sporadic permafrost zone (close to 80% of the lakes were smaller than 10 ha) although lakes >100 ha made up more than 60% of the total lake surface area mapped in the region (Table 5.3, Figure 5.9). The LN_{ratio} showed an overall decrease for larger lakes like in the continuous and discontinuous permafrost zones. The largest increase in LN_{ratio} of almost 2% was observed for lakes <10 ha (Figure 5.9). We observed a small increase in LA_{ratio} for lakes <100 ha mostly because of an increase of 1.4% in the area ratio of lakes <10 ha and a less than 0.3% decrease in

LA_{ratio} of lakes belonging to the size class 10-100 ha (Figure 5.9). We also observed an increase in LA_{ratio} for very large lakes (>5,000 ha) by almost 2 %.

We found a net increase of 13.3% (2760 lakes or 15.2 lakes/100 km^2) in total number of lakes and a net increase of 2.7% (11718.1 ha or 64.4 ha/100 km^2) in total lake surface area (Table 5.3, Figure 5.7). In contrast to other permafrost zones, there was an increased lake abundance and lake surface area for all lake size classes. The largest increase in number and surface area was observed for lakes <10 ha. The total number of lakes <10 ha increased by 16.2% (2663 lakes or 14.6 lakes/100 km^2) and the total surface area increased by 14.4% (7460.8 ha or 41 ha/100 km^2) (Table 5.3, Figure 5.7). The total number increased by less than 1 lake/100 km^2 for lakes >10 ha. We observed an increase of 2.5% (82 lakes) for lakes in the 10-50 ha size class, 1% (5 lakes) for lakes in the 50-100 ha size class, and 2.1% (10 lakes) for lakes >100 ha. Similarly, the total surface area increased by 1% (699.4 ha or 3.8 ha/100 km^2) for lakes in the 10-50 ha size class, 0.7% (247 ha or 1.4 ha/100 km^2) for lakes in the 50-100 ha size class, and 1.2% (3310.9 ha or 18.2 ha/100 km^2) for lakes >100 ha (Table 5.3, Figure 5.7).

5.5.6. Changes in the isolated permafrost zone (1972-2014)

The isolated permafrost zone is present only in the YK Delta region and had the lowest limnicity of about 5% among all permafrost zones (Table 5.2). We observed a decrease in limnicity from 5.6% to 5.2%. We noticed that the presence of lakes <10 ha dominated this zone (more than 85%), however unlike in other zones, where very large lakes made up 40% or more of the total lake surface area, here in the isolated permafrost zone lakes <50 ha made up 70-75% of the total lake surface area mapped (Table 5.2, Figure 5.7). The LN_{ratio} showed an overall decrease of larger lakes similar to that in the other permafrost zones (Figure 5.9). We found the largest increase in LN_{ratio} of 3.4% for lakes <10 ha and a significant decrease in LN_{ratio} by 2.8% was found for lakes in the 10-50 ha size class. Similarly, there was an overall decrease in LA_{ratio} for larger lakes (Figure 5.9). We observed a total increase of 6.8% in cumulative LA_{ratio} for lakes <10 ha and the most significant decrease of almost 4.3% in LA_{ratio} for lakes >100 ha.

The isolated permafrost zone experienced the most pronounced lake changes in the YK Delta similar to that observed in the continuous permafrost zone with a net loss of lake surface area by 6.9% (-3150.6 ha or -38.6 ha/100 km^2) but we observed a net increase in lake number by 13.4% (829 lakes or 10.2 lakes/100 km^2) (Table 5.3, Figure 5.7). The largest increase in lake

number and lake area of 17.9% (942 lakes or 11.5 lakes/100 km^2) and 10.5 % (1721.2 ha or 21.1 ha/100 km^2) respectively, were observed for lakes <10 ha. In contrast, the largest decrease in both lake number and area of 29.2% (-14 lakes or -0.2 lakes/100 km^2) and 29.9% (-2382.8 ha or -29.2 ha/100 km^2), respectively, were observed for lakes >100 ha. We observed a decrease in number of lakes of 11% (-87 lakes or -1.1 lakes/100 km^2) for lakes in the 10-50 ha size class and 15.2% (-12 lakes or -0.1 lakes/100 km^2) for lakes in the 50-100 ha size class. Similarly, the total surface area decreased by 11.1% (-1745.2 ha or -21.4 ha/100 km^2) for lakes in the 10-50 ha size class and 13.9% (-742.9 ha or -9.1 ha/100 km^2) for lakes in the 50-100 ha size class (Table 5.3, Figure 5.7).

5.6. Discussion

5.6.1. Changes in lake distribution in study sites

The overall decrease in lake area and increase in lake number in Beringia, Central Seward Peninsula and Selawik can be explained by drainage patterns that we observed in these regions. We found that many big lakes >10 ha drained partially creating several small remnant ponds, which increased the number of small lakes in the region even though the total lake surface area in the region decreased. Among these three sites, Beringia experienced the largest loss in lake surface area due to drainage of 20 lakes >100 ha in contrast to Central Seward Peninsula and Selawik, where only 2 lakes >100 ha drained. Recently, Jones et al. (2011) used high resolution imagery to show an increase in drainage rate for larger lakes in the Cape Espenberg lowland of the Beringia region since 1978 compared to the period 1950-1978, resulting in a similar pattern in which total lake surface area is decreasing yet the total lake abundance is increasing. A similar pattern of increased lake number due to partial drainage of large lakes despite a net decline in lake area was reported from northwestern Siberia (Karlsson et al., 2014).

In the eastern delta region of Selawik, we observed expansion of water channels connecting multiple large lakes, which in the analysis is counted as a single water body. Therefore, Selawik gained more surface area for lakes >100 ha. In contrast, there was a net decline in total lake surface area in Selawik despite this expansion due to extensive drainage of lakes <100. Consequently, because of partial drainage of such lakes, the number of small remnant lakes (<10 ha) increased. Complete drainage (more than 90% lake area loss) of a significant number of lakes

<10 ha was also observed resulting in a net decrease of area for lakes <10 ha unlike other regions where both number and area of such small lakes increased. Roach et al. (2013) in their analysis of Landsat images for the period 1985-86 and 2007-2009 have reported similar patterns of net lake area decline for Selawik. They estimated a net decline in lake area of 0.81% per year and projected that the lake area could decline by 33.3% in 50 years.

Baldwin Peninsula, Kobuk Delta and YK Delta experienced an overall increase in total lake surface area due to formation of many new small lakes (<10 ha) and very large lakes (>100) due to both drainage and expansion respectively. Both expansion of existing water bodies <1 ha as well as formation of remnant lakes due to drainage of larger lakes accounted for a large increase in area and number of small lakes. In Baldwin Peninsula, expansion of such small water bodies was more prominent. There we identified a large number of new very small lakes particularly <5 ha that increased the number of lakes <10 ha significantly. In Kobuk Delta and YK Delta, the formation of remnant ponds due to drainage of large lakes was the major driver for an increased abundance of smaller lakes (<10 ha). Similar to the Selawik delta region, expansion of very large lakes (>100 ha) in Kobuk Delta was due to expansion of existing water channels that connected a network of lakes in the delta region.

The observations indicate that both lake expansion and drainage are phenomenon ongoing in parallel in western Alaska. Lakes in this permafrost region are highly dynamic both spatially and temporally. Drainage and expansion may offset each other in some locations but the identified regional trends suggest that a shifting of the regional lake abundance and distribution into a certain direction (i.e., net lake area loss) is not just a future scenario but is already happening now with significant pace. Many other studies suggest similar trends for smaller study regions in various permafrost regions (Yoshikawa and Hinzman, 2003; Mars and Houseknecht, 2007; Jones et al., 2011; Chen et al., 2014; Karlsson et al., 2014). Jones et al. (2011) found that thermokarst lakes, as a result of permafrost degradation in the 700 km^2 study region on the northern Seward Peninsula, are actively expanding at rates of 0.35 to 0.39 m/year, and due to the rapid expansion many lakes were draining at rates from 2.2 lakes/year to 2.3 lakes/year in 1950/51 to 1978 and 1978 to 2006/07, respectively. These expansion-driven dynamics led to net lake area decline in the northern Seward Peninsula, because many large lakes were lost. In Siberia, Karlsson et al. (2014) also found lakes appearing and disappearing with high numbers of drainage events. They

reported both increase and decrease in net lake area and abundance between two different time periods (1973 and 1987-1988, 1987-88 and 2007-2009) with a net decline in lake area in most of their 144,300 km^2 study region.

5.6.2. Lake change in different permafrost zones across western Alaska

The average lake area decline observed in various permafrost zones does not represent the trend of individual sites due to spatial heterogeneity in lake characteristics. This agrees with the previous finding that permafrost extent of the region alone does not determine the direction of lake change (Riordan et al., 2006; Roach et al., 2013; Karlsson et al., 2014; Chen et al., 2014).

Smith et al. (2005) reported an overall lake area increase in the continuous permafrost zone and a decrease in the non-continuous permafrost zones across their study region covering an area of 515,000 km^2 in Siberia for the time period between the 1970s and 2004. In the whole study domain, on average the continuous permafrost zone experienced a total lake surface area loss during the time period 1970s to 2014. A decrease or negligible change in lake area has been reported from other regions of Alaska and Siberia for smaller study regions in the continuous permafrost zone (Riordan et al., 2006; Labrecque et al., 2009; Jones et al., 2009; Jones et al., 2011). We also noticed an overall increase in lake area for the sporadic permafrost zone located in the YK Delta in contrast to Smith et al. (2005) who found lake loss dominated the sporadic permafrost zone of West Siberia. These differences in observations show that the direction of lake area change can be variable from one region to another.

The net decrease in lake area in the continuous permafrost zone in the study was due to major lake drainage events in Beringia and Selawik even though total lake area increased in three out of five of the study regions located in the continuous permafrost zone. This indicates higher lake expansion rates in these three continuous permafrost regions (Baldwin Peninsula, Central Seward Peninsula and Kobuk Delta). Fine-scale studies (Jones et al., 2011) suggest that lakes also expanded during the observation period in the continuous permafrost zone of Beringia. Using Landsat data we mostly were not able to detect these changes in the observation period 1970s - 2014. Expansion of lakes is a common phenomenon in the continuous permafrost zone that may result in lake drainage via shoreline breaching (Mackay 1988; Burn and Smith 1990; Jones et al., 2011). Plug et al. (2008) documented an overall increase in total lake area between 1978-1992 and a decrease between 1992-2001 in the continuous permafrost zone distributed

across Tuktoyaktuk, Canada. Initial thaw of thick ice rich permafrost in the continuous permafrost zone may lead to land subsidence creating thermokarst ponds and lakes. Further permafrost degradation leads to expansion of lakes both vertically and horizontally increasing the chances for drainage (Mackay, 1988; Jones et al., 2011). Several studies have discussed lateral drainage of thermokarst lakes in continuous permafrost due to bank overflow, subsequent development of the drainage network by ice wedge degradation, headward erosion, bank overflow, or lake tapping by another water body such as lake, river or sea (Hopkins, 1949; Mackay, 1988; Hinkel et al., 2007; Marsh et al., 2009; Jones et al., 2011; Grosse et al., 2013; Jones and Arp, 2015). Therefore, it is possible that areas of relatively stable continuous permafrost show lake change to be variable depending on the stages of thaw.

In Alaska, declining lake surface area was reported from different regions underlain by discontinuous permafrost (Yoshikawa and Hinzman, 2003; Riordan et al., 2006; Rover et al., 2012; Chen et al., 2014) Lake change trends in this study largely agree with previous findings, suggesting that lake shrinkage is becoming increasingly common in areas of discontinuous permafrost. In a warmer Arctic, the southern portions of the continuous permafrost zone will transition into non-continuous permafrost (Jafarov et al., 2012) where lake shrinkage may then become a more prominent phenomenon than lake expansion (Yoshikawa and Hinzman, 2003; Smith et al., 2005).

Distribution and structure of hydrological networks and patchy permafrost distribution in the sporadic permafrost zone of the YK Delta could be a potential driver for an increase in total lake surface area. Hydrology in low-lying delta regions is very dynamic with an expansive and complicated web of water channel distributaries both at the surface and in the subsurface. In the sporadic permafrost zone, underground connectivity of lakes to the groundwater system is enhanced and recharge from better-developed ground water aquifers may play a more important role for lake water levels and areas than in more continuous permafrost regions. For the YK Delta it could be a very likely scenario similar to the one proposed by Chen et al. (2014) for the Yukon Flats that permafrost distribution beneath lakes and the hydraulic head gradient of lakes relative to the groundwater table are a potential driver for heterogeneous though clustered spatial patterns of lake changes. In the isolated permafrost zones of the study region lake area loss is again larger than lake expansion, because numerous large lakes are located close to water

channels drained by stream or river tapping. Based on the Landsat observations, we observed that formation of new drainage channels or expansion of pre-existing water channels promoted lake loss. In addition, headward erosion of stream channels and erosion of narrow land between coastal lakes and the sea caused nearby lakes to drain. Loss of lakes due to coastal erosion has been described earlier for the Alaska North Slope (Jones and Arp, 2015; Hinkel et al., 2007).

It is also important to consider how different sized lakes are behaving in different regions to better understand the dynamics of lake area change. We noticed an increase in total area and number of small lakes (<10 ha) in most regions (except in the discontinuous zone of Selawik) and an increase in area of very large lakes (>100 ha) in three out of five regions in the continuous permafrost zone, two out of four regions in the discontinuous zone and the sporadic permafrost zone despite reduced lake number in some cases. But lakes in size classes 10-50 ha and 50-100 ha showed a consistent drainage pattern in all regions except in the sporadic permafrost zone, which indicates that, overall, large lakes are more vulnerable to drainage. One of the primary reasons for the increase in abundance of small lakes is due to drainage of such large lakes whereas expansion of very large lakes in some regions indicates ongoing degradation of surrounding permafrost or changes in local hydrology that likely altered the lake water budget. Consequently, we observed a noticeable increase in lake number and lake area ratio for smaller lakes. However, the area ratio varied from region to region for larger lakes indicating different drainage and expansion patterns among different sized lakes. Therefore, it is important to note that these drainage and expansion events offset each other eventually shifting the overall lake change pattern to a certain direction. Since there is spatial as well as temporal variability in lake area change across different regions, an effort to assess lake area change and its cause using high spatial and temporal resolution imagery should be conducted for future planning and decision-making.

5.6.3. Factors influencing lake area changes

Landscape and substrate characteristics beneath and around the lakes can additionally dictate the lake drainage and expansion patterns. For instance, trends in lake area change are more variable in areas dominated by surface geological settings where coarse, porous and ice-poor sediment allows both drainage and refill depending on the surrounding or neighboring landscape characteristics and hydrological system, which we have observed in the delta lake regions. This

is in agreement with previous studies investigating regions with such deltaic or alluvial terrace substrates (Burn, 2002; Jorgenson and Shur, 2007; Roach et al., 2013). In contrast, ice-rich fine-grained silty soil can promote water ponding resulting in thermokarst development, lake expansion, and later drainage as observed in ice-rich loess areas, for example in Beringia.

There are several other climate-induced factors that interact with each other influencing permafrost dynamics and subsequently lake area characteristics in permafrost regions. Several studies have analyzed influences of ice-jam flooding, storm floods, changes in water balance, terrestrialization, precipitation, temperature, and climate on lake habitat characteristic changes (Riordan et al., 2006; Jones et al., 2009; Labrecque et al., 2009; Turner et al., 2010; Jones et al., 2011; Roach et al., 2011; Chen et al., 2013; Chen et al., 2014; Terenzi et al., 2014). Some studies have indicated that patterns of precipitation and evaporation are the primary factors influencing water budgets and areal extent of lakes in particular in highly continental permafrost regions (Riordan et al., 2006; Plug et al., 2008; Jones et al., 2009; Labrecque et al., 2009; Roach et al., 2011; Bosikov, 1998). Similarly, inter-annual variability of ice-jam flooding events have been identified as another factor affecting lake area changes (Chen et al., 2014), which in turn is controlled by a number of climatic factors. Wildfire can also have an impact on the local vegetation cover and ground ice content eventually affecting local lake area distribution (Roach et al., 2013).

All these factors play roles in altering local permafrost dynamics, which eventually influence regional lake distribution and lake habitat characteristics. Changes in lake characteristics in response to changes in surrounding permafrost terrain largely depend on the local ground ice-content and geomorphic characteristics (Jorgenson and Shur, 2007). For instance, in a warming climate regions of ice-rich permafrost may first experience an increase in lake area followed by increased drainage events. In contrast thawing of ice-poor permafrost currently in coarse sandy regions can lead to vertical lake drainage through talik. The changes in the neighboring areas of lake habitat and their distance from rivers and streams can have an additional impact (Chen et al., 2013; Roach et al., 2013). For example, lakes with channel connections to river systems may have a lower probability of drainage (Chen et al., 2013; Roach et al., 2013). However, if a lake is close to a stream then a change in stream hydrology could breach the land between the lake and the stream cut resulting in lake drainage (Hinkel et al.,

2007). Tapping of lakes by coastal erosion is another mechanism of lake drainage (Mars and Houseknecht, 2007; Jones et al., 2008; Arp et al., 2010). We noticed such lake tapping events in the YK Delta. In some cases, water channels connecting multiple lakes may expand as permafrost thaws and sediment is eroded, merging the lakes. We commonly observed this process in the deltas of the Kobuk Delta and Selawik regions. Continued permafrost degradation can eventually lead to lake shrinkage, but in areas with a complex hydrological network where lake water balance is controlled by the surrounding rivers and other larger water systems, changes in lake area can be highly variable. Therefore, future field and modeling studies of mechanisms and feedbacks of hydrological dynamics and their response to climate change are required in order to fully understand changes in lake habitat characteristics.

5.6.4. Broader implications

A widespread lake area and lake number loss is already happening in western Alaska. Permafrost is one of the major components that maintain the lake distribution in this region. However, permafrost models project extensive permafrost loss across western Alaska in a warming climate (Jafarov et al., 2012). Therefore, an increased number of lake drainage events and net drying of soil as subsurface permafrost thaws are expected, which will have a direct impact on the regional lake habitat characteristics. Lakes constitute a large portion of the wetlands and deltas in western Alaska, which are also major biodiversity hotspots. Therefore, changes in lake habitat characteristics will have a huge impact on waterfowl, and other aquatic and terrestrial wildlife that largely depend on the wetlands and deltas for breeding and feeding during open-water seasons (Clark et al., 2010; Marcot et al., 2015). Similarly during winter when lakes freeze, shifting of lake ice characteristics from floating-ice to grounded-ice in winter due to a decline in water level can immensely affect the aquatic life (Arp et al., 2011). Such changes will directly affect fisheries and hunting opportunities as well as accessibility to water sources for village communities living a subsistence lifestyle (Alessa et al., 2008; Eisner et al., 2009; Jones et al., 2009).

Ongoing changes in the lakes will also have a positive feedback on the surrounding permafrost. While permafrost degradation can change lake habitat characteristics drastically through initiation of new lakes by thermokarst processes as well as through growth and drainage of existing lakes, the presence of lakes depending on their dimensions can alter the ground

thermal properties and further degrade the confining permafrost (West and Plug et al., 2008). On the contrary, permafrost aggradation or reactivation of polygonal ice-wedge networks could eventually take place on drained lake basins in the cold climate regions located in northwestern Alaska such as Seward Peninsula (Hopkins, 1949; Mackay and Burn, 2002; Ling and Zhang, 2004; Bockheim and Hinkel, 2012). Drainage of lakes and initiation of ponding on low-centered ice wedge polygons at the later stage of post-drainage succession could also result in formation of wetlands and a new thermokarst lake cycle (Hinkel et al., 2003; Jones et al., 2012, Regmi et al., 2012). Such repeated cycles of lake formation and drainage on millennial scales form complex landscapes comprising a mosaic of different generations of lakes and drained basins at various stages of post-drainage succession that affect other terrestrial and hydrological characteristics of the region. It has been found that young or first generation and later generation lakes are different in terms of depth, morphology, buried ice content and soil organic matter (West and Plug, 2008; Brosius et al., 2012; Kessler et al., 2012), which has a major implication on aquatic habitat characteristics and biogeochemical cycling. However, in western Alaska, predicted increases in temperature could restrict regeneration of permafrost in drained lake basins and continued thawing of ice-rich permafrost present in the original sediment more likely transform the current landscape into the one occupied with a larger number of later generation lakes and a drier environment.

Another concern is the impact on the mobilization of permafrost-stored soil organic carbon due to changes in lake characteristics, particularly of thermokarst origin, and its feedback on the regional carbon cycle and global carbon budget (Walter et al., 2007b; Tranvik et al., 2009; Schneider von Deimling et al., 2015). Expansion of thermokarst lakes along the margin as well as formation of taliks underneath lakes due to thawing of permafrost can release organic matter into anaerobic lake bottoms enhancing methane production and emission (Walter et al., 2006; Kessler et al., 2012). Besides, changes in lake morphology will have an impact on lake methane dynamics (Bastviken et al., 2004). On the other hand, if lakes are draining at a landscape scale, establishment of terrestrial vegetation and later peat accumulation on lake basins following drainage have the potential to act as a carbon sink on a regional scale (Jones et al., 2012; Klein et al., 2013). The estimation of a net carbon budget associated with lakes is a challenging task as it is dependent on the rate and type of lake change patterns, history of lake basins, and other

environmental and climatic factors (Zona et al., 2010; Kessler et al., 2012; Walter Anthony et al., 2014).

5.7. Conclusion

The assessment of lake distribution and changes using Landsat images from 1972-75 to 2013-14 in major lake-rich regions covering an area of 68,830 km^2 in western Alaska shows widespread lake number and lake area loss. We found that many large lakes drained and shrunk in area while the abundance of lakes <10 ha increased significantly due to partial drainage of large lakes creating numerous remnant ponds. Though lake drainage dominated most portions of the region, lake area increase was observed in some regions of the continuous permafrost zone. Lake area shrinkage dominated the non-continuous permafrost zones except in the sporadic zone located in the YK delta region. This study shows that both lake expansion and drainage are phenomena ongoing in parallel in western Alaska, which may offset each other or shift the regional lake change pattern in a certain direction. This further demonstrates that the selection of the specific study region can have an impact on lake change findings such that a fine-scale observation of small study regions can show spatial heterogeneity in lake area loss and gain, but only a broad-scale observation of large study regions can show the net effect. The identified regional trends suggest that a shift of the regional lake abundance and distribution to a negative direction (i.e., net lake area loss) is not just a future scenario but is already happening now at a significant pace and confirms projections of landscape scale drying in a warming Arctic. Therefore, an increased number of drainage events is expected in the continuous permafrost as climate gets warmer and surface permafrost begins to degrade or even becomes discontinuous in extent. Additionally, as permafrost becomes less stable, the influence of other factors such as surficial geology and landscape characteristics such as topography, hydrology, and cryolithology likely will magnify the variability of lake area change. To increase the accuracy of projections, other important climatic and non-climatic factors such as precipitation, temperature, connectivity, lake ice regime, and surface topography need to be taken into account in further studies. Changes in lake dynamics and characteristics have a measureable impact on the hydrological and terrestrial dynamics, surrounding permafrost, biogeochemical cycling, wildlife habitats, and human communities living in remote villages in western Alaska. Efforts to assess lake area change and

their causes in high northern latitudes should be continued for future planning and decision making.

5.8. Acknowledgement

This research was supported by the Western Alaska Landscape Conservation Cooperative project WA2011-02, NASA NNX11AH20G, and ERC #338335.

5.9. Figures

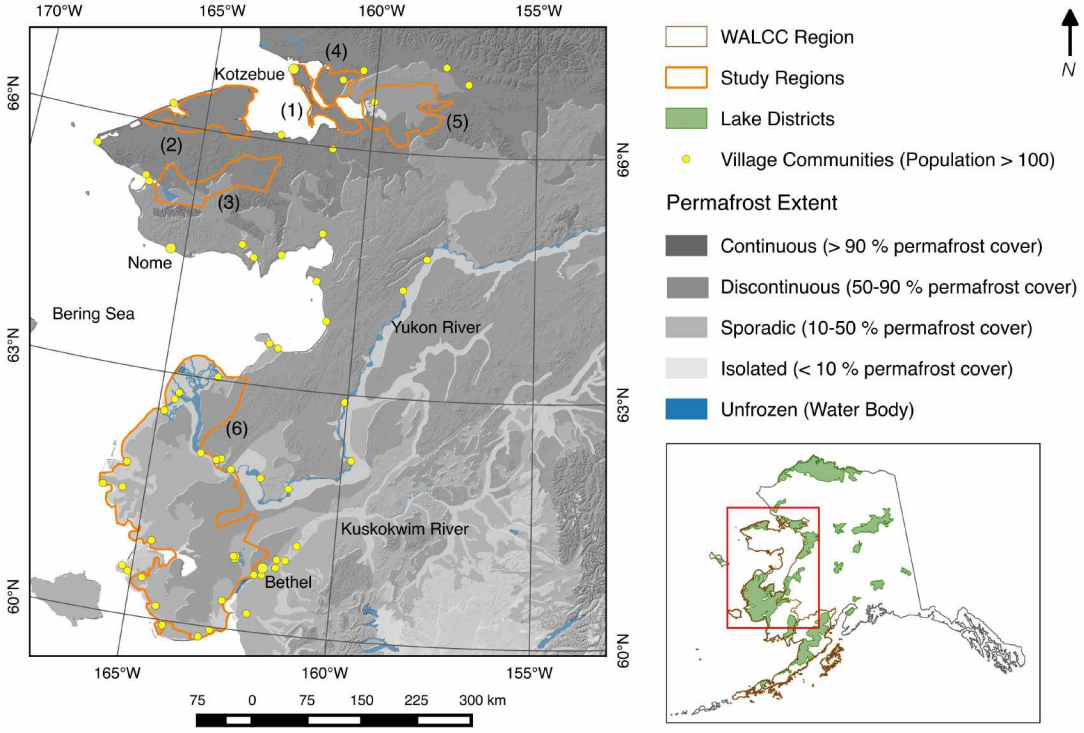

Figure 5.1. Study areas in the northern and central Western Alaska LCC Region with permafrost extent types and village locations in the region (with population > 100, major villages Kotzebue, Nome and Bethel are shown in large yellow dots): (1) Baldwin Peninsula, (2) Beringia, (3) Central Seward Peninsula, (4) Kobuk Delta, (5) Selawik, and (6) Yukon-Kuskokwim Delta.

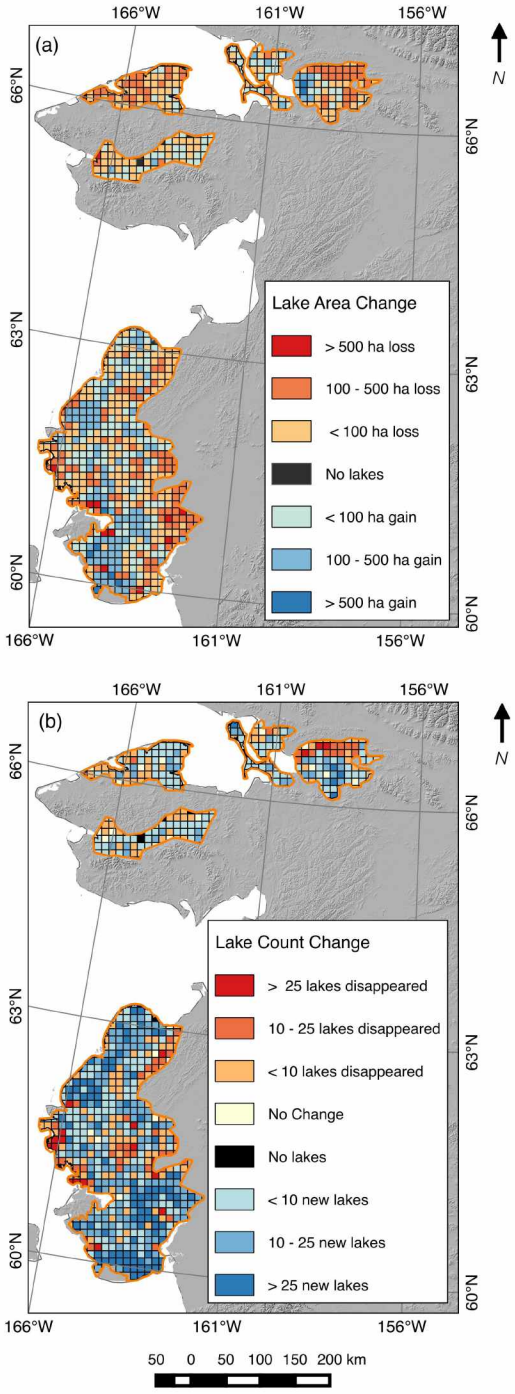

Figure 5.2. Maps showing gridded (10x10 km = 100 km^2 grid cells) lake area and lake count change.

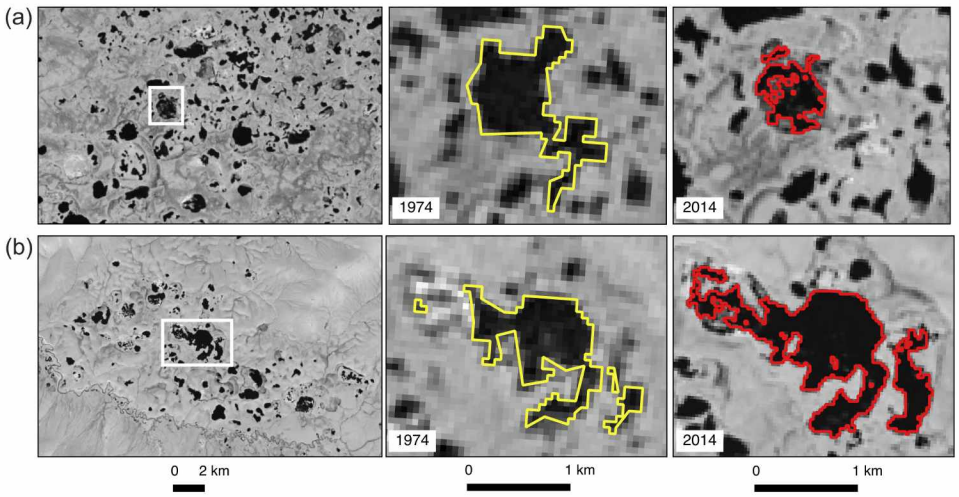

Figure 5.3: Examples of (a) lake area shrinkage or partial lake drainage in the Selawik lake-rich region and (b) lake area expansion in the Baldwin Peninsula lake-rich region.

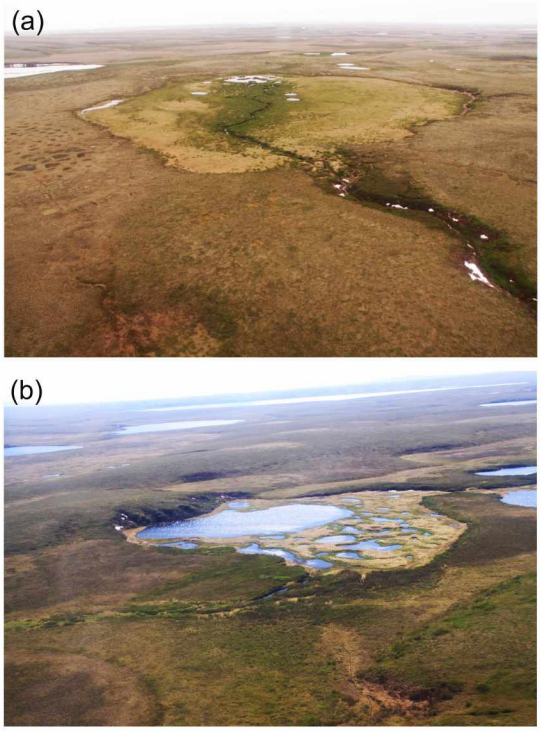

Figure 5.4. Field photos from the Beringia study region showing lateral drainage of lakes caused by formation of a drainage channel. (a) Photo showing a complete drainage, note the deep drainage channel and (b) showing partial drainage (Photo credit G. Grosse).

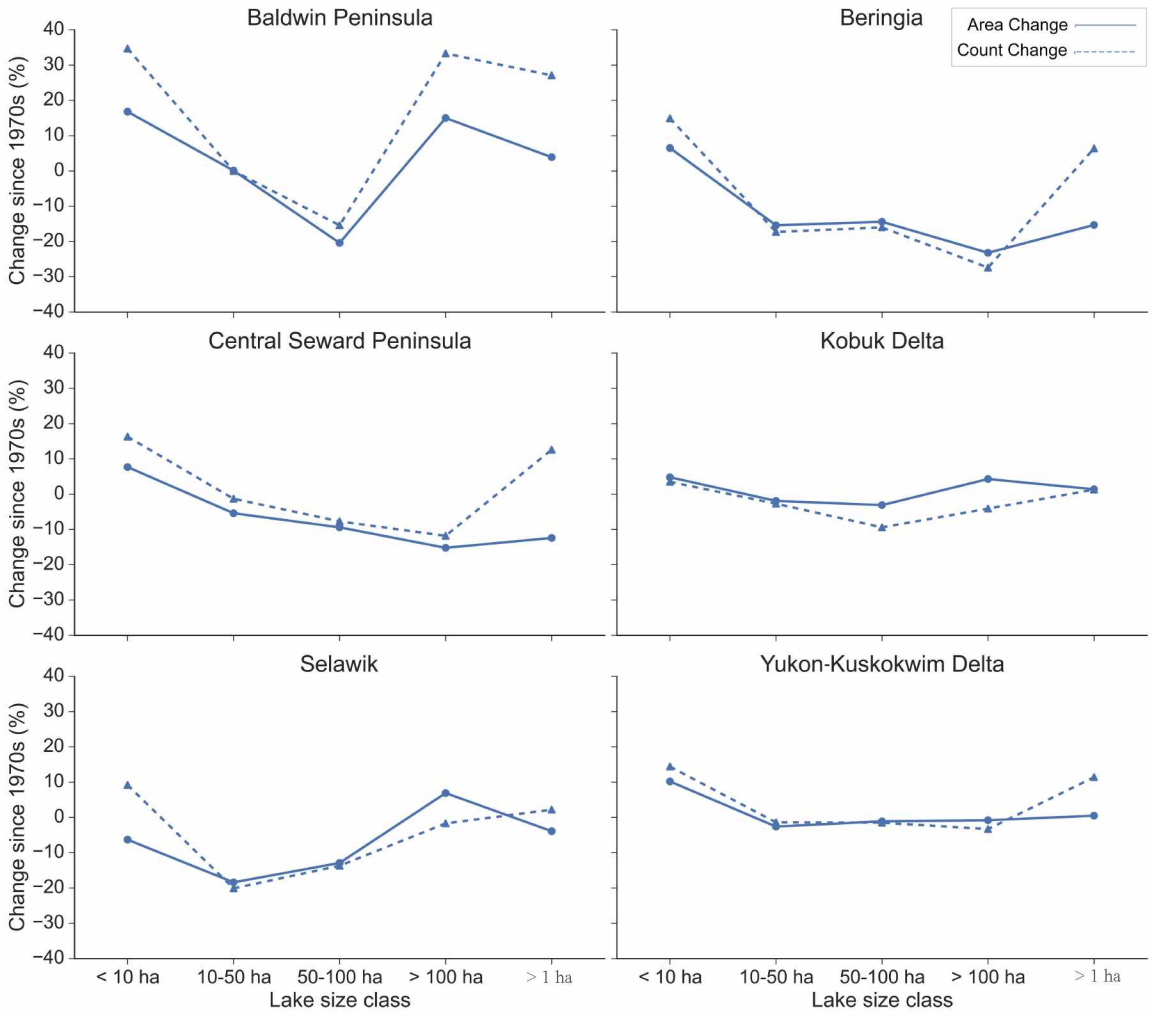

Figure 5.5. Percent of total area and lake number change since the 1970s in different study regions.

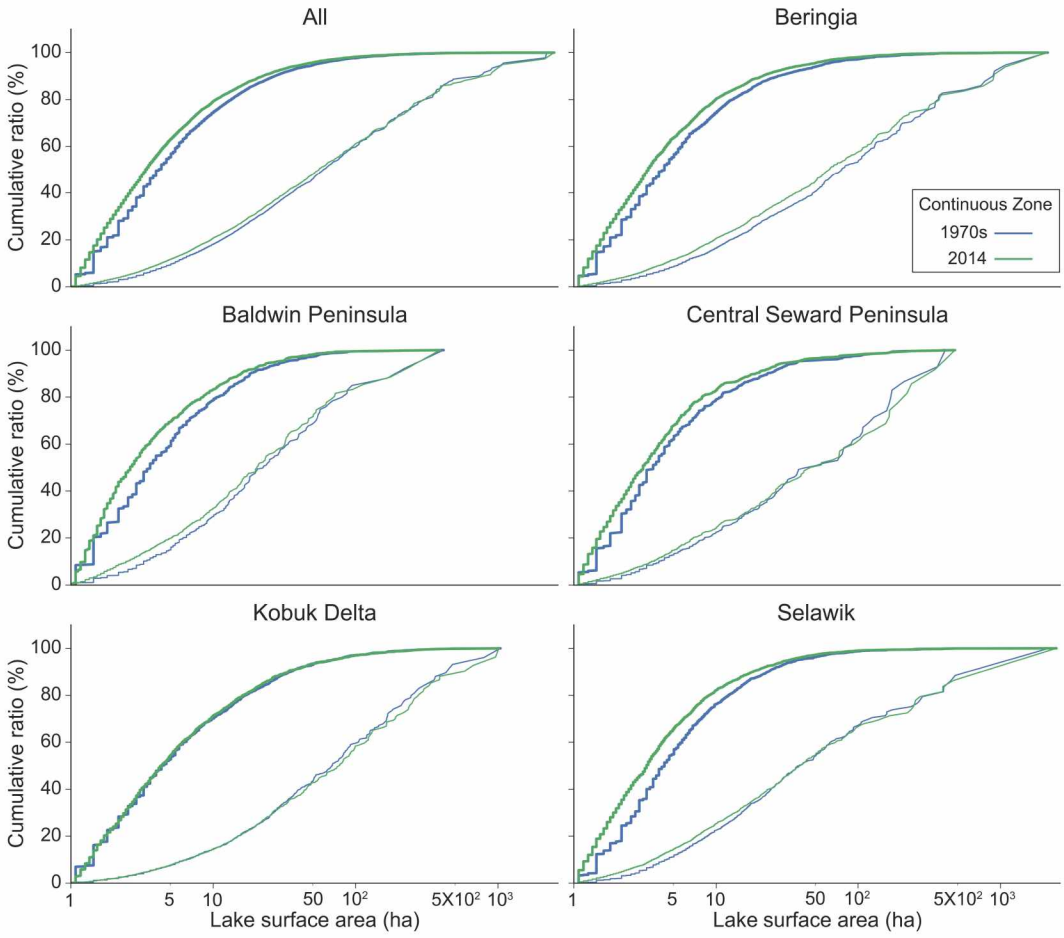

Figure 5.6. Cumulative ratio of number of lakes to total lake number (thicker curves) and cumulative ratio of lake surface to total lake coverage area available (thinner curves) within the continuous permafrost zone.

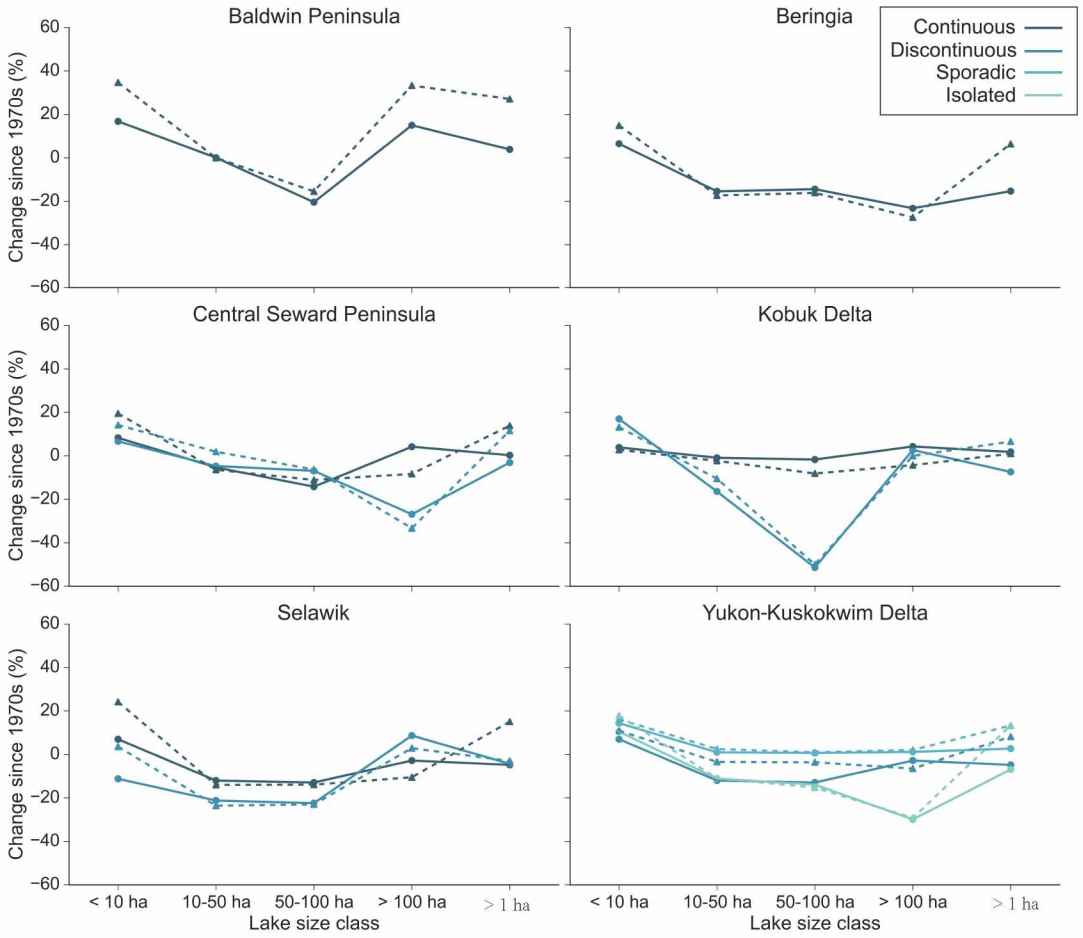

Figure 5.7. Percent of total area change (solid line) and lake number change (dotted line) since the 1970s in different permafrost zones located in each study region.

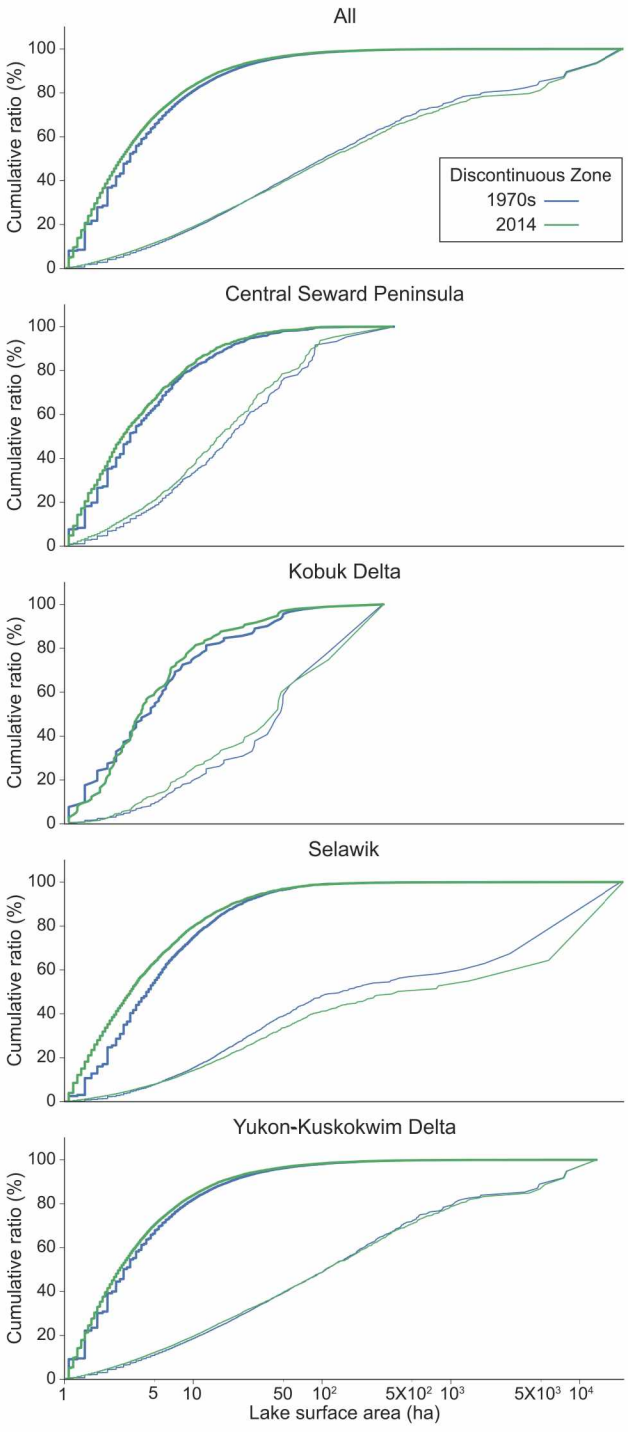

Figure 5.8. Cumulative ratio of number of lakes to total lake number (thicker curves) and cumulative ratio of lake surface to total lake coverage area available (thinner curves) within the discontinuous permafrost zone.

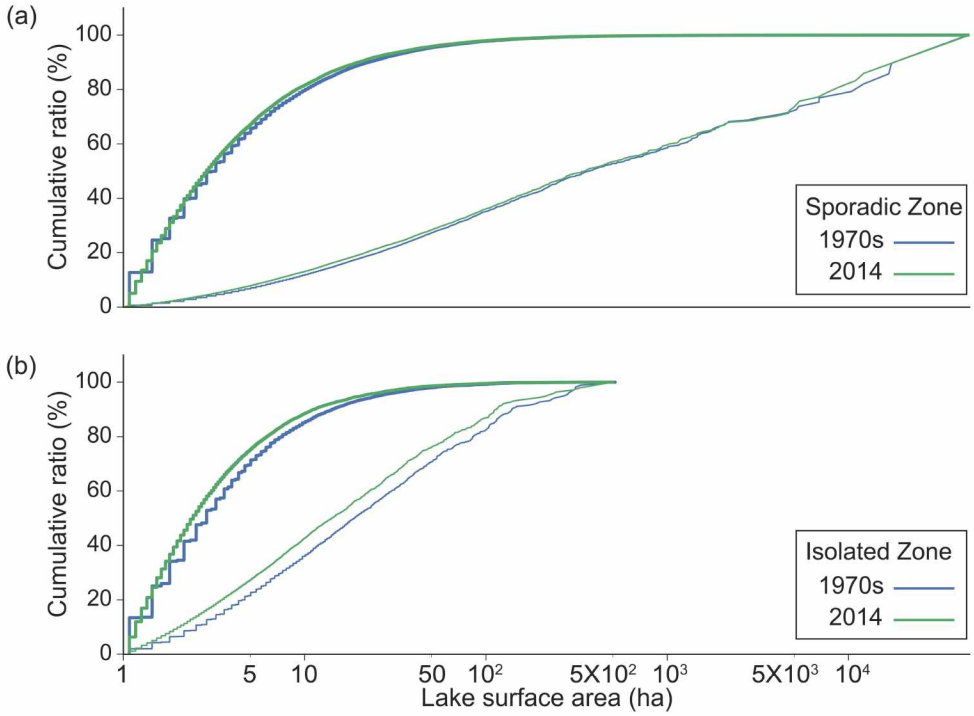

Figure 5.9. Cumulative ratio of number of lakes to total lake number (thicker curves) and cumulative ratio of lake surface to total lake coverage area available (thinner curves) within the (a) sporadic and (b) isolated permafrost zones, both located in YK Delta.

5.10. Tables

Table 5.1. Lake distribution, limnicities, and lake change for all six lake-rich study regions.

		1970s			2014			Change				
Focus Regions	Size Class	Count	Surface Area (ha)	Limnicity	Count	Surface Area (ha)	Limnicity	% Count Change*	% Area Change*	Count Change /100 km^2	Area Change (ha)/100 km^2	Change Pattern
Baldwin Peninsula	< 10 ha	447	1542.0	1.0	602	1801.6	1.2	34.7	16.8	10.1	16.9	Many new small lakes
	10-50 ha	106	2098.7	1.4	106	2101.4	1.4	0.0	0.1	0.0	0.2	No significant change
	50-100 ha	13	868.8	0.6	11	691.7	0.5	-15.4	-20.4	-0.1	-11.6	Drainage of big lakes and expansion
	> 100 ha	3	800.7	0.5	4	920.4	0.6	33.3	15.0	0.07	7.8	Expansion or formation by fusion of smaller lakes
	All lakes	569	5310.2	3.5	723	5515.1	3.6	27.1	3.9	10.1	13.4	Expansion dominates
Beringia	< 10 ha	1866	6771.8	1.2	2144	7210.0	1.3	14.9	6.5	5.1	8	New lakes
	10-50 ha	491	9914.9	1.8	406	8389.2	1.5	-17.3	-15.4	-1.6	-28	Drainage
	50-100 ha	81	5275.1	1.0	68	4516.3	0.8	-16.0	-14.4	-0.2	-13.9	Drainage of big lakes
	> 100 ha	73	19294.8	3.5	53	14823.0	2.7	-27.4	-23.2	-0.4	-82	Drainage of big lakes
	All lakes	2511	41256.6	7.6	2671	34938.5	6.4	6.4	-15.3	2.9	-115.9	Drainage dominates
Central Seward Peninsula	< 10 ha	1133	3873.2	0.7	1318	4171.0	0.7	16.3	7.7	3.1	5.0	Many new lakes
	10-50 ha	237	4912.7	0.8	234	4646.8	0.8	-1.3	-5.4	-0.1	-4.5	Drainage
	50-100 ha	26	1943.3	0.3	24	1760.3	0.3	-7.7	-9.4	-0.03	-3.1	Drainage of big lakes
	> 100 ha	17	42074.8	7.1	15	35683.7	6.0	-11.8	-15.2	-0.03	-107.6	Overall drainage of big lakes and also expansion
	All lakes	1413	52804.0	8.9	1591	46261.9	7.8	12.6	-12.4	3.0	-110.2	Drainage dominates

Table 5.1 continued

Focus Regions	Size Class	1970s Count	1970s Surface Area (ha)	1970s Limnicity	2014 Count	2014 Surface Area (ha)	2014 Limnicity	Change % Count Change*	Change % Area Change*	Change Count Change /100 km^2	Change Area Change (ha)/100 km^2	Change Pattern
Kobuk Delta	< 10 ha	1152	4071.1	2.1	1192	4265.4	2.2	3.5	4.8	2.1	10.1	New lakes
	10-50 ha	373	8181.2	4.3	363	8029.0	4.2	-2.7	-1.9	-0.5	-7.9	Drainage
	50-100 ha	64	4410.3	2.3	58	4272.4	2.2	-9.4	-3.1	-0.3	-7.2	Drainage of big lakes and also expansion
	> 100 ha	49	11189.2	5.8	47	11668.6	6.1	-4.1	4.3	-0.1	24.9	Expansion is prominent, connected by channels
	All lakes	1638	27851.7	14.5	1660	28235.4	14.7	1.3	1.4	1.1	19.9	Expansion dominates
Selawik	< 10 ha	3793	14630.1	2.3	4142	13715.2	2.2	9.2	-6.3	5.5	-14.4	Drainage of small lakes
	10-50 ha	1091	22318.9	3.5	872	18212.7	2.9	-20.1	-18.4	-3.4	-64.6	Drainage of big lakes
	50-100 ha	131	8946.5	1.4	113	7796.4	1.2	-13.7	-12.9	-0.3	-18.1	Drainage of big lakes
	> 100 ha	59	40747.8	6.4	58	43560.0	6.9	-1.7	6.9	0.02	44.3	Expansion of big lakes, connected by channels
	All lakes	5074	86643.2	13.6	5185	83284.3	13.1	2.2	-3.9	1.7	-52.9	Drainage dominates
Yukon Kuskokwim Delta	< 10 ha	37080	117058.2	2.5	42434	128965.9	2.8	14.4	10.2	11.5	25.5	New lakes
	10-50 ha	6754	139691.8	3.0	6658	136058.7	2.9	-1.4	-2.6	-0.2	-7.8	Drainage
	50-100 ha	937	64904.8	1.4	923	64196.2	1.4	-1.5	-1.1	-0.03	-1.5	Drainage
	> 100 ha	886	437292.4	9.4	857	433648.8	9.3	-3.3	-0.8	-0.1	-7.8	Drainage
	All lakes	45657	758947.0	16.3	50872	762869.6	16.3	11.4	0.5	7.6	5.7	Not significant change in total lake area. But distinct sub-regional lake change patterns, loss or gain, exist.

Table 5.2. Lake distribution, limnicities, and lake change for all four permafrost zones.

		1970s			2014			Change			
Permafrost extent	Size Class	Count	Surface Area (ha)	Limnicity	Count	Surface Area (ha)	Limnicity	% Count Change*	% Area Change*	Count Change/100 km^2	Area Change (ha)/100 km^2
Continuous	< 10 ha	4879	17703.2	0.8	5683	18958.9	0.9	16.5	7.1	5.4	8.5
	10-50 ha	1322	27268.3	1.2	1183	24872.9	1.1	-10.5	-8.8	-0.9	-16.2
	50-100 ha	201	13553.4	0.6	175	12133.3	0.5	-12.9	-10.5	-0.2	-9.6
	> 100 ha	154	39383.0	1.8	130	35415.5	1.6	-15.6	-10.1	-0.2	-26.8
	All lakes	6556	97907.9	4.4	7171	91380.6	4.1	9.4	-6.7	4.2	-44.2
Discontinuous	< 10 ha	18576	60978.3	1.0	20437	62526.0	1.0	10.0	2.5	8.2	6.8
	10-50 ha	3572	73315.8	1.2	3307	67400.6	1.1	-7.4	-8.1	-1.2	-26.0
	50-100 ha	463	31838.1	0.5	428	29664.6	0.5	-7.6	-6.8	-0.2	-9.6
	> 100 ha	395	168386.7	2.8	372	169431.7	2.8	-5.8	0.6	-0.1	4.6
	All lakes	23006	334518.9	5.5	24544	329022.9	5.4	6.7	-1.6	6.8	-24.2
Sporadic	< 10 ha	16484	51819.7	1.1	19147	59280.6	1.3	16.2	14.4	14.6	41.0
	10-50 ha	3259	68415.4	1.5	3341	69114.8	1.5	2.5	1.0	0.5	3.8
	50-100 ha	497	34797.5	0.7	502	35044.5	0.8	1.0	0.7	0.03	1.4
	> 100 ha	471	286281.7	6.1	481	289592.6	6.2	2.1	1.2	0.1	18.2
	All lakes	20711	441314.4	9.5	23471	453032.5	9.7	13.3	2.7	15.2	64.4
Isolated	< 10 ha	5251	16354.4	0.4	6193	18075.6	0.4	17.9	10.5	11.5	21.1
	10-50 ha	791	15759.0	0.3	704	14013.9	0.3	-11.0	-11.1	-1.1	-21.4
	50-100 ha	79	5353.8	0.1	67	4610.9	0.1	-15.2	-13.9	-0.1	-9.1
	> 100 ha	48	7979.8	0.2	34	5596.0	0.1	-29.2	-29.9	-0.2	-29.2
	All lakes	6169	45447.0	1.0	6998	42296.4	0.9	13.4	-6.9	10.2	-38.6

Table 5.3. Lake change for all four permafrost zones located in each lake-rich study region

Focus Regions	Size Class	Continuous PF Extent		Discontinuous PF Extent		Sporadic PF Extent		Isolated PF Extent	
		% Count Change*	% Area Change*	% Count Change*	% Area Change*	% Count Change*	% Area Change*	% Count Change*	% Area Change*
Baldwin Peninsula	< 10 ha	34.7	16.8						
	10-50 ha	0.0	0.1						
	50-100 ha	-15.4	-20.4						
	> 100 ha	33.3	14.9						
	All lakes	27.1	3.9						
Beringia	< 10 ha	14.9	6.5						
	10-50 ha	-17.3	-15.4						
	50-100 ha	-16.0	-14.4						
	> 100 ha	-27.4	-23.2						
	All lakes	6.4	-15.3						
Central Seward Peninsula	< 10 ha	19.5	8.3	14.2	6.7				
	10-50 ha	-6.4	-5.3	1.9	-4.7				
	50-100 ha	-11.1	-14.2	-6.3	-6.9				
	> 100 ha	-8.3	4.2	-33.3	-26.9				
	All lakes	13.9	0.3	11.6	-3.1				
Kobuk Delta	< 10 ha	2.8	3.9	13.2	17.0				
	10-50 ha	-2.3	-0.9	-10.5	-16.4				
	50-100 ha	-8.1	-1.7	-50.0	-51.4				
	> 100 ha	-4.3	4.3	0.0	2.7				
	All lakes	1.0	1.8	6.6	-7.4				

Table 5.3 continued

Focus Regions	Size Class	Continuous PF Extent		Discontinuous PF Extent		Sporadic PF Extent		Isolated PF Extent	
		% Count Change*	% Area Change*	% Count Change*	% Area Change*	% Count Change*	% Area Change*	% Count Change*	% Area Change*
Selawik	< 10 ha	24.1	7.0	3.5	-11.2	----------			
	10-50 ha	-14.0	-12.0	-23.6	-21.2				
	50-100 ha	-13.9	-12.9	-23.0	-22.4				
	> 100 ha	-10.5	-2.8	2.9	8.7				
	All lakes	15.1	-4.8	-3.0	-4.3				
Yukon Kuskokwim Delta	< 10 ha	----------		10.9	7.0	16.2	14.4	17.9	10.5
	10-50 ha			-3.4	-12.0	2.5	1.0	-11.0	-11.1
	50-100 ha			-3.6	-12.9	1.0	0.7	-15.2	-13.9
	> 100 ha			-6.5	-2.8	2.1	1.2	-29.2	-29.9
	All lakes			8.2	-4.8	13.3	2.7	13.4	-6.9

5.11. Supplementary materials

Supplementary Table 5.1. Permafrost extent type and percentage coverage in each study site. This is estimated from data provided by Jorgenson et al., 2008*.

Study Regions	Permafrost Extent	Area (km^2)	Percent Coverage
Baldwin Peninsula	Continuous	1531.8	100.0
Beringia	Continuous	5452.0	100.0
	Unfrozen (Water body)	0.0	0.0006
Central Seward Peninsula	Continuous	3759.3	63.5
	Discontinuous	1863.0	31.5
	Unfrozen (Water body)	295.9	5.0
Kobuk Delta	Continuous	1597.8	88.8
	Discontinuous	201.4	11.2
Selawik	Continuous	2436.4	42.1
	Discontinuous	3355.6	57.9
Yukon-Kuskokwim Delta	Discontinuous	17328.1	38.5
	Sporadic	18191.8	40.4
	Isolated	8162.4	18.1
	Unfrozen (Water body)	1349.5	3.0

* Jorgenson, T. M., Yoshikawa, K., Kanevskiy, M., Shur, Y. L., Romanovsky, V., Marchenko, S., Grosse, G., Brown, J., Jones, B. 2008. Permafrost characteristics of Alaska. In Proceedings of the Ninth International Conference on Permafrost, Kane DL, Hinkel KM (eds). Fairbanks, AK; 121–122.

Supplementary Table 5.2. Ground ice content and percentage coverage in each study site. This is estimated from data provided by Jorgenson et al., 2008*.

Study Regions	Ground Ice Content	Area (km^2)	Percent Coverage
Baldwin Peninsula	High	746.7	48.7
	Moderate	666.3	43.5
	Low	118.8	7.8
Beringia	High	5281.7	96.9
	Moderate	140.6	2.6
	Low	29.7	0.5
	Unfrozen	0.0	0.001
Central Seward Peninsula	High	3056.1	51.6
	Moderate	1783.5	30.1
	Low	263.9	4.5
	Unfrozen	295.9	5.0
	Variable	518.9	8.8
Kobuk Delta	Moderate	1678.0	93.3
	Low	36.9	2.1
	Variable	84.3	4.7
Selawik	High	920.0	15.9
	Moderate	4108.6	70.9
	Low	763.3	13.2
Yukon-Kuskokwim Delta	High	17164.2	38.1
	Moderate	18355.8	40.8
	Low	8162.4	18.1
	Unfrozen	1349.5	3.0

* Jorgenson, T. M., Yoshikawa, K., Kanevskiy, M., Shur, Y. L., Romanovsky, V., Marchenko, S., Grosse, G., Brown, J., Jones, B. 2008. Permafrost characteristics of Alaska. In Proceedings of the Ninth International Conference on Permafrost, Kane DL, Hinkel KM (eds). Fairbanks, AK; 121–122.

Supplementary Table 5.3. Surficial deposit type and percentage coverage in each study site. This is estimated from data provided by Jorgenson et al., 2008*.

Study Regions	Deposit Type	Area (km^2)	Percent Coverage
Baldwin Peninsula	Beach	118.8	7.8
	Coarse and fine rubble	72.1	4.7
	Old marine and alluvium	594.2	38.8
	Upland loess	746.7	48.7
Beringia	Beach	29.7	0.5
	Coastal Delta	140.3	2.6
	Fine rubble	0.3	0.0
	Lake	0.0	0.0
	Upland loess	14.3	0.3
	Valley loess and alluvium	5267.4	96.6
Central Seward Peninsula	Alluvial terrace	740.9	12.5
	Coarse and fine rubble	191.0	3.2
	Coastal Delta	81.3	1.4
	Fine rubble	304.0	5.1
	Highly modified moraine	448.1	7.6
	Lake	295.9	5.0
	Moderate modified moraine	70.8	1.2
	Old glacial outwash	263.9	4.5
	Old marine and alluvium	8.1	0.1
	Proglacial lake	458.1	7.7
	Upland loess	3056.1	51.6
Kobuk Delta	Coarse and fine rubble	1.1	0.1
	Coastal Delta	1420.3	78.9
	Floodplain	36.9	2.1
	Highly modified moraine	84.3	4.7
	Old marine and alluvium	256.6	14.3

Supplementary Table 5.3 continued

Study Regions	Deposit Type	Area (km^2)	Percent Coverage
Selawik	Alluvial terrace	17.8	0.3
	Coarse and fine rubble	486.5	8.4
	Coastal Delta	654.4	11.3
	Floodplain	571.1	9.9
	Old marine and alluvium	2949.9	50.9
	Sand dune	192.2	3.3
	Undifferentiated mosaic	920.0	15.9
Yukon-Kuskokwim Delta	Alluvial terrace	1036.8	2.3
	Coarse and fine rubble	474.0	1.1
	Coastal Delta	6992.4	15.5
	Floodplain	701.8	1.6
	Lake	3.3	0.0
	Old marine and alluvium	16072.5	35.7
	River	1346.2	3.0
	Undifferentiated mosaic	963.5	2.1
	Upland loess	16200.7	36.0
	Volcanic	1240.8	2.8

* Jorgenson, T. M., Yoshikawa, K., Kanevskiy, M., Shur, Y. L., Romanovsky, V., Marchenko, S., Grosse, G., Brown, J., Jones, B. 2008. Permafrost characteristics of Alaska. In Proceedings of the Ninth International Conference on Permafrost, Kane DL, Hinkel KM (eds). Fairbanks, AK; 121–122.

Supplementary Table 5.4. Landsat images used for lake mapping and lake change analysis in western Alaska.

Image ID	Sensor Type	Path/Rows	Spatial Resolution	Date
LM10820181974160AAA04	LM 1 MSS	082/018	60 m	9-Jun-1974
LM10830171974233FAK03	LM 1 MSS	083/017	60 m	21-Aug-1974
LM10840131974252FAK03	LM 1 MSS	084/013	60 m	9-Sep-1974
LM10840161974252AAA05	LM 1 MSS	084/016	60 m	9-Sep-1974
LM10840181974180FAK03	LM 1 MSS	084/018	60 m	29-Jun-1974
LM10850141974217FAK03	LM 1 MSS	085/014	60 m	5-Aug-1974
LM10850161974217FAK03	LM 1 MSS	085/016	60 m	5-Aug-1974
LM20850171975221AAA04	LM 2 MSS	085/017	60 m	9-Aug-1975
LM20850181975221AAA04	LM 2 MSS	085/018	60 m	9-Aug-1975
LM20870131975205AAA05	LM 2 MSS	087/013	60 m	24-Jul-1975
LM10880131972213AAA02	LM 1 MSS	088/013	60 m	31-Jul-1972
LM10880141974184AAA05	LM 1 MSS	088/014	60 m	3-Jul-1974
LC80760182014157LGN00	LC 8 OLI	076/018	30 m	6-Jun-2014
LC80770182013193LGN00	LC 8 OLI	077/018	30 m	12-Jul-2013
LC80780132013168LGN00	LC 8 OLI	078/013	30 m	17-Jun-2013
LC80780142014235LGN00	LC 8 OLI	078/014	30 m	23-Aug-2014
LC80780172014171LGN00	LC 8 OLI	078/017	30 m	20-Jun-2014
LC80790132014210LGN00	LC 8 OLI	079/013	30 m	29-Jul-2014
LC80790142014210LGN00	LC 8 OLI	079/014	30 m	29-Jul-2014
LC80790162014210LGN00	LC 8 OLI	079/016	30 m	29-Jul-2014
LC80790172014210LGN00	LC 8 OLI	079/017	30 m	29-Jul-2014
LC80800132014217LGN00	LC 8 OLI	080/013	30 m	5-Aug-2014
LC80800142014217LGN00	LC 8 OLI	080/014	30 m	5-Aug-2014
LC80800152014217LGN00	LC 8 OLI	080/015	30 m	5-Aug-2014
LC80820142015170LGN00	LC 8 OLI	082/014	30 m	19-Jun-2015
LC80830132014222LGN00	LC 8 OLI	083/013	30 m	10-Aug-2014

5.12. References

Alessa, L., Kliskey, A., Lammers, R., Arp, C., White, D., Hinzman, L., Busey, R., 2008. The Arctic Water Resource Vulnerability Index: An Integrated Assessment Tool for Community Resilience and Vulnerability with Respect to Freshwater. Environ. Manage. 42, 523–541. doi:10.1007/s00267-008-9152-0

Arp and Jones, 2009. Geography of Alaska lake districts: identification, description, and analysis of lake- rich regions of a diverse and dynamic state: U.S. Geological Survey Scientific Investigations Report, 2008–5215, 40 p.

Arp C.D., Jones B.M., Urban F.E., Schmutz J.A., Jorgenson M.T., 2010. Two mechanisms of aquatic and terrestrial habitat change along an Alaskan Arctic coastline. Polar Biology 33: 1629–1640. doi:10.1007/s00300-010- 0800-5.

Arp, C.D., Jones, B.M., Urban, F.E., Grosse, G., 2011. Hydrogeomorphic processes of thermokarst lakes with grounded-ice and floating-ice regimes on the Arctic coastal plain, Alaska. Hydrol. Process. 25, 2422–2438. doi:10.1002/hyp.8019

Bastviken, D., Cole, J., Pace, M., Tranvik, L., 2004. Methane emissions from lakes: Dependence of lake characteristics, two regional assessments, and a global estimate. Global Biogeochem. Cycles 18, 1–12. doi:10.1029/2004GB002238

Blaschke, T. and Strobl, J., 2001. What's wrong with pixels? Some recent developments interfacing remote sensing and GIS. GIS – Zeitschrift für Geoinformationssysteme, 14 (6), 12–17.

Blaschke, T., Lang, S., Hay, G.J. (Eds.), 2008. Object Based Image Analysis, Springer, Heidelberg, Berlin, New York, 817 p.

Bockheim, J.G., Hinkel, K.M., 2012. Accumulation of Excess Ground Ice in an Age Sequence of Drained Thermokarst Lake Basins, Arctic Alaska. Permafr. Periglac. Process. 23, 231–236. doi:10.1002/ppp.1745

Bosikov, N.P., 1998. Wetness variability and dynamics of thermokarst processes in central Yakutia. Proceedings of the 7th International Conference on Permafrost, Yellowknife, Canada, pp. 71–74.

Brosius, L.S., Walter Anthony, K.M., Grosse, G., Chanton, J.P., Farquharson, L.M., Overduin, P.P., Meyer, H., 2012. Using the deuterium isotope composition of permafrost meltwater to constrain thermokarst lake contributions to atmospheric CH 4 during the last deglaciation. J. Geophys. Res. 117, G01022. doi:10.1029/2011JG001810

Burn, C.R., Smith, M.W., 1990. Development of thermokarst lakes during the Holocene at sites near Mayo, Yukon territory. Permafrost & Periglacial Processes. 1, 161–175.

Burn, C., 2002. Tundra lakes and permafrost, Richards Island, western Arctic coast, Canada, Can. J. Earth Sci., 39, 1281–1298, doi:10.1139/ E02-035.

Chen, M., Rowland, J.C., Wilson, C.J., Altmann, G.L., Brumby, S. P., 2013. The Importance of Natural Variability in Lake Areas on the Detection of Permafrost Degradation: A Case Study in the Yukon Flats, Alaska. Permafrost and Periglacial Processes. 24, 224–240. doi: 10.1002/ppp.1783

Chen, M., Rowland, J.C., Wilson, C.J., Altmann, G.L., Brumby, S.P., 2014. Temporal and spatial pattern of thermokarst lake area changes at Yukon Flats, Alaska. Hydrological Processes. 28, 837–852. doi: 10.1002/hyp.9642

Clark, R., Ott, A., Rabe, M., Vincent-Lang, D., Woodby, D., 2010. The effects of a changing climate on key habitats in Alaska. Special Publication No. 10-14, Alaska Department of Fish and Game, 102 p.

Eisner W.R., Cuomo C.J., Hinkel K.M., Jones B.J., Brower, R.H. Sr., 2009. Advancing landscape change research through the incorporation of Iñupiaq Knowledge. Arctic, 62 (4), 429–442. doi: http://dx.doi.org/10.14430/arctic174

Frohn, R.C., Hinkel, K.M., Eisner, W.R., 2005. Satellite remote sensing classification of thaw lakes and drained thaw lake basins on the North Slope of Alaska. Remote Sensing of Environment. 97, 116–126. doi: 10.1016/j.rse.2005.04.022

Grosse G., Jones B., Arp C., 2013. Thermokarst Lakes, Drainage, and Drained Basins. In: Shroder JF (ed.): Treatise on Geomorphology. Vol. 8, pp. 325-353. San Diego: Academic Press. doi:10.1016/B978-0-12-374739-6.00216-5

Hinkel, K.M., Eisner, W.R., Bockheim, J.G., Nelson, F.E., Peterson, K.M., Dai, X., 2003. Spatial Extent, Age and Carbon Stocks in Drained Thaw Lake Basins on the Barrow Alaska Peninsula, Alaska. Arctic, Antart. Alp. Res. 35, 291–330.

Hinkel, K.M., Jones, B.M., Eisner, W.R., Cuomo, C.J., Beck, R. A., Frohn, R., 2007. Methods to assess natural and anthropogenic thaw lake drainage on the western Arctic coastal plain of northern Alaska. J. Geophys. Res. 112, 1–9. doi:10.1029/2006JF000584

Hinkel, K.M., Lenters, J.D., Sheng, Y., Lyons, E. A., Beck, R. A., Eisner, W.R., Maurer, E. F., Wang, J., Potter, B. L., 2012. Thermokarst Lakes on the Arctic Coastal Plain of Alaska: Spatial and Temporal Variability in Summer Water Temperature. Permafr. Periglac. Process. 23, 207–217. doi:10.1002/ppp.1743

Hinzman, L.D., Bettez, N.D., Bolton, W.R., Chapin, F.S., Dyurgerov, M.B., Fastie, C.L., Griffith, B., Hollister, R.D., Hope, A., Huntington, H.P., Jensen, A.M., Jia, G.J., Jorgenson, T., Kane, D.L., Klein, D.R., Kofinas, G., Lynch, A.H., Lloyd, A.H., McGuire, A. D., Nelson, F.E., Oechel, W.C., Osterkamp, T.E., Racine, C.H., Romanovsky, V.E., Stone,

R.S., Stow, D. a., Sturm, M., Tweedie, C.E., Vourlitis, G.L., Walker, M.D., Walker, D. A., Webber, P.J., Welker, J.M., Winker, K.S., Yoshikawa, K., 2005. Evidence and Implications of Recent Climate Change in Northern Alaska and Other Arctic Regions. Clim. Change 72, 251–298. doi:10.1007/s10584-005-5352-2

Hopkins, D.M., 1949. Thaw lakes and thaw sinks in the Imuruk Lake area, Seward Peninsula, Alaska. The Journal of Geology. 57, 119–131. http://www.jstor.org/stable/30063635.

Intergovernmental Panel on Climate Change (IPCC), 2007. Fourth Assessment Report: The physical science basis. Cambridge Univ. Press. (https://www.ipcc.ch)

Jafarov, E.E., Marchenko, S.S., Romanovsky, V.E., 2012. Numerical modeling of permafrost dynamics in Alaska using a high spatial resolution dataset. Cryosphere 6, 613–624. doi:10.5194/tc-6-613-2012

Jones, B.M., Hinkel, K.M., Arp, C.D., Eisner, W.R., 2008. Modern Erosion Rates and Loss of Coastal Features and Sites, Beaufort Sea Coastline , Alaska 61, 361–372.

Jones, B., Arp, C., Hinkel, K., Beck, R., Schmutz, J., Winston, B., 2009. Arctic lake physical processes and regimes with implications for winter water availability and management in the National Petroleum Reserve Alaska. Environmental Management 43: 1071–1084. DOI: 10.1007/s00267-008-9241-0.

Jones, B.M., Grosse, G., Arp, C.D., Jones, M.C., Walter Anthony, K.M., Romanovsky, V.E., 2011. Modern thermokarst lake dynamics in the continuous permafrost zone, northern Seward Peninsula, Alaska. J. Geophys. Res. 116, 1–13. doi:10.1029/2011JG001666

Jones, M.C., Grosse, G., Jones, B.M., Walter Anthony, K., 2012. Peat accumulation in drained thermokarst lake basins in continuous, ice-rich permafrost, northern Seward Peninsula, Alaska. J. Geophys. Res. 117, 1–16. doi:10.1029/2011JG001766

Jones, B.M., Arp, C.D., 2015. Observing a Catastrophic Thermokarst Lake Drainage in Northern Alaska. Permafr. Periglac. Process. 119–128. doi:10.1002/ppp.1842

Jorgenson, M.T., and Osterkamp,T., 2005. Response of boreal ecosystems to varying modes of permafrost degradation, Can. J. For. Res. 35, 2100–2111. doi:10.1139/x05-153.

Jorgenson, M.T., Shur, Y., 2007. Evolution of lakes and basins in northern Alaska and discussion of the thaw lake cycle. J. Geophys. Res. 112, 1–12. doi:10.1029/2006JF000531

Jorgenson, T.M., Yoshikawa, K., Kanevskiy, M., Shur, Y.L., Romanovsky, V., Marchenko, S., Grosse, G., Brown, J., Jones, B. 2008. Permafrost characteristics of Alaska. In Proceedings of the Ninth International Conference on Permafrost, Kane DL, Hinkel KM (eds). Fairbanks, AK; 121–122.

Jorgenson, M.T., Romanovsky, V., Harden, J., Shur, Y., O'Donnell, J., Schuur, E.A.G., Kanevskiy, M., Marchenko, S., 2010. Resilience and vulnerability of permafrost to climate change. Can. J. For. Res. 40, 1219–1236. doi:10.1139/X10-060

Karlsson, J., Lyon, S., Destouni, G., 2014. Temporal Behavior of Lake Size-Distribution in a Thawing Permafrost Landscape in Northwestern Siberia. Remote Sens. 6, 621–636. doi:10.3390/rs6010621

Kessler, M. A., Plug, L.J., Walter Anthony, K.M., 2012. Simulating the decadal- to millennial-scale dynamics of morphology and sequestered carbon mobilization of two thermokarst lakes in NW Alaska. J. Geophys. Res. Biogeosciences 117, 1–22. doi:10.1029/2011JG001796

Klein, E.S., Yu, Z., Booth, R.K., 2013. Recent increase in peatland carbon accumulation in a thermokarst lake basin in southwestern Alaska. Paleo3 392, 186-195.

Labrecque, S., Lacelle, D., Duguay, C.C.R., Lauriol, B., Hawkings, J., 2009. Contemporary (1951-2001) evolution of lakes in the Old Crow Basin, Northern Yukon, Canada: remote sensing, numerical modeling, and stable isotope analysis. Arctic 62, 225–238.

Li, W., Du, Z., Ling, F., Zhou, D., Wang, H., Gui, Y., Sun, B., Zhang, X., 2013. A Comparison of Land Surface Water Mapping Using the Normalized Difference Water Index from TM, ETM+ and ALI. Remote Sens. 5, 5530–5549. doi:10.3390/rs5115530

Ling, F., Zhang, T.J., 2004. Modeling study of talik freeze-up and permafrost response under drained thaw lakes on the Alaskan Arctic Coastal Plain. Journal of Geophysical Research 109, D01111.

Livingstone, D.A., Bryan, K., Leahy, R.G., 1958. Effects of an arctic environment on the origin and development of fresh-water lakes. Limnol. Oceanogr. 3, 192–214.

Mackay, J.R., 1988. Catastrophic lake drainage, Tuktoyaktuk Peninsula area, District of Mackenzie. Curr. Res.-Bull. Geol. Surv. Can., 88–1D, 83–90.

Mackay, J.R., Burn, C.R., 2002. The first 20 years (1978–1979 to 1998–1999) of ice-wedge growth at the Illisarvik experimental drained lake site, western Arctic coast, Canada. Can. J. Earth Sci. 39, 95–111.

Marcot, B., Jorgenson, M.T., Lawler, J., Handel, C., DeGange, A., 2015. Projected changes in wildlife habitats in Arctic natural areas of northwest Alaska. Climatic Change 130, 145-154.

Mars, J.C., and Houseknecht, D.W., 2007. Quantitative remote sensing study indicates doubling of coastal erosion rate in the past 50 yr along a segment of the Arctic coast of Alaska. Geology 35(7), 583–586.

Marsh, P., Russell, M., Pohl, S., Haywood, H., Onclin, C., 2009. Changes in thaw lake drainage in the western Canadian Arctic from 1950 to 2000. Hydrological Process. 23, 145–158. DOI:10.1002/hyp.7179.

Mather, P. M. and Koch, M., 2011. Computer processing of remotely-sensed images: An introduction, 4th edn, John Wiley & Sons.

McFeeters, S.K., 1996. The use of the normalized difference water index (NDWI) in the delineation of open water features. Int. J. Remote Sens. 17, 1425–1432. doi: 10.1080/01431169608948714

Navulur, K., 2007. Multispectral Image Analysis Using the Object-Oriented Paradigm. CRC Press, Inc., Boca Raton, FL, USA.

Osterkamp, T. E. and Romanovsky,V. E.: 1999. Evidence for warming and thawing of discontinuous permafrost in Alaska. Permafrost Periglacial Process. 10, 17–37.

Plug, L.J., Walls, C., Scott, B.M., 2008. Tundra lake changes from 1978 to 2001 on the Tuktoyaktuk Peninsula, western Canadian Arctic. Geophys. Res. Lett. 35, L03502. doi:10.1029/2007GL032303

Regmi, P., Grosse, G., Jones, M., Jones, B., Anthony, K., 2012. Characterizing Post-Drainage Succession in Thermokarst Lake Basins on the Seward Peninsula, Alaska with TerraSAR-X Backscatter and Landsat-based NDVI Data. Remote Sensing 4, 3741-3765.

Riordan, B., Verbyla, D., McGuire, a. D., 2006. Shrinking ponds in subarctic Alaska based on 1950–2002 remotely sensed images. J. Geophys. Res. 111, G04002. doi:10.1029/2005JG000150

Roach, J., Griffith, B., Verbyla, D., Jones, J., 2011. Mechanisms influencing changes in lake area in Alaskan boreal forest. Global Change Biology 17, 2567-2583.

Roach, J.K., Griffith, B., Verbyla, D., 2013. Landscape influences on climate-related lake shrinkage at high latitudes. Glob. Chang. Biol. 19, 2276–2284. doi:10.1111/gcb.12196

Romanovsky, V.E., Smith, S.L., Christiansen, H.H., 2010. Permafrost thermal state in the polar Northern Hemisphere during the international polar year 2007-2009: A synthesis. Permafr. Periglac. Process. 21, 106–116. doi:10.1002/ppp.689

Rowland, J.C., Travis, B.J., Wilson, C.J., 2011. The role of advective heat transport in talik development beneath lakes and ponds in discontinuous permafrost. Geophys. Res. Lett. 38, L17504.

Rover, J., Ji, L., Wylie, B.K., Tieszen, L.L., 2012. Establishing water body areal extent trends in interior Alaska from multi-temporal Landsat data. Remote Sens. Lett. 3, 595–604. doi:10.1080/01431161.2011.643507

Schneider Von Deimling, T., Grosse, G., Strauss, J., Schirrmeister, L., Morgenstern, A., Schaphoff, S., Meinshausen, M., Boike, J., 2015. Observation-based modelling of permafrost carbon fluxes with accounting for deep carbon deposits and thermokarst activity. Biogeosciences 12, 3469–3488. doi:10.5194/bg-12-3469-2015

Smith, L.C., Sheng, Y., MacDonald, G.M., Hinzman, L.D., 2005. Disappearing Arctic lakes. Science 308, 1429. doi:10.1126/science.1108142

Smith, L.C., Sheng, Y., Macdonald, G.M., 2007. Short Communication A First Pan-Arctic Assessment of the Influence of Glaciation , Permafrost , Topography and Peatlands on Northern Hemisphere Lake Distribution 208, 201–208. doi:10.1002/ppp

Smith, S.L., Romanovsky, V.E., Lewkowicz, A.G., Burn, C.R., Allard, M., Clow, G.D., Yoshikawa, K., Throop, J., 2010. Thermal state of permafrost in North America: a contribution to the international polar year. Permafr. Periglac. Process. 21, 117–135. doi:10.1002/ppp.690

Terenzi, J., Jorgenson, M.T., Ely, C.R., 2014. Storm-Surge Flooding on the Yukon-Kuskokwim Delta, Alaska. Arctic 67, 15.

Tranvik, L.J., Downing, J.A., Cotner, J.B., Loiselle, S.A., Striegl, R.G., Ballatore, T.J., Dillon, P., Finlay, K., Fortino, K., Knoll, L.B., Kortelainen, P.L., Kutser, T., Larsen, S., Laurion, I., Leech, D.M., Mccallister, S.L., Mcknight, D.M., Melack, J.M., Overholt, E., Porter, J.A., Prairie, Y., Renwick, W.H., Roland, F., Sherman, B.S., Schindler, D.W., Sobek, S., Tremblay, A., Vanni, M.J., Verschoor, A.M., Wachenfeldt, E. Von, Weyhenmeyer, G.A., 2009. Lakes and reservoirs as regulators of carbon cycling and climate. Limnol. Ocean. 54, 2298–2314.

Turner, K.W., Wolfe, B.B., Edwards, T.W.D., 2010. Characterizing the role of hydrological processes on lake water balances in the Old Crow Flats, Yukon Territory, Canada, using water isotope tracers. J. Hydrol. 386, 103–117. doi:10.1016/j.jhydrol.2010.03.012

Walter, K.M., Zimov, S. a, Chanton, J.P., Verbyla, D., Chapin, F.S., 2006. Methane bubbling from Siberian thaw lakes as a positive feedback to climate warming. Nature 443, 71–5. doi:10.1038/nature05040

Walter, K.M., Smith, L.C., Chapin, F.S., 2007a. Methane bubbling from northern lakes: present and future contributions to the global methane budget. Philos. Trans. A. Math. Phys. Eng. Sci. 365, 1657–76. doi:10.1098/rsta.2007.2036

Walter, K.M., Edwards, M.E., Grosse, G., Zimov, S.A., Chapin, III., F.S., 2007b. Thermokarst lakes as a source of atmospheric CH_4 during the last deglaciation. Science

Walter Anthony, K.M., Zimov, S. A., Grosse, G., Jones, M.C., Anthony, P.M., Chapin, F.S, Finlay, J.C., Mack, M.C., Davydov, S., Frenzel, P., Frolking, S., 2014. A shift of thermokarst lakes from carbon sources to sinks during the Holocene epoch. Nature 511, 452–456. doi:10.1038/nature13560

West, J.J., Plug, L.J., 2008. Time-dependent morphology of thaw lakes and taliks in deep and shallow ground ice. J. Geophys. Res. 113, 1–14. doi:10.1029/2006JF000696

Xu, H., 2006. Modification of normalized difference water index (NDWI) to enhance open water features in remotely sensed imagery. Int. J. Remote Sens. 27, 3025–3033. Doi: 10.1080/01431160600589179

Yoshikawa, K., Hinzman, L.D., 2003. Shrinking thermokarst ponds and groundwater dynamics in discontinuous permafrost near council, Alaska. Permafr. Periglac. Process. 14, 151–160. doi:10.1002/ppp.451

Zhang, T., Barry, R.G., Knowles, K., Heginbottom, J.A., Brown, J., 2008. Statistics and characteristics of permafrost and ground-ice distribution in the Northern Hemisphere. Polar Geogr. 31, 47–68. doi:10.1080/10889370802175895

Zona, D., Oechel, W.C., Peterson, K.M., Clements, R.J., Paw U, K.T., Ustin, S.L., 2010. Characterization of the carbon fluxes of a vegetated drained lake basin chronosequence on the Alaskan Arctic Coastal Plain. Glob. Chang. Biol. 16, 1870–1882. doi:10.1111/j.1365-2486.2009.02107.x

Chapter 6. Summary

6.1. Overview

In this dissertation, I examined four applications of high- and medium-resolution remote sensing images derived from both radar and optical sensors in combination with field-based observations to study lake dynamics at local and regional scales. The dissertation focused on the application of (1) high-resolution airborne optical imagery to detect methane ebullition bubbles trapped in early winter lake ice and to examine its spatiotemporal dynamics, (2) TerraSAR-X data to characterize post drainage succession patterns in drained lake basins and to correlate these characteristics with basin age and peat accumulation, and (3) Landsat images to assess lake distribution and lake area changes in relation to regional permafrost extent. Each study highlights the excellent opportunities that remote sensing methods offer to evaluate different aspects of permafrost region lake dynamics, to identify spatiotemporal changes of lakes and environmental responses associated with lake changes, and in combination with field-survey data to improve the ability to quantify methane emission from whole lakes with the potential for upscaling to regional scales.

6.2. Key findings

6.2.1. Chapter 2

In this chapter, I developed a classification technique built on using an Object-Based Image Analysis (OBIA) framework to successfully map ebullition bubble patches trapped in early winter lake ice of an interior Alaska thermokarst lake. I used high-resolution (9-11 cm) aerial images acquired two and four days following freeze up in the years 2011 and 2012, respectively. This study focusing on Goldstream Lake, Fairbanks, Alaska showed that high-resolution optical remote sensing is a promising tool to map the distribution of point-source methane ebullition seeps across an entire thermokarst lake surface, a task that is difficult to achieve through field-based surveys alone. OBIA proved to be efficient in identifying bubble clusters on lake ice with a high accuracy of > 95% for the years 2011 and 2012. This classification framework can be applied on other ice-covered lakes to derive useful information that can complement field-based surveys to understand spatiotemporal dynamics of methane ebullition and identify variables that control the methane ebullition dynamics.

6.2.2. Chapter 3

In this chapter, I analyzed the spatiotemporal dynamics of methane ebullition bubble patches trapped in lake ice using the bubble mapping results from Chapter 2 in conjunction with field-based observations of ebullition bubbles. This remote sensing approach helped to reveal the location and relative sizes of high- and low-flux seepage zones within the study lake, Goldstream Lake, located in Fairbanks, Alaska. It provided an ability to estimate whole-lake methane emission by combining the field-measured seep flux data with the seep classification results derived from the remote sensing data. The study showed that the spatial pattern of ebullition bubble patches can help to characterize permafrost carbon mobilization in the lake since lake portions with greater numbers of high-flux seeps likely indicate rapidly thawing organic-rich permafrost deposits or the eroding lake margins. The study helped to evaluate the location stability of ebullition seeps across time indicating that a large proportion of ebullition seeps in the study lake were location-stable over at least two winter seasons in the 2011–2012 observation periods. The analysis of temporal distribution of ebullition bubble patches in relation to atmospheric pressure measured for the area demonstrated the ebullition is highly controlled by changes in air pressures. This shows an opportunity of combining remote sensing data with other environmental observations to identify the drivers of bubble dynamics, which can further aid in a more accurate estimation of ebullition from lakes. This approach is also applicable to other regions and will help to differentiate lakes in a region based on methane emission by estimating ebullition seep density, and their relative methane flux. This differentiation could potentially be used to identify the presence or absence of organic-rich permafrost deposits such as yedoma in the area. However, the timing of optical image acquisitions is a critical and a potentially limiting factor, with respect to both atmospheric pressure changes and snow/no-snow conditions during early lake freeze-up. Therefore, high-resolution remotely sensed optical images in combination with SAR and field data will be a very valuable tool to improve the estimation of methane emission from lakes at the regional scale.

6.2.3. Chapter 4

In this chapter, I used high-resolution TerraSAR-X (TSX) images to derive a relationship of SAR backscatter of surfaces in drained thermokarst lake basins (DTLBs) with basin age, an indicator of the amount of peat stored in the basin soils. To answer the question how this

relationship would compare to the relationship estimated by using Normalized Difference Vegetation Index (NDVI) derived from optical remote sensing data, I examined the backscatter and NDVI properties of 60 known DTLBs that drained partially or completely since 1950 (modern DTLBs), as well as the properties of 14 DTLBs radiocarbon-dated to be up to 10,000 years BP (young, medium-aged, old and ancient DTLBs) in three subsets: (1) 0–50 years since drainage, modern basins; (2) 50–10,000 years since drainage, radiocarbon-dated basins; and (3) 0–10,000 years since drainage, modern and radiocarbon-dated basins. The findings indicated that both TSX backscatter and Landsat NDVI can trace long-term (0–10,000 years) succession dynamics of DTLBs related to vegetation, soil and permafrost changes. TSX backscatter data outperformed NDVI in discriminating basin successional stage for the 50–10,000 year period, likely due to its ability to partially detect soil moisture conditions. However, in modern basins, the 50-year time scale was insufficient to find a clear relationship of basin age with TSX backscatter and NDVI. Overall, there was a decreasing trend in both backscatter and NDVI as basin age increased as a result of post-drainage changes in basin surface properties that include decreasing vegetation productivity after an initial productivity spike, decreasing soil moisture, renewed ice-wedge growth and development of either ponded or dry polygonal networks. This study highlights the excellent opportunity to use and combine various remote sensing tools for identifying successional stages on DTLBs. This observation can further help to estimate the areal extent of high latitude carbon pools and sources of greenhouse gases associated with thermokarst lake dynamics.

6.2.4. Chapter 5

In this chapter, I used Landsat images from 1972 to 2014 to assess the spatial distribution of lakes and the changes in areal extent of lakes > 1 ha in major lake-rich regions in western Alaska distributed across various permafrost extent (continuous, discontinuous, sporadic and isolated). The study regions included Baldwin Peninsula, Beringia, Central Seward Peninsula, Kobuk Delta, Selawik, and Yukon-Kuskokwim Delta. I examined the relationship of direction of lake change with the regional permafrost extent types. The results showed widespread lake loss in all six studied regions. Many large lakes drained and shrunk in area while the abundance of lakes < 10 ha increased significantly due to partial drainage of large lakes creating numerous remnant ponds. Though lake drainage dominated most portions of the region, lake area increase was

noticed in some regions of the continuous permafrost zone. Lake area shrinkage dominated the non-continuous permafrost zones except in the sporadic zone located in the delta regions. As a consequence of the observed lake change trajectories, we expect increased numbers of drainage events in the continuous permafrost as climate gets warmer and surface permafrost begins to degrade or even becomes discontinuous in extent. To make more detailed projections, other important climatic and non-climatic factors such as precipitation, temperature, connectivity, lake ice regime, and surface topography need to be taken into account in further studies that can significantly influence the complex behavior of lakes in changing permafrost environments. Additionally, efforts to assess lake area change and their causes in high northern latitudes should be continued for future planning and decision making.

6.3. Future research directions

In my dissertation I show that there is an immense opportunity to use and combine various remote sensing tools to study permafrost-region lake dynamics and to evaluate associated environmental changes. A suite of previous studies has also highlighted the ability of remote sensing tools to advance research on lakes that are widely spread in remote locations of the permafrost regions in the high northern latitudes. Moreover, high spatial and temporal resolution satellite image datasets covering large portions of the Arctic and Subarctic are getting readily available now. For the next steps, knowing that the lake ecosystem balance maintained by permafrost-climate interactions is already shifting, lakes should be monitored regularly using both remote sensing and field observations to understand how they are responding to the changing environment for predicting future scenarios and the associated impacts. Another option of data collection can be via portable, inexpensive and customizable airborne platforms such as Unmanned Aerial Vehicles (UAV). This offers an excellent opportunity to collect very high-resolution image data as needed particularly when the timing of image acquisition is a crucial factor, for example while studying methane bubbles trapped in lake ice using optical imagery, the window to collect images of snow-free ice-covered lakes is very narrow. Even though data collection using UAV might be limited to a small spatial extent, this is an option that can easily overcome logistical difficulties associated with fieldwork at a very low cost and it still will be a valuable tool that can tremendously help to understand lake dynamics. Additionally, this will provide an opportunity to design pilot research that can be scaled up to larger regions.

Another step should be directed towards developing methods to upscale the study across larger Arctic and Subarctic regions to detect and quantify regional lake dynamic patterns and responses of lakes to ongoing climate change. This means development of an automated or semi-automated image analysis method for feature extraction. It is important to note that scaling such image-processing tasks to larger regions requires vast computational capacities and image processing software that allows automation to process gigabytes of data. Even though there are advanced proprietary, off the shelf image processing software products available, they are mostly expensive and may not necessarily fulfill the full range of needs in a single software package. Recently, the use of open-source software products and libraries for image processing and analysis such as QGIS, Python geospatial libraries has become popular among geospatial scientists because it is an inexpensive option, which also provides greater customizable options, flexibility and freedom to perform a task. Some of these open-source platforms have remarkable capacity to process large volumes of data, which can minimize the processing time tremendously, which in many cases can perform better than conventional proprietary software products. So, there are other viable cost-effective tools that can help to tailor a customized processing environment based on image processing needs and can be used in combination with specialized propriety software that can help fulfill other needs that open-source software products can't provide. These options should be explored for computational heavy work in future.

At the same time, field observations should be continued to collect data for validation and to derive important results and relationships for upscaling purposes. This further sheds light on collaborative research opportunities for combining field-based observations and remote sensing tools to improve the understanding of how lakes in permafrost regions may respond to the projected climate change and what it means to the surrounding ecosystem and global carbon budget. Therefore, future work should be directed towards such collaborative research to fulfill the ultimate goal of upscaling the response of lakes to changing climate and permafrost environments to larger regions. This will enable scientists to project future regional hydrological characteristics, feedbacks to climate change associated with the regional and global carbon cycle, and to assess stability of natural resources vital to human communities and for supporting a healthy wildlife ecosystem. Last but not the least, future research should be dedicated to the

making of novel remote sensing data products that can be useful to a variety of stakeholder groups including permafrost scientists, land, wildlife and resource managers, and communities in the permafrost region for future planning and decision making.